Environmental Noise from Underwater Explosions and the Impact of the Seabed on the Received Levels

Alexander G. Soloway

A dissertation

submitted in partial fulfillment of the

requirements for the degree of

Doctor of Philosophy

University of Washington

2018

Reading Committee:

Peter Dahl, Chair

Kevin Williams

Robert Odom

Brian Polagye

Program Authorized to Offer Degree:

Mechanical Engineering

University of Washington

Abstract

Environmental Noise from Underwater Explosions and the Impact of the Seabed on the Received Levels

Alexander G. Soloway

Chair of the Supervisory Committee:
Professor Peter H. Dahl
Mechanical Engineering

In the following work measurements of underwater explosions from three experimental sites area presented and compared. The goals of this work are to present the measurements of small underwater explosions (charges weighing between 0.5 kg and 20 kg) with an emphasis on the metrics commonly used to describe environmental noise including the peak pressure and the SEL. These data are provided within the context of the measurement environments, the seabed in particular, so that they can be more effectively utilized by both researchers and policy makers for studying environmental noise and in the development of mitigation measures to protect marine life from harmful noise levels.

TABLE OF CONTENTS

LIST OF FIGURES

LIST OF TABLES

ACKNOWLEDGEMENTS

First, I would like to thank my committee starting with Kevin Williams for all of his help, advice, feedback, that helped me to greatly improve the quality of my research. Next, I want to thank Bob Odom for answering the hundreds of questions I have had on elastic waves and geophysics which has been in invaluable resource. I have also had a number of his books for longer than I'd care to admit. These have been invaluable resources that I continue to reference. I would like to thank Brian Polagye for all of the help and support which has kept me grounded. Miles Logsdon has guided me throughout the logistical side of getting a PhD and has kept me honest in my timelines. This process would have been considerably harder without his guidance and experience. Finally, I would like to thank my adviser Peter Dahl for this wonderful opportunity as well as the funding that has allowed me to complete this degree.

I would also like to thank my friends who have supported me, distracted me, and listened to all of my complaints. You have kept me grounded when my world turned upside down and helped me remember to stay positive. In particular, I would like to thank Rachael Minucciani who gave me the kick I needed to finish writing this dissertation. I hate to admit it, but I needed it. I would also like to thank all of my friends in the Washington Alpine Club who showed me that there is a world outside of school that is a lot of fun. For better or worse, they might have done this too well.

Saving the best for last, I would like to thank my family. To my sister Sam and my brother in law Ben, for putting up with me, listening to me, and for always having a room (or their van) available for me to live in. Most of all I'd like to thank my parents for always being there for whenever I needed them and putting up with me when I'm at my worst. I know I don't tell them this enough, but they mean the world to me. Finally, I'd like to thank my niece and nephew. They haven't really done all that much, but they are adorable.

DEDICATION

To my parents. For their unconditional love and for liking me most of the time.

Chapter 1. INTRODUCTION

There are a variety of studies looking at the impact of sound on marine animals [1]–[11], and it is now well-established that high sound levels can harm marine animals by causing both temporary [12] and permanent [13] hearing threshold shifts, total hearing loss, and even death. Explosives, commonly used by the Navy as well as in the marine construction industry, can produce some of the loudest anthropogenic noises and pose a serious threat to marine mammals. While explosives have been widely used as broadband acoustic sources for decades [14]–[17], little of the work has focused on the metrics commonly used for reporting environmental noise; these include the peak pressure and sound exposure levels (SEL). Few measurements of underwater explosions between 1 kg and 20 kg have been collected at short ranges (less than 2 km) where the sound levels are highest [10], [18], [19], and many of the previous studies have been conducted in deep water where little, if any, interaction with the seabed occurred [20]–[25], [16], [17].

Empirical equations are available for both the peak pressure and the energy flux density (which is proportional to SEL) for explosions [26], but their utility is limited in shallow water noise prediction as they were developed for sources in unbounded media. Current predictive models typically over- or under-estimate the noise levels produced by underwater explosions, however improving these predictions has been difficult due to the lack of measured data. There is therefore a need for high quality explosion measurements in shallow water as well as studies to determine how the seabed affects the resulting environmental noise metrics.

In the following work, measurements of underwater explosions from three experimental sites are presented and compared. These experiments were conducted at the U.S. Navy Pu`uloa Underwater Detonation Range, Pearl Harbor, HI, (Pu`uloa) at a training range 7 km off the coast of Virginia Beach, VA [19], [27] (Virginia Beach) and at the Silver Strand Training Complex, Naval Base Coronado, Coronado, CA (Silver Strand) [28]. These measurements show that the peak pressures and SEL at the Pu`uloa measurement site is up to 25 dB lower than levels measured at the other two sites. These results are considered within the context of the seabed at the measurement sites. Despite a lack of complete information on the seabed, these data are used

along with previous seabed studies at the measurement sites to develop geoacoustic models. Doing so involves;

1. Presenting the measurements of small underwater explosions (charges weighing between 0.5 kg and 20 kg) with an emphasis on the metrics commonly used to describe environmental noise including the peak pressure and the SEL.
2. Determining why measurements collected at the Pu`uloa measurement site are considerably lower than at the other two sites.
3. Providing context about the measurement environments so that these data can be more effectively utilized by both researchers and policy makers for studying environmental noise and in the development of mitigation measures to protect marine life from harmful noise levels.

In Chapter 2, background information on shallow water noise propagation, underwater explosions and the environmental metrics commonly used to describe underwater noise levels are provided. The chapter begins by discussing the motivation for this work; this includes both the impact of anthropogenic noise on marine animals as well as the process by which this impact is assessed. Next, background on the environmental models and physical loss mechanisms that are explored in this work are presented including the canonical Pekeris waveguide with shear wave effects included, depth dependent seabed properties in sandy sediments (both shear and compressional wave profiles) and losses due to thin layers overlying elastic bottoms. Environmental metrics commonly used to quantify environmental noise are also discussed along with details on their implementations. As underwater explosions are the sources of noise considered in this work, relevant background on the explosion process are also presented.
In Chapter 3, experiment descriptions are presented for the three studies considered in this work.

With the background information laid out, the next step is to go through the tools and data analysis techniques used in subsequent sections to develop an understanding of the measurement environment. This is done in Chapter 4 through the study of low-frequency Scholte interface waves generated by the explosions at the Virginia Beach Measurement site. In this chapter the observations of very low frequency noise (between 3 Hz and 10 Hz) are considered and the

OASES wavenumber integration propagation model [29] are utilized for predictive modelling. This chapter shows how numerical propagation models and observable features in the data can be utilized in developing an understanding of the measurement environment.

Having demonstrated how OASES can be utilized for studying the seabed composition, in Chapter 5 attention is turned to comparing and understanding the environmental noise levels measured at the three sites. Comparing the noise levels at the three sites shows the levels at one of the measurement sites is up to 25 dB lower than the other two. Using the techniques presented in Chapter 4 in conjunction with an analytical model, it is shown that these differences are due to the seabed composition. Additional mechanisms that could be responsible for these differences are also considered but ultimately have been ruled out. This includes differences in the source model, sea surface roughness effects as well as bathymetric refraction. Based on previous studies, the seabeds at the Virginia Beach and Silver Strand measurement sites are composed of sandy sediments and are modelled as Pekeris waveguides whereas the Pu`uloa site is composed of a thin calcareous-sand layer overlying an elastic limestone half-space.

While the Pekeris model generally gives good agreement to the measured data at the Virginia Beach measurement site, poor agreement between 40 Hz and 100 Hz are observed. In Chapter 6 this discrepancy is considered. The study of Scholte interface waves in Chapter 4 shows that the seabed at this site has depth-dependent characteristics. This chapter shows that the observed discrepancies between 40 Hz and 100 Hz could be a result of seabed refraction caused by a depth dependent compressional wave speed. Outside of this frequency range the depth-dependent and Pekeris seabed models are shown to be in reasonable agreement.

Having presented the measured sound levels for the three measurement sites and comparing the resulting noise levels within the context of the seabed composition, the final step in Chapter 7 discusses the implications of these results on the noise field, how these data can be used by others conducting similar studies and the limitations on their use and application. Finally, lessons learned are summarized as a point of reference for future research.

Chapter 2. BACKGROUND

2.1 ENVIRONMENTAL IMPACT ASSESSMENT

Naval training activities can occur in waters that overlap with marine mammal habitats. Therefore, for marine mammal protection environmental impact assessments (EIA) to quantify the impact of the noise generated by an activity on resident marine animal species are required. These typically include predictive modelling to determine the expected noise levels from an activity; the goal being to determine an approximate range beyond which the noise levels are not expected to be harmful. This is often defined as the *mitigation zone* or the *zone of influence*. The accuracy of these predictions depends on both the propagation model that is selected as well as the inputs to this model. Farcas et. al. [30] provide a comprehensive overview of the inputs required for a noise prediction model;

a) Bathymetry data
b) Geo-acoustic seabed model
c) Water column properties
d) Surface roughness
e) Source levels

Propagation models have been widely developed for military use, however Farcas et. al. [30] explain that simple models are commonly used in EIAs. One of the simplest approaches for predicting environmental noise levels is referred to as *practical spreading* and describes the source-receiver propagation loss, PL_o, as

$$PL_o = N \log_{10} R \tag{2.1}$$

where R is the receiver range and N is a coefficient that depends on the waveguide geometry and receiver ranges [31], [32]. A commonly used value for N in Eq.(2.1) is 15, representing the $R^{3/2}$ law [33]. The range at which the law is applicable depends on water depth, H, and the seabed composition. Although simple propagation relations, like Eq. (2.1), can provide a quick guide, they can also result in significant errors in estimated noise levels.

Estimates of PL_o can be further improved by taking into account the influence of the seabed on propagation. The canonical shallow water environmental model is the Pekeris waveguide where the environment is described by a water layer over a homogeneous fluid half-space [34] or an elastic half-space [35]. Computing PL_o using this environmental model within an appropriate propagation model (analytical or numerical) allows geometric spreading and losses from sound transmission into the seabed to be taken into account. Additional losses can also be included by adding an imaginary component to the wavenumber defined by

$$k = k' + k'' \tag{2.2}$$

where k is the total wavenumber, k'' is the imaginary component of the wavenumber that control attenuation, and k' is the real component of the wavenumber defined as

$$\mathrm{k} = \frac{2\pi f}{c} \tag{2.3}$$

where f is the frequency and c is the wave speed (compressional or shear wave speed, as discussed in the next section). One school of thought is to use a fluid model that approximates the losses in the seabed caused by various loss mechanisms into a single effective attenuation [36], [37]. These effective models, while providing good agreement to measured data, do not take into the account the physical mechanisms responsible for the loss of energy in a waveguide and might not be applicable in other environments. A better approach is to approximate the seabed in a way that all relevant loss mechanisms can be accounted for as these effects can have a dramatic impact on resulting noise levels. This can require elasticity to be considered where shear waves, for which particle motion is perpendicular to the direct of travel, are supported by the medium. It can also require that other seabed compositions be considered, including layering, surface roughness, or depth dependent seabed properties.

While predictive models can be a useful tool in planning, their accuracy cannot be confirmed without validation experiments. This is accomplished through acoustic monitoring of noise

generating activities to obtain ground truth data on the resulting noise levels. Using these measurements, parameters in the predictive model can then be optimized to give more accurate predictions and provide a better understanding of the mechanisms that contribute to the propagation loss.

These validation measurements are not only valuable for benchmarking specific EIA studies; they can also be used more broadly to inform the initial stages in future EIA studies. By using data from a measurement environment with similar characteristics, appropriate propagation models and geoacoustic models can be selected early on in the process. It is important, however, that the characteristics of the measurement environment are taken into account to ensure levels are not over or under predicted. For reported validation measurements to be useful to other researchers, the measured data must therefore include meta-data that describes the measurement environment.

The discussion above can be applied to any anthropogenic underwater noise source; however, this work specifically considers explosive charges (C-4 explosive) detonated within the water column. As previously discussed, explosives have been widely used as broadband acoustic sources for decades [14]–[17]; however little of the work has focused on the metrics commonly used for reporting environmental noise. Additionally, few measurements of underwater explosions between 1 kg and 20 kg have been collected at short ranges (less than 2 km) where the sound levels are highest [10], [18], [19]. As TNT is used as a reference for explosives, the charge weights in the work are reported as the Net Explosive Weight (NEW); for example, 1 kg of C-4 explosive is equivalent to 1.34 kg of TNT and is reported in this work as a 1.34 kg charge. Additionally, many of the previous studies have been conducted in deep water where little, if any, interaction with the seabed occurred [20]–[25], [16], [17]. Thus, while empirical equations are available for both the peak pressure and the energy flux density (which is proportional to SEL) for explosions [26], their utility is limited in shallow water noise prediction as they were developed for sources in unbounded media. There is, therefore, a need for high quality explosion measurements in shallow water as well as studies to determine how the seabed affects the resulting environmental noise metrics.

2.2 ENVIRONMENT MODELS

2.2.1 *Pekeris Waveguide*

The Pekeris waveguide is the canonical environment model for propagation of sound in shallow water. It is characterized by a homogeneous water layer with thickness, H, a pressure release surface at the water air interface at a depth $z = 0$ m, and a homogeneous half-space at the water-sediment interface at $z = H$ that is characterized as either a fluid or elastic medium. In this section the waveguide is primarily considered as a shear-supporting elastic half-space with some discussion on the fluid case. A schematic of this environment is shown in Figure 2.1. For the purposes of this work, it is assumed that the source is located within the fluid layer.

Solutions of the pressure field in this environment are available from Pekeris [38], Brekhovskikh [33], Press and Ewing [39], and Ewing et. al. [40]. Following the method outline by Ewing et. al. [40], solutions for the Pekeris waveguide can be found by the use of potentials where the displacement $\bar{u} = (u_x, u_v, u_w) = (u, v, w)$ is given by

$$\bar{u} = \bar{\nabla}\phi + \bar{\nabla} \times \bar{\psi} \tag{2.4}$$

Where the scalar potential ϕ corresponds to compressional waves and the vector potential $\bar{\psi} = (\psi_x, \psi_y, \psi_z)$ corresponds to shear waves, and $\bar{\nabla}$ is the differential operator,

$$\bar{\nabla} = \left(\frac{\partial}{\partial x}, \frac{\partial}{\partial y}, \frac{\partial}{\partial z}\right) \tag{2.5}$$

Here, ∂ represents the partial derivative. Both ϕ and $\bar{\psi}$ in Eq. (2.4) are solutions to the wave equation;

$$\bar{\nabla}^2\phi = \frac{1}{{c_p}^2}\frac{\partial^2\phi}{\partial^2 t} \tag{2.6}$$

$$\bar{\nabla}^2\bar{\psi} = \frac{1}{c_s^2}\frac{\partial^2\bar{\psi}}{\partial^2 t} \tag{2.7}$$

Using the Lame parameters λ and μ, and the material density ρ, the compressional wave speed c_p is defined by

$$c_p = \sqrt{\frac{\lambda+2\mu}{\rho}} \tag{2.8}$$

And the shear wave speed β is defined by

$$c_s = \sqrt{\frac{\mu}{\rho}} \tag{2.9}$$

Ignoring the time dependence, the solutions for ϕ in Eq. (2.6) and $\bar{\psi}$ in Eq. (2.7) are given by

$$\phi_i = \left(A_i e^{jk_{zi}z} + B_i e^{-jk_{zi}z}\right)e^{jk_x x} \tag{2.10}$$

$$\overline{\psi_i} = \left(\bar{C}_i e^{j\kappa_{zi}z} + \bar{D}_i e^{-j\kappa_{zi}z}\right)e^{jk_x x} \tag{2.11}$$

Where j detonates an imaginary number ($j = \sqrt{-1}$), $i = 1$ denotes the water layer, $i = 2$ the homogeneous half-space, and A, B, C and D are coefficients. Note that the inclusion of k_x in Eq. (2.10) and Eq. (2.11) implies horizontal continuity in that this parameter is the same on either side of the interface of the water layer and half-space. The vertical wavenumbers are defined by

$$k_{zi} = \sqrt{k_i^2 - k_x^2} \tag{2.12}$$

$$\kappa_{zi} = \sqrt{\kappa_i^2 - k_x^2} \tag{2.13}$$

Where k_x is the horizontal wavenumber, and, using the frequency f, the compressional wavenumber is defined by

$$k_i = \frac{2\pi f}{c_{pi}} \tag{2.14}$$

And the shear wavenumber by

$$\kappa_i = \frac{2\pi f}{c_{si}} \tag{2.15}$$

The coefficients A, B, C and D are found using the boundary conditions. These are broken into the continuity of normal stress in the z direction σ_{zz}, shear stress along the interface τ_{zx}, and the continuity of displacement normal to the interface w. The boundary conditions for a given interface are outlined in Table 2.1. Another boundary condition, the Sommerfeld radiation condition, imposes the condition that the disturbance from a source vanishes at infinity (e.g. no upward propagating waves from the seabed at $z = -\infty$).

Writing the boundary conditions in terms of potentials gives a system of equations. Taking the determinant of this system and setting it equal to zero yields the characteristic equation of the waveguide (see Ewing et. al. p.157-161 for details)

$$\tan\left(H\sqrt{k_1^2 - k_x^2}\right)) = j\,\frac{\rho_2}{\rho_1}\frac{\sqrt{k_1^2-k_x^2}}{\sqrt{k_2^2-k_x^2}}\left[\left(1 - \frac{2k_x^2}{\sqrt{\kappa_2^2-k_x^2}}\right)^2 + \frac{4\sqrt{k_2^2-k_x^2}(\kappa_2^2-k_x^2)}{\left(\kappa_2^2-k_x^2\right)^2}\right] \tag{2.16}$$

The characteristic equation defines a set of allowable solutions of k_x. The largest, real value of k_x corresponds to a pole and defines the interface wave that propagates at a speed of roughly 10% below the slowest wave speed in the waveguide (for sandy sediments this is the shear speed). Note that the term interface wave can refer to different wave types depending on the boundary conditions of the interface; Stoneley wave between two solids, Scholte wave between a fluid and a solid, or Rayleigh wave between a solid and a vacuum. The Pekeris waveguide discussed here supports Scholte waves.

When the seabed has a higher compressional wave speed than the water, there is a point where a wave transmitted into the seabed is parallel to the boundary; this occurs at the critical angle, θ_c. For grazing angle (Figure 2.2), this is given as

$$\cos\theta_c = \frac{c_{p1}}{cp_2} \tag{2.17}$$

The wavenumber at this point is defined by $k_2 = k_1 \cos\theta_c$ and defines a branch point of the system. Physically, it corresponds to a head wave (also referred to as a ground wave, critically refracted wave, lateral wave, or more generally as a precursor arrival) [41]. At sufficient distance, the head wave is the first arriving wave [42]. A ray diagram of the head wave is shown in Figure 2.2. Head wave arrivals are used in later chapters for estimating the compressional wave speed in the seabed. The critical angle defines an important point in the system; when $k_x > k_2$ a wave incident on the water-sediment interface is totally reflected, whereas when $k_x < k_2$ the wave is partially transmitted into the seabed. This corresponds to trapped modes and the continuous spectra respectively.

One final detail worth noting is the cutoff frequency, f_c, for a waveguide with a fluid seabed, below which a mode does not propagate. From Aki and Richards [42] p.315 it is

$$f_c = \frac{c_{p,1}}{4H}\sqrt{\frac{1}{1-\left(c_{p,1}/c_{p,2}\right)^2}} \tag{2.18}$$

This is utilized in later section to investigate refraction effects within a waveguide with a depth dependent seabed.

Table 2.1. Boundary Conditions. Not included here is the Sommerfeld radiation condition as it is the same for all interface combinations.

Interface	Boundary Conditions
Vacuum-Fluid	$\sigma_{zz} = 0$
Fluid-Fluid	$\sigma_{zz,1} = \sigma_{zz,2}$ $w_1 = w_2$
Fluid- Solid	$\sigma_{zz,1} = \sigma_{zz,2}$ $\tau_{zx,1} = \tau_{zx,2}$ $w_1 = w_2$

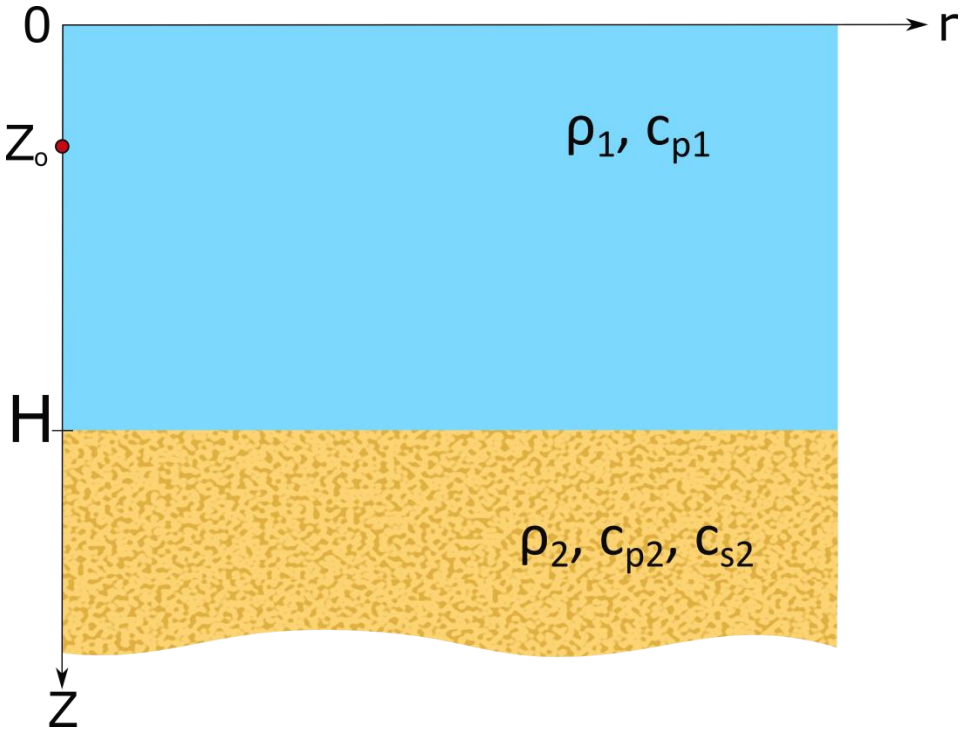

Figure 2.1. Pekeris waveguide with shear. The seabed (Z>H) is an infinite half-space

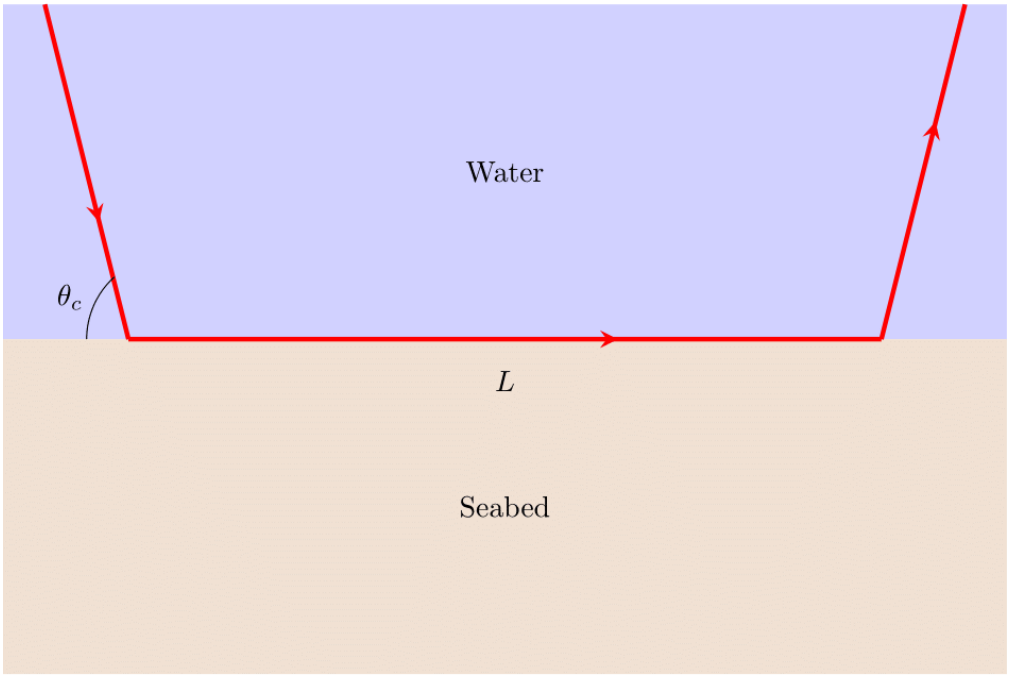

Figure 2.2. Ray schematic of a headwave arrival where θ_c is the critical angle and L is the horizontal travel distance in the seabed. Note that a headwave is continually returning energy to the wave guide and this schematic only represents a single ray-path.

2.2.2 *Depth-dependent Shear Wave Speed*

In a homogeneous medium, where the shear wave speed is constant with depth, Scholte wave dispersion is only present for frequencies whose wavelength is large compared to the thickness of the waveguide, whereas dispersion can also occur when the shear wave speed in the seabed is depth dependent [43]. In unconsolidated sediments of uniform composition (e.g. sands and clays), theoretical [44]–[46] and experimental [47] studies suggest that the shear wave speed increases continuously with depth into the seabed according to the following power law;

$$c_s(z) = c_{ob} z^{\nu} \tag{2.19}$$

In Eq.(2.19), $c_s(z)$ is the depth dependent shear wave speed, z is the depth below the water-sediment interface, c_{ob} is a constant equal to the shear wave speed at a depth of 1 m, and ν is a parameter between 0 and 1 that controls the rate at which the shear speed increases with depth. Previous studies put ν in the range of 0.3 to 0.4 [45], [47]–[50].

2.2.3 *Compressional Wave Speed and Seabed Refraction*

Similar to the shear wave speed, the compressional wave speed in sands and clays increases with depth into the seabed. This is a departure from the Pekeris waveguide case and results in more complicated propagation within the waveguide. A common approach for modelling this depth dependence is to assume that it increases linearly with depth [51]

$$c_p(z) = c_o + \beta z \tag{2.20}$$

Where c_o is the compressional sound speed at a depth of $z = 0$ m (water-sediment interface) and β is the rate of increase of the sound speed in units of s^{-1}.

If the sound speed increases with depth into the seabed, as is the case with sand, sound propagating into the ocean bottom can undergo refraction. An early study by Sachs and Silbiger [52] considers the effects of a seabed gradient on the formation of a caustic defining the point between *shadow zones*, where acoustic energy does not propagate, and *lit zones* in which energy re-enters the waveguide. The paper provides an analytical equation that relates a bilinear sound speed profile (where c_o is equal to the sound speed in the water) and the source and receiver heights to the range at which a caustic forms. A later study by Frisk [53] presents a similar analytical equation for an environment where c_o is slightly lower than the sound speed in the water.

Hanna [54], noting an unusual arrival structure in his data, investigates the effects of refraction on short-range transmission loss. It was shown that a complex arrival structure was due to the energy refracted through the seabed re-entering the waveguide at roughly 11 km for a velocity gradient, β, between 1.5 s^{-1} and 2.0 s^{-1}. At shorter ranges, predictions that ignored refracted arrivals were in good agreement with the data. A similar study by Christensen et. al. [55] compared two models; one that considered only reflections from the seabed and a second that includes refraction in the seabed. Similar to Hanna, this study showed the data were in good agreement with the reflection model at ranges less than 15 km, and in good agreement with the refraction model beyond 15 km.

Building on these studies, Stickler [56]reports on observation of negative bottom losses in depth dependent seabed where refraction occurs. This study demonstrated that that the range at which refracted energy re-entering the seabed can be observed depends not only on the sound speed profile in the seabed but also on the source and receiver heights as discussed by Sachs and Silbiger. Refracted energy from a source close to the seabed re-enters the seabed at shorter ranges than a source at a large height above the seabed (e.g. shallower source depth).

2.2.4 *Three-Layer Environment with Shear Effects*

Up until now the environments considered consist of a water layer over a sediment half-space consisting of a single material that is either homogeneous or has some type of depth dependence. In many areas, however, the seabed is more complicated and can have multiple layers that depend on both geological and biological activity. In this section a three layer waveguide (Figure 2.3) is considered that consists of a water layer bounded above by a pressure release surface, and below by a seabed composed of a thin, elastic sediment layer over an elastic half-space.

Propagation within a three-layer fluid waveguide is well established [40], [57]. However, this model does not account for losses caused by the conversion of compressional to shear waves or the conversion of shear waves to compressional waves which can occur at interfaces between two materials. Hawker [58] proposed that within a three layer waveguide with an elastic seabed there can be large effects due to the excitation of Stoneley waves on the sediment-basement interface. In this work, Stoneley wave refers to interface waves travelling along the interface of two elastic solids. This was later confirmed in a follow-up work [59] that looked at the reflection loss, RL, for a single inhomogeneous clay layer modelled as a fluid overlying a semi-infinite solid substrate (basalt) where reflection loss is defined as follows;

$$RL = -20\log_{10}|R| \tag{2.21}$$

Where R is the plane wave reflection coefficient. Following a similar line of study, Vidmar [60] used a ray path analysis to investigate the propagation of compressional and shear waves within this medium and show that high losses at low frequencies resulted from the conversion of compressional waves to shear waves at the sediment-basement interface creating a loss of energy that reduces the total energy returned to the water from the seabed.

The effects of shear related losses in the seabed were also studied by Hughes et. al. [61] where high propagation losses at regularly spaced frequencies over a finite frequency range were examined. Above a certain frequency these high losses were not observed. They compared measured propagation losses to model results for the three-layer elastic waveguide discussed here, fluid half-spaces, and elastic half-spaces. The best fit to these data were given by the three-layer elastic model. The elastic basement model (no sediment layer) gave better agreement than a fluid seabed model at low frequencies, however this model over predicted the losses at higher frequencies. Using the reflection loss calculated using the SAFARI wavenumber integration model (predecessor to OASES that is used in this work [29]) the authors show that the high losses at low frequencies are due to the excitation of shear resonances within the thin sediment layer.

Unlike Hughes et. al., Hovem and Kristensen [62] expand on the work of Hawker and explain that losses in this environment are due to the excitation of Stoneley interface waves [43] at the sediment-basement interface. They proposed that below the critical grazing angle the sediment layer produces the correct wavenumber for the excitation of interface waves to be excited along at the sediment-basement boundary. Chapman and Chapman [63] give a good explanation of this phenomena; the excitation of interface waves typically occurs at low grazing angles and low frequencies when the compressional wave speed in the sediment layer is higher than in the water. Below the critical angle at the water-sediment interface an evanescent compressional wave is excited. In thin layers, this evanescent wave can be strong enough to excite interface waves in the basement. In thick sediment layers, however, the exponential decay of the evanescent wave weakens the wave incident on the sediment-basement boundary so that an interface wave is either not excited or only weakly excited. To summarize, the evanescent wave in the thin layer is strong enough to interact with half-space below whereas in a thick layer the evanescent wave has decayed before it can interact with the half-space.

Building on the papers by Hughes et. al. and Hovem and Kristensen, Ivansson [64] demonstrates that both mechanisms contribute to the losses. Shear resonances appear as high losses at distinct

frequencies, whereas the conversion to interface waves is isolated to a range of low frequencies with the effects diminished at a high frequency cutoff.

As many of the studies relied on the plane wave reflection coefficient to study the three layer waveguide with an elastic seabed, Vidmar and Foreman [65] proposed a plane wave reflection coefficient model using a Thomson-Haskell matrix approach (for additional details on this method see [42]). While this approach can yield accurate results, it can suffer numerical instabilities. An intuitive understanding of the physics involved can also be lost in the numerical computations. In response, Chapman and Chapman [63] proposed a simple analytical coherent ray based model. It assumes that (i) there are no wave conversions at the water-sediment interface (e.g. compressional to shear wave or shear wave to compressional, and (ii) along a particular ray path, only two wave conversions can occur at the sediment basement boundary (Figure 2.4). This analytical model relies on the plane wave reflection coefficients. It should be noted that while the authors recommend the coefficients described by Brekhovskikh [33], these can be numerically unstable. It is therefore recommended that the coefficients presented in Aki and Richards [42] on pp.144 – 145 be used instead. The approximate reflection coefficient is given by;

$$R \approx R_{12} + (1 - R_{12}^2)\left(\frac{R_{23}^{pp} e^{j\Delta\phi_p}}{1+R_{12}R_{23}^{pp} e^{j\Delta\phi_p}} - \frac{R_{23}^{ps}R_{23}^{sp} e^{j(\Delta\phi_s+\Delta\phi_p)}}{\left(1+R_{12}R_{23}^{pp} e^{j\Delta\phi_p}\right)^2\left(1+R_{23}^{ss} e^{j\Delta\phi_s}\right)}\right) \qquad (2.22)$$

Where R is the reflection coefficient, the first subscript number indicates the incident medium, the second subscript number indicates the medium from which the ray is reflected/transmitted. The first superscript letter indicates the type of incident wave (p for compressional, and s for shear) and the second superscript letter indicates the nature of the reflected/transmitted ray. Phase effects resulting from the thin sediment layer are included in all coefficients in the middle layer with ϕ_p identifying the phase of compressional waves and ϕ_s the phase of the shear waves.

The Chapman-Chapman model can be broken down into several components; R_{12} identifying the reflection from the water-sediment interface, the left-hand side of the large term in parentheses identifying a family of compressional waves travelling through the sediment layer, and the right-hand side identifying compressional to shear wave conversions. A similar reflection coefficient

model for this environment have also been proposed by Clark [66] and a three layer elastic medium has been presented by Ainslie [67]; however, the Chapman-Chapman model is used in this work due to its simplicity and utility in elucidating the underlying mechanisms responsible for the high losses in this environment.

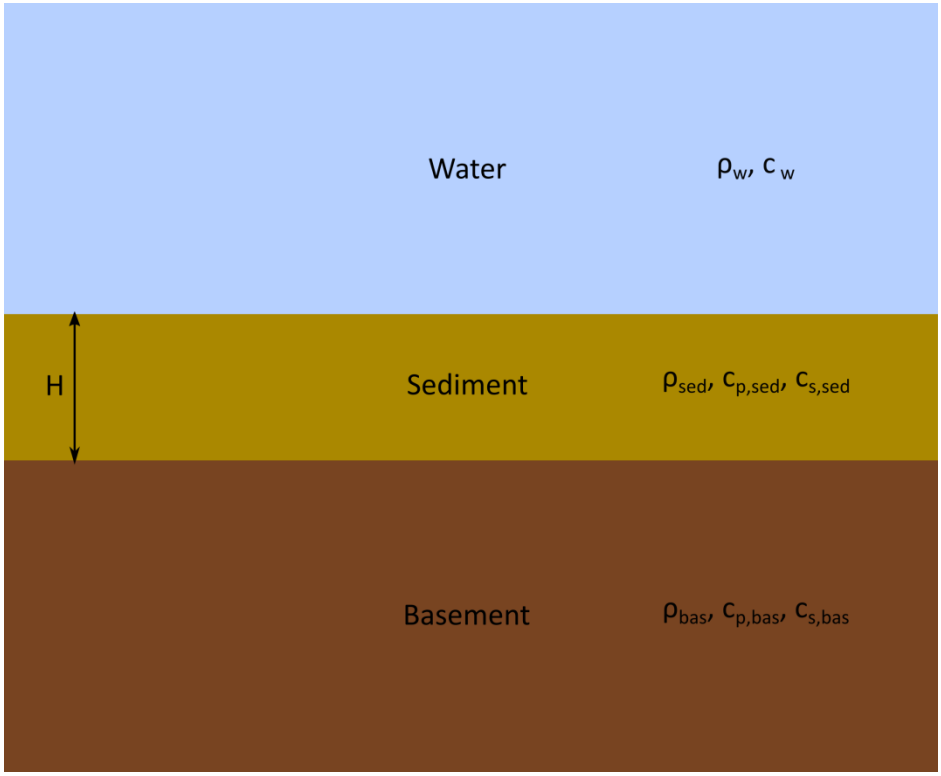

Figure 2.3. Three-layer seabed model with a thin layer of thickness H

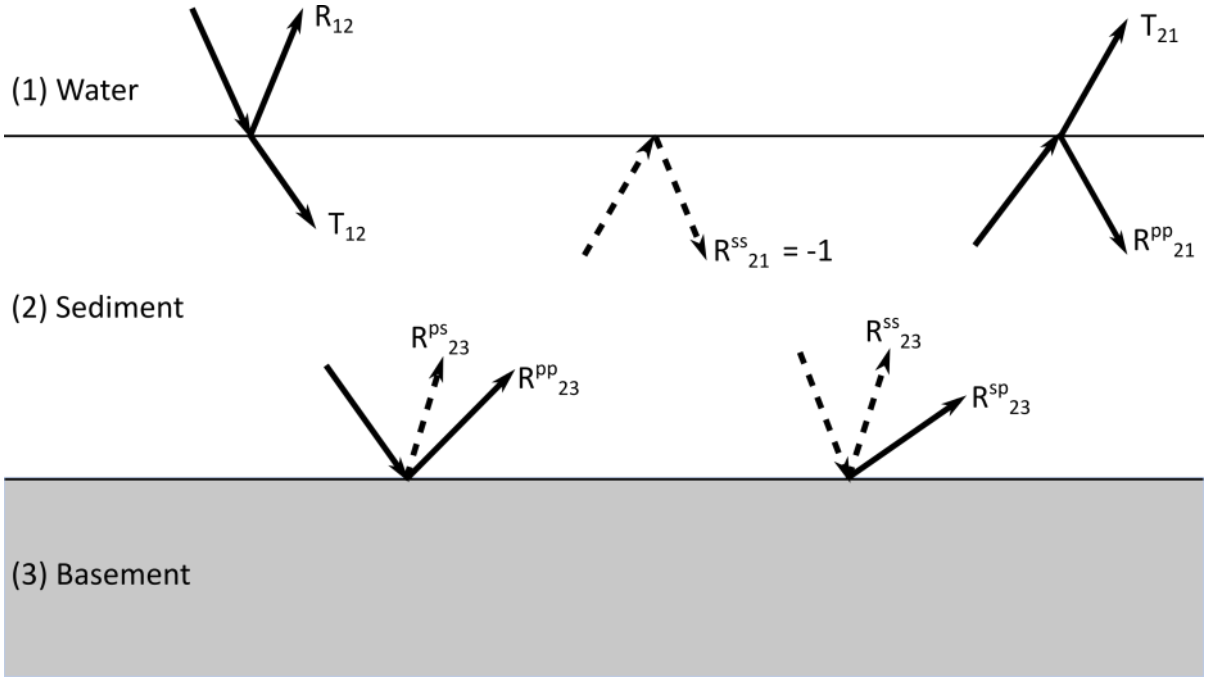

Figure 2.4. The important reflection and transmission coefficients for a solid sediment layer with a low shear speed used in the Chapman and Chapman reflection coefficient model (based on figure by Chapman and Chapman [63])

2.3 UNDERWATER EXPLOSIONS

Having considered the physics of sound propagation in shallow water, attention is turned to the source used in this work; underwater explosives. Chapman [16] provided a relatively recent review and discussion of the general characteristics of underwater explosions. During the detonation of an underwater charge, the explosive material is transformed into a small sphere of gas at high temperature and pressure. As a result of the pressure differential between the gas sphere and the hydrostatic pressure in the water, a shock wave is radiated into the water. Following detonation, the gas sphere begins to expand outward resulting in a pressure tail behind the shockwave that exponentially decreases in magnitude. As the bubble expands, the pressure inside begins to decrease. When the pressure inside the bubble reaches the hydrostatic pressure of the water, the inertia of the moving gas causes the bubble to continue to expand. This continued expansion of the gas results in the pressure within the gas sphere falling below the hydrostatic pressure. Eventually the gas sphere ceases to expand. With the pressure inside the gas sphere now below the hydrostatic pressure, the bubble begins to contract thereby increasing the

internal pressure. Similar to the expansion process, the inertia of the gas bubble causes the pressure within the sphere to increase past the hydrostatic pressure. This process of expansion and contraction, collectively referred to as the *bubble pulse*, continues until the energy within the gas sphere has been radiated into the water. A representative pressure history of the explosive waveform as it relates to the size of the gas sphere is shown in Figure 2.5. The time between the shock arrival, P_{peak}, and the peak pressure of the bubble pulse P_1, is referred to as the bubble pulse period, τ.

The process described above is representative of an underwater explosion in an unbounded medium in which there is no interaction with nearby surfaces. Recent studies by Cui et. al. [68] have looked at how a nearby surface can affect the bubble pulse including rigid surfaces and pressure release surfaces. In a real ocean environment, these would correspond to the seabed and sea surface respectively. The proximity of an explosion to a free surface can result in cavitation effects where the pressure within the cavitation zone is lower than the pressure in the water and expands outward from the center of the free surface. Additionally, atmospheric air can be ingested by the bubble when it is in close enough proximity to the surface. When a charge is located above a rigid surface cavitation can occur as well as other effects including the formation of annular jets and the separation of the gas bubble into two parts as a result of buoyancy effects. For both of these surfaces, the pressure time series of the source would deviate from the idealized model shown in Figure 2.5.

2.4 BUBBLE PULSE PERIOD

Using measurements of explosions, empirical equations for the bubble pulse period as a function of charge weight and explosion depth were developed. Specifically, this equation predicts the time delay between the arrival of the shock wave and the first bubble pulse peak. Although originally formulated using measurements of deep underwater explosions [69], this equation has previously been successfully applied to shallow charges [16]. The bubble pulse period is given by;

$$\tau = 2.11 \times W^{1/3} z_o^{-5/6} \tag{2.23}$$

where τ is the bubble pulse period in seconds (s) (Figure 2.5), w is the charge weight in kg NEW and z_o is the hydrostatic depth in meters (given by $z_o = W + 10.1$ m). Unlike the peak pressure equation, which is a function of scaled range, the bubble pulse period is a function of charge weight and detonation depth. It should be consistent for measurements collected simultaneously at multiple ranges.

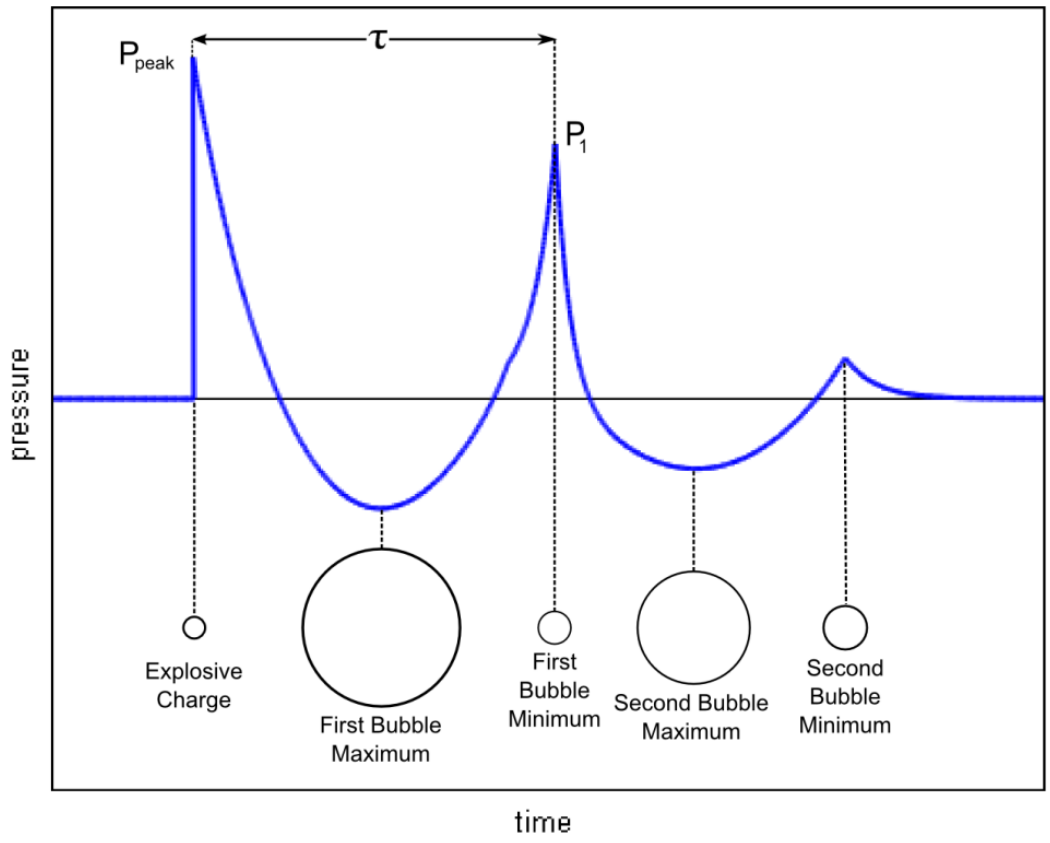

Figure 2.5. Pressure-time history for an underwater explosion with the size of the gas sphere is shown in relation to the explosion waveform [25].

2.5 ENVIRONMENTAL METRICS

2.5.1 *Peak Pressure*

Using experimental measurements of underwater explosions collected during and after World War II, a semi-empirical equation for predicting the peak pressure from underwater explosions was developed as a function of the scaling parameter, or $R/W^{1/3}$, defined as the range from the source, R, divided by charge weight, W, to the one-third power (herein referred to as scaled range.) The term semi-empirical has been used to describe this peak pressure equation due to the origins of this parameter in Kirkwood-Bethe propagation theory [70]. The peak pressure [20] is given by;

$$P_{peak} = 52.4 \times 10^6 \left(\frac{R}{W^{1/3}}\right)^{-1.13} \tag{2.24}$$

where $P_{peak}\ is$ the peak pressure in Pascal (Pa), R the measurement range in meters (m), and W the charge weight in kilograms of TNT, also referred to as the net explosive weight (NEW). It is important to note that this equation was developed for TNT, due to its historical and continued use as the standard high explosive, and assumes a spherical TNT charge of density 1520 kg/m^3 [26]. Using this equation, the peak pressure for other high explosives can be predicted through the use of TNT-equivalent weight. While originally formulated for spherical charges, the equation has been successfully employed for an array of charge geometries [16], [71]–[73].

While a full derivation of the Kirkwood-Bethe theory is outside the scope of this dissertation, it has been shown [26] that the pressure in the water decays exponentially with time, and is dependent only on the explosive material and the ratio of the range to the charge radius, R/a_o. The peak-pressure equation assumes a spherical charge geometry where the charge weight is given by $W = \rho\frac{4}{3}\pi a_o^3$ where ρ denotes the density of the explosive material. With this in mind, the ratio R/a_o can be reformulated as;

$$\frac{R}{a_o} = \frac{R}{w^{1/3}} \times \left(\rho\frac{4}{3}\pi\right)^{1/3} \tag{2.25}$$

In the peak-pressure equation $\left(\rho\frac{4}{3}\pi\right)^{1/3}$ is absorbed into the 52.4×10^{6} factor. Additionally, the Kirkwood-Bethe theory supports the $R^{-1.13}$ decay of the peak pressure with range, which is a somewhat greater decay rate than the R^{-1} decay expected for spherical spreading of an acoustic wave [26]. This departure could be due to weak non-linear effects; this was discussed in detail by Temkin [74], although conclusive explanation was not reached.

2.5.2 *Sound Exposure Level*

The sound exposure level (SEL) is the time integral of the squared acoustic pressure;

$$\mathrm{SEL} = 10\log_{10}\left(\frac{1}{p_{ref}^{2}}\int_{0}^{T}p^{2}(t)dt\right) \tag{2.26}$$

where SEL is in units of dB referenced to p_{ref}, which in this case is 1 μPa^{2}s. Popper [75] explained that SEL is an indication of the total acoustic energy received by an organism. It has become a useful metric to assess cumulative noise exposure as it allows for the comparison of sounds with varying durations [76]. The most common approach to calculating the SEL is the 90% energy approach. Using this approach, the integration period, T, is defined as the sample interval that includes 90 percent of the energy of the explosion's waveform. An example of this calculation is shown in Figure 2.6

Energy flux density, E, is defined as the time integral of the squared pressure divided by the characteristic impedance of the medium and is closely related to the SEL in Eq. (2.26). similar to the peak pressure equation (Eq. (2.24)), the energy flux density is proportional to the scaled range $R/W^{1/3}$ [26]

$$\mathrm{E} \propto \mathrm{W}^{1/3}\left(\frac{\mathrm{R}}{\mathrm{W}^{1/3}}\right)^{-2.12} \tag{2.27}$$

where W is the charge weight and R is the range. This relation has been shown to be useful for comparing the SEL for different combinations of charge weight and measurement range.

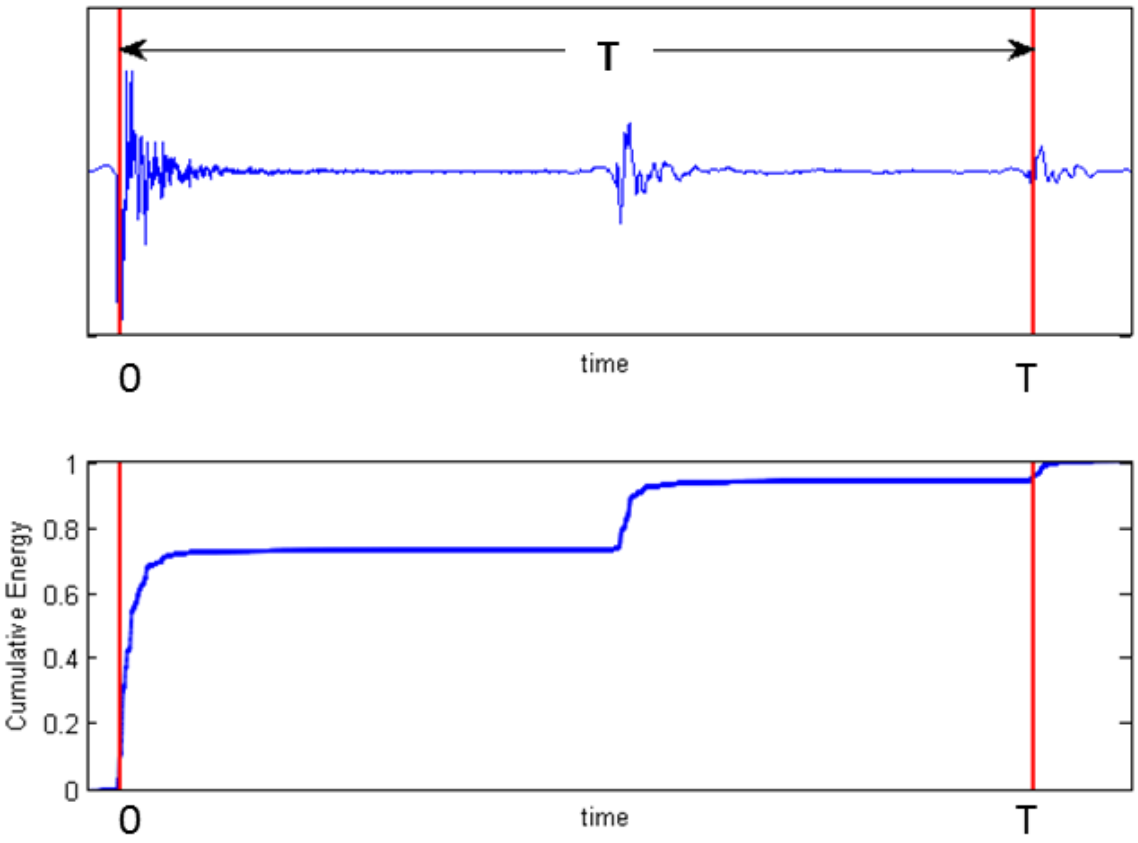

Figure 2.6. a) Time history of an explosion and b) the resulting time history of its cumulative energy. Red lines indicated the start and end times of the window containing 90 percent of the waveform energy.

Chapter 3. EXPERIMENTAL DESCRIPTIONS

In the following chapter experimental descriptions for experiments discussed in this work are presented.

3.1 PU`ULOA EXPERIMENT

The underwater explosion measurements were conducted over a three day period from May 17 to 19, 2016 at the U.S. Navy Pu`uloa Underwater Detonation (UNDET) Range at Pearl Harbor, HI (Figure 3.1). Each day three, C-4 charges of identical weight were prepared, deployed and detonated by the U.S. Navy Mobile Diving and Salvage Unit ONE, Company 1-8. The charge weights, reported as the net explosive weight (NEW), were 2.3 kg NEW on day 1, 8 kg NEW on day 2, and 4.5 kg NEW on day 3. All charges were detonated on the seabed. The charges are summarized in Table 3.1. The third 8 kg NEW charge detonated on day 2 misfired and is therefore not included in this study.

Acoustic measurements of the UNDETs were recorded simultaneously from two directions: one aligned cross-shore (Figure 3.2a) and one aligned alongshore (Figure 3.2b). For cross-shore measurements, these data were recorded on a vertical line array (VLA) deployed from the motor vessel Ho`oponopono (chartered from Parker Marine Corporation, Honolulu, HI). The VLA consisted of 9 hydrophones (ITC 1032) spaced 2 m apart, and had receiving voltage sensitivities ranging from -204 to -208 dB re V/μPa depending on their position on the VLA. Data from the VLA were recorded on a multi-channel coherent data acquisition system (Astro-Med, Inc.) for which each channel was recorded at 62,500 samples per second. The water depth along this transect varied from 10 m at the UNDET site to 18 m at the receiver range (Figure 3.1).

For alongshore measurements, single-element autonomous systems were deployed near the seabed and consisted of a self-contained data acquisition and storage system (Loggerhead Instruments DSG) and a single hydrophone (HTI-96-min) recording at 50,000 samples per second with a receiving voltage sensitivity of -220 dB re 1 V/μPa. The water depth along this transect varied between 8 and 10 m. For days 1 and 2 the single element systems were deployed 750 m and 1500 m down-range from the UNDET and on day 3 at 500 m and 1500 m.

At range 1500 m, on all three days, a third system was deployed that had receiver sensitivity of -170 dB re 1 V/μPa. This high sensitivity system enabled studies of ambient noise conditions immediately before, during, and after an UNDET event; it also provides recording details of the low-frequency precursor signal that arrives prior to the direct, high-level signal which is used in Chapter 5 for calculating an estimate of the compressional wave speed in the seabed. Note, that while precursor arrivals can be observed on the low sensitivity system, only the high sensitivity system can fully resolve the beginning of this feature. In the low sensitivity system, this feature has a low signal-to-noise ratio so the arrival time that can be observed in the high sensitivity system cannot be resolved. Depths and ranges for the receivers shown in Figure 3.2 are approximate. Precise values are given in Table 3.1.

Sound speed in the water column was measured at the VLA site on 17, 18, and 19 May between 2030 and 2200 UTC. The measured sound speed was between 1536 and 1537 m/s and was nearly constant with depth; this was expected for this environment because of mixing from wave action. Directional wave conditions were also measured at the VLA site using a Datawell wave buoy. Wave conditions over the three day experiment were consistent and show waves of frequency 0.18 Hz originating from approximately 135 degrees, and a 0.1 Hz, low-frequency swell component originating from 180 degrees where 0 degrees corresponds to North. The root-mean-square wave height is 0.33 m and the significant wave height is 1.34 m. Directional wave conditions over the three days are consistent.

Seabed studies conducted in the vicinity of the measurement site show the seabed is composed of limestone [77] overlain by a coral sand layer of variable thickness [78]. This has been confirmed by images collected by the dive team that show the seabed composition exhibits significant spatial variation with some areas presenting only limestone pavement and in others the limestone is topped by sand. Additional information on this study can be found in the report by Dahl et. al. 2016 [79].

Table 3.1. Test charge summary for the Pu`uloa experiment. Note that the tripod color designations refer to the schematic in Figure 3.1.

Date	Weight (kg NEW)	Detonation Depth (m)	Receiver Range Orange Tripod (m)	Receiver Depth Orange Tripod (m)	Receiver Range Green Tripod (m)	Receiver Range Green Tripod (m)
17MAY2016	2.3	10.3	758	7.1	1503	7.7
18MAY2016	8	10.6	784	7.1	1503	8.0
19MAY2016	4.5	10.3	513	8.1	1503	7.7

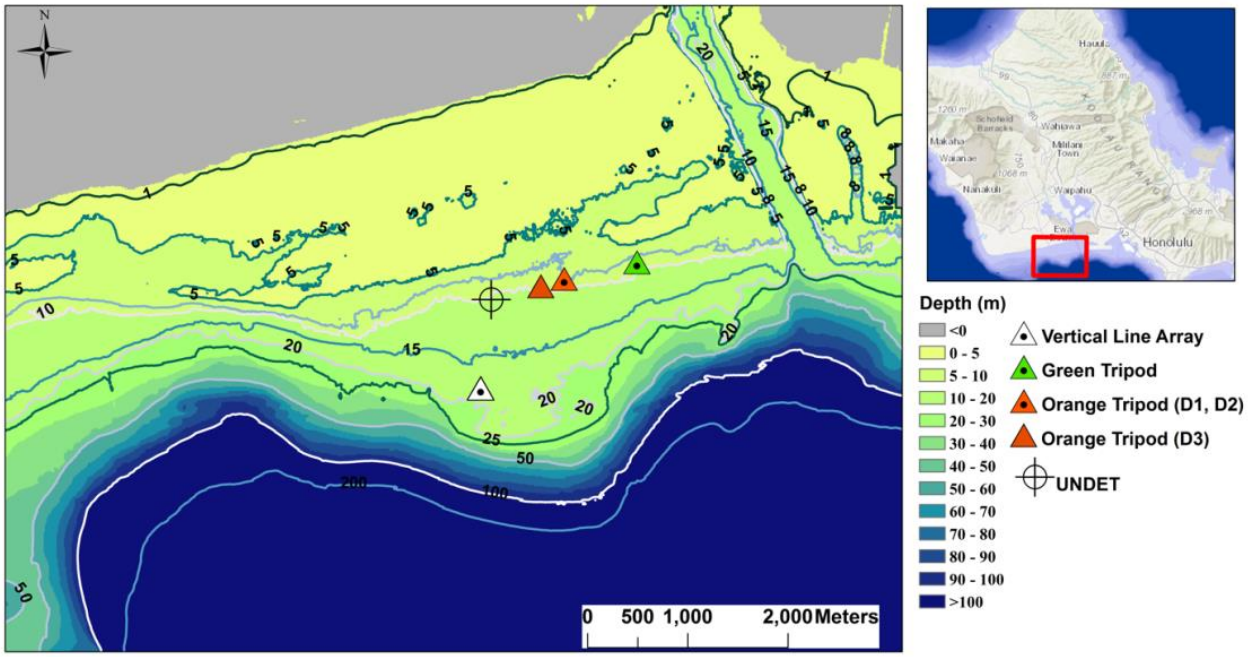

Figure 3.1. Map of the measurement geometry and bathymetry for the 3-day Pu`uloa Range experiment in May 2016, showing locations of the UNDET source, charter vessel and deployment of vertical line array (white triangle), and the two autonomous recording tripod systems (green and orange triangles). Note the orange system was repositioned closer to the UNDET site on day 3 (map by Dara Farrell).

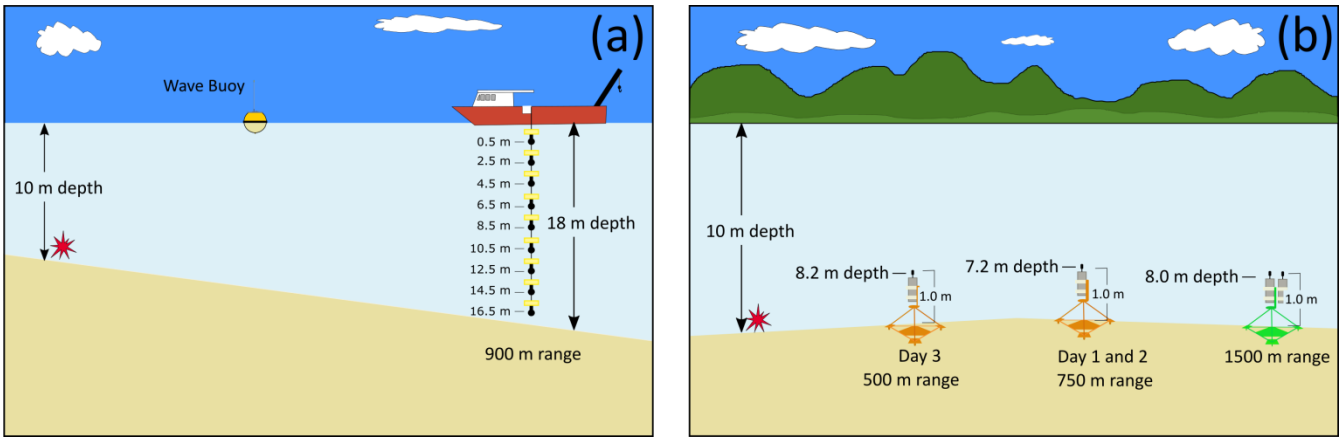

Figure 3.2. Equipment setup for (a) the off shore receiver range measured on a vertical line array and (b) The cross-shore measurement location of the two autonomous systems. The 750 m autonomous system was moved to 500 m on day 3.

3.2 VIRGINIA BEACH EXPERIMENT

The Virginia Beach measurements were originally presented by Soloway and Dahl 2014a [19]. Five explosive charges were detonated either on the seabed or at a depth of approximately 9 m. The NEW of the charges ranged from 0.1 to 6 kg NEW. The measurement site was located 7 km off the coast of Virginia Beach, Virginia in shallow water with constant water depth along the measurement transect. Exact measurement of the water depth were not unfortunately not collected during the experiment, so the water depth has been estimated using the bubble pulse period of the 6 kg charge detonated on the seabed and Eq. (2.23). This put the water depth at 16 m. To help verify that the bubble pulse provides a reasonable water-depth estimate, a comparison is made to the water depths listed on navigational charts. The navigational charts show a constant mean lower-low water depth of 14.3 m; when tidal variation is accounted for, the water depth is between 14.7 m and 15 m. As the isobaths exhibit some spatial variation, the 1 m discrepancy is reasonable. A water depth of 16 m is therefore used in the remainder of this work.

which is the value that is used here as the nautical charts do not provide exact. Acoustic data were collected simultaneously at either 165 m and 430 m or 430 m and 950 m along an isobath. As part of an unrelated sand-mining study conducted by conducted by Hardaway et. al. [80] at a nearby site, 22 seabed core samples were collected over a 16 km^2 area. These core samples

contained a range of materials from stiff clays to very coarse sands and gravels[80]. A study by Soloway and Dahl 2015b [81] also showed that the seabed is likely composed of sandy sediments. A summary of measurement ranges and depths is given in Table 3.2.

Measurements were made from two small vessels; Vessel 1 located at range 430 m from the source detonation site for tests 1 - 4 and Vessel 2 located at range 165 m for tests 1 and 2 and at range 950 m for tests 3 and 4 (Figure 3.3). Acoustic data were recorded from Vessel 1 using a vertical line array (VLA), and an autonomous acoustic recording system. The VLA elements consisted of 9 hydrophones (ITC 1032) with receiving voltage sensitivity ranging from -204 to -208 dB re V/μPa depending on the position in the VLA. The elements were spaced 0.7 m apart with the uppermost hydrophone at depth 6.6 m and the deepest at 12.2 m. The autonomous system recorded at depth 12.9 m and consisted of a self-contained data acquisition and storage system (Loggerhead Instruments DSG) and a single hydrophone (HTI-96-min) recording at 50,000 samples per second with a receiving voltage sensitivity of -220 dB re 1 V/μPa. An identical autonomous system was used for Vessel 2 and was deployed at depth 9.5 m for tests 1 and 2 (165 m range) and depth 10.0 m for tests 2 and 4 (950 m range). Additional measurement details for the Virginia Beach experiment can be found in the report by Soloway and Dahl 2014b [27] or in Appendix A where the experimental description from this report has been included for completeness.

Table 3.2. Summary of the charge weights and measurement locations for the Virginia Beach, VA experiment

Date	**Weight (kg NEW)**	**Detonation Depth (m)**	**Receiver Range Vessel 1 (m)**	**Receiver Depth Vessel 1 (m)**	**Receiver Range Vessel 2 (m)**	**Receiver Depth Vessel 2 (m)**
11SEP2012	0.3	9	430	12.9	165	9.5
11SEP2012	0.6	14.7	430	12.9	165	9.7
11SEP2012	3.0	9	430	13.1	950	10.0
11SEP2012	6.0	14.7	430	13.1	950	10.4

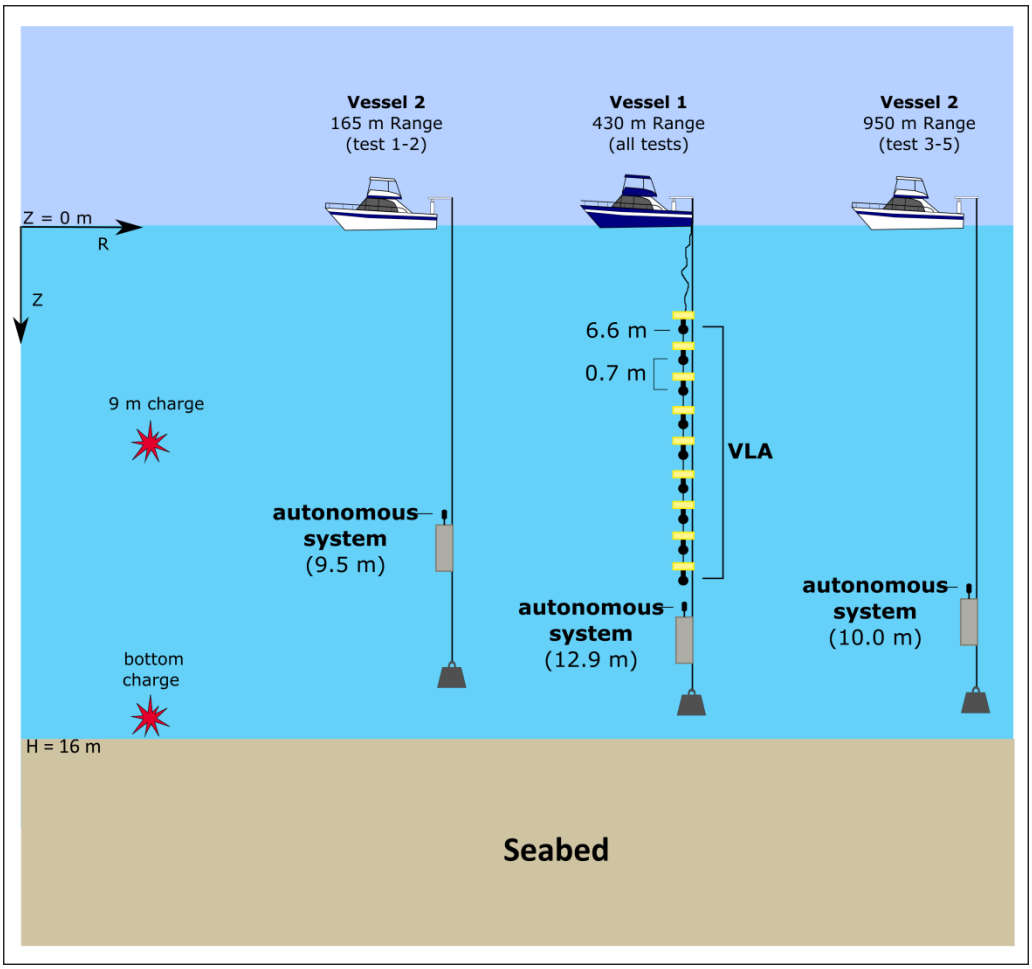

Figure 3.3. Experiment setup for the Virginia Beach experiment

3.3 SAN DIEGO EXPERIMENT

The Silver Strand experiment was conducted at the Silver Strand Training Complex, Naval Base Coronado, Coronado, CA. Over two days, four 6 kg NEW explosive charges were detonated on the seabed at a depth of 23.7 m. Charges were recorded simultaneously at two ranges along an isobaths. The exact range of each receiver varied from charge to charge, with one receiver at a range between 350 and 800 m from the detonation site, and a second, farther range, between 1200 and 1700 m. A summary of the receiver depths and measurement ranges can be found in Table 3.3.

The seabed at this measurement site, similar to the Virginia Beach experiment, was composed of sand. Unlike the Virginia beach site, the water sound speed at the Silver Strand experiment site was characterized by a thermocline between the surface and approximately 15 m, resulting in a sound speed that varied from 1510 m/s near the sea surface to 1492 m/s near the seabed, with sound speed in the bottom 10 meters of the water column being approximately constant. Additional experimental details can be found in the report by Soloway and Dahl 2015a [28] or in Appendix B where the experimental description from this report has been included for completeness.

Table 3.3. Summary of the charge weights and measurement locations for the Silver Strand experiment

Date	**Weight (kg NEW)**	**Detonation Depth (m)**	**Receiver Range Vessel 1 (m)**	**Receiver Depth Vessel 1 (m)**	**Receiver Range Vessel 2 (m)**	**Receiver Depth Vessel 2 (m)**
13MAY2014	6.0	22	512	12.3	1255	15.7
13MAY2014	6.0	22	784	12.3	1499	15.7
14MAY2014	6.0	22	685	13.1	1651	19.9
14MAY2014	6.0	22	358	13.1	1353	19.9

Chapter 4. MODELING AND EXPERIMENTS EXAMINING EXPLOSION GENERATED SCHOLTE WAVES IN SANDY SEDIMENTS WITH POWER LAW DEPENDENT SHEAR WAVE SPEED

4.1 INTRODUCTION

This chapter demonstrates how numerical propagation models and observable features in the data can be utilized to develop an understanding of the measurement. The detonation of explosive charges in shallow water from marine construction activities and navy training exercises generates high amplitude, broad-band noise levels, some of which are potentially hazardous to nearby marine life [73]. The lowest frequencies generated by such explosions (1-20 Hz) typically propagate along the interface between the water and the seabed as Scholte waves, which are the focus of this chapter.

At the interface of two homogeneous half-spaces where the shear wave speed is constant with depth, Scholte waves are non-dispersive, whereas at the interface of a finite water layer and a homogeneous half-space weak dispersion can occur when the wavelength is large compared to the layer thickness (see Eq. (2.16)). Dispersion can occur to a significantly greater degree when the shear wave speed in the seabed is depth dependent [43]. In unconsolidated sediments that are un-layered and of uniform composition (e.g. sands and clays), theoretical [44]–[46] and experimental [47] studies suggest that the shear wave speed increases continuously with depth into the seabed according to the power law in Eq. (2.19) where $c_s(z)$ is the depth dependent shear wave speed, z is the depth below the water-sediment interface, c_{ob} is a constant equal to the shear wave speed at a depth of 1 m, and ν is a parameter between 0 and 1 that controls the rate at which the shear speed increases with depth.

In a previous paper [19], measurements of the noise produced by the detonation of explosive charges in shallow water at the Virginia Beach measurement site were presented. During this

experiment, Scholte waves generated by a C-4 charge with 3 kg-TNT equivalent weight detonated at a depth of 11.6 m, and a C-4 charge with 6 kg-TNT equivalent weight detonated on the seabed at 16 m, were measured on a vertical hydrophone array that sampled the water column between 6.4 and 12.1 m.

The main goal of this work is to assess whether the explosion-generated Scholte waves traveling in the sandy seabed at the measurement site can be modeled using a power law dependent shear wave speed profile. This is accomplished using the dispersion of the Scholte waves and Eq.(2.19) to determine the shear wave speed profile in the seabed through a forward modelling approach.

Furthermore, in this study we also employ an empirical source model from Chapman [16], [17] that determines the pressure time-series of an explosion at 1 m from the source as a function of TNT-equivalent charge weight. It is particularly appropriate for this study given that this source model was developed using multiple measurements collected in shallow water and can be applied to varying charge weights. This approach differs from previous studies involving Scholte waveforms that have used, for example, source functions based on a Ricker wavelets with a center frequency of 10 Hz or 20 Hz where the source model is not directly connected to TNT-charge weight [82], and a volume seismic source with strength estimated using adiabatic bubble theory [83].

This volume is the difference between the volume initially occupied by the unexploded charge and the volume occupied by the combustion products at the end of the process.

4.2 ENVIRONMENT MODEL

Scholte waves generated by the detonation of a 3 kg-TNT equivalent and a 6 kg-TNT equivalent charge were measured on a 9-element vertical line array at a range of 430 m with an uncertainty of ±50 m owing to vessel drift. All measurements discussed in this paper were recorded on the deepest hydrophone, 12.1 m below the surface (3.9 m above the seabed). Additional details on

the experiment can be found in Chapter 3 or in Soloway and Dahl [19] (experiment description from this report has been included in Appendix A for completeness).

As the exact composition of the seabed is unknown, a laterally homogeneous seabed with a depth dependent shear wave speed described by Eq. (2.19) has been assumed. Following previous studies, the density in the seabed is assumed to be constant with depth [82], [84] and is set equal to 1700 kg/m^3. Similarly, the compressional wave speed, which has little influence on the Scholte wave dispersion, is assumed to be 1700 m/s. Finally, a shear attenuation factor of 1.0 dB/λ and a compressional wave attenuation factor of 0.2 dB/λ have also been assumed.

4.3 METHODOLOGY

Previous investigations have determined the shear speed profile through two main methods; matching the group and phase speeds of Scholte waves [50], [85], and matching of the measured data to synthetic time series [82]. Here we use the latter approach and find values for $c_o$and ν in Eq. (2.19) that give the best fit to our data using a forward modelling technique that iterates through a predetermined parameter space for c_{ob} and ν. The best fit is given by the model parameters that minimize the L^2 norm calculated from the difference of the measured and modeled data. Since the spectrum of the measured Scholte wave is in the range of 1 to 10 Hz, the data have been first band-pass filtered between 1 and 15 Hz and then down-sampled from 62,500 samples/s to 200 samples/s. Processing the data in this way greatly reduces the computation time for each forward model run.

During the experiment the source and receiving equipment were not synchronized, so an alternate method had to be employed to determine the source-receiver timing. By assuming the first water arrival corresponds to the peak pressure, the source-receiver time could be determined using the measured water sound speed, 1528 m/s, and the measurement range, 430 m. This puts the peak pressure arrival at time 0.28 s.

Forward modeling is achieved using the OASES seismo-acoustic wave propagation code [29] which computes the frequency dependent Green's function for a given environment using the

parameters described in the previous section as model inputs. The forward modeling iterates over a parameter space of c_{ob} in the range 90 to 110 m/s with 1 m/s discretization, and ν in the range 0.2 to 0.4 discretizing by 0.001. Outside this parameter space, the spectra of the modeled Scholte waves were in poor agreement with the measured data, as the Scholte wave arrived either before or unrealistically long after the arrival time of the data; these values were therefore not considered in the forward modeling. The time series are then computed by taking the inverse Fourier Transform of the Green's function weighted by the spectrum of the empirical source model from Chapman [16], [17], also sampled at 200 samples/s. As OASES describes the environment using a series of horizontally stratified layers, the continuous seabed described by Eq. (2.19) is discretized using an equal layer travel time approach originally described by Godin and Chapman [45] (also discussed in Section 6.4.2). In this approach, the shear wave speed is selected such that the travel time though each discrete layer is the same. As the shear wave speed increases with depth, the layer thicknesses also increase with increasing depth. The seabed is modeled using 78-layers with a homogeneous half-space beginning at 150 m below the water-sediment interface.

4.4 RESULTS AND DISCUSSION

4.4.1 *Scholte Wave Measurements*

The figures in this section originally appeared in the report by Soloway and Dahl 2014 [27] and have been included here for completeness. Time series of the Scholte waves measured on the deepest hydrophones of the vertical line array (VLA) are shown in Figure 4.1 and Figure 4.2 for the 3.0 kg and 6.0 kg charges. The main water arrival and bubble pulse can be observed between 0 s and 0.25 s with the low frequency Scholte waves coming in between 1s and 4 s.

Looking at the energy spectral density (ESD) of these data on the VLA (Figure 4.3 and Figure 4.4), the energy carried by the Scholte wave is in the very low-frequency range between 1 and 10 Hz for both tests. Deeper hydrophones (those closer to the water-sediment interface) typically measured higher levels than hydrophones at shallower depths. Scholte waves correspond to a pole in the characteristic equation (Eq. (2.16)) and decay exponentially away from the water-sediment interface; these results are therefore expected. While the ESDs for the two tests showed

some similarities, the ESD levels for Test 3 were typically lower than the Test 4 levels, likely a result of the smaller charge weight and shallower detonation depth. Hydrophone 2 (11.7 m) has not been included due to noise present in the signal.

A spectrogram of the Scholte waves (Figure 4.5 and Figure 4.6) show low frequencies arriving first followed by higher frequencies. This is expected for Scholte waves in an environment where the shear waves are depth dependent according to Eq. (2.19). In a Pekeris waveguide, shear dispersion still occurs due to the $\tan\left(H\sqrt{k_1^2 - k_x^2}\right)$ term in Eq. (2.16), although it is only weakly dispersive at a narrow range of frequencies. When the waveguide thickness, H, is large compared to the wavelength, the dispersion equation tends towards the dispersion equation for a layered waveguide defined by a water half-space above an elastic half-space. When H is small compared to the wavelength, the dispersion equation tends towards the Rayleigh wave equation for an elastic half-space below a vacuum.

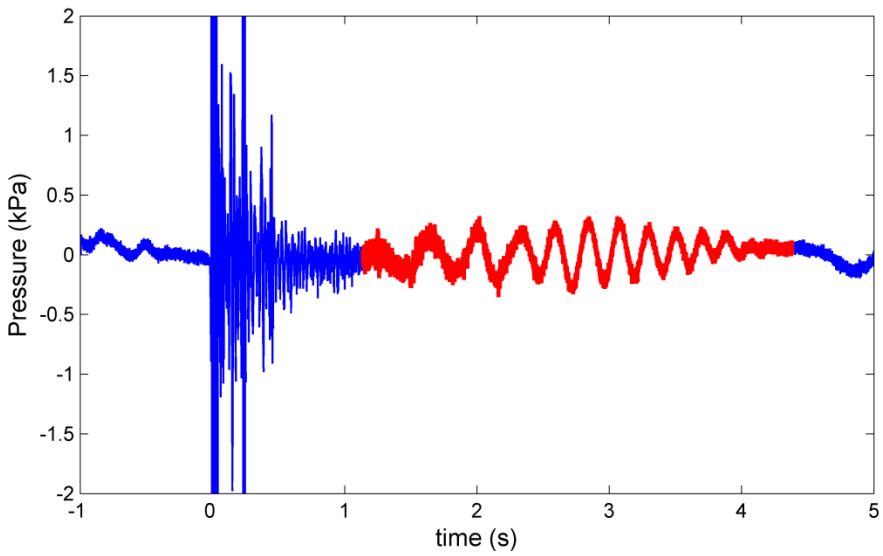

Figure 4.1. Time series of the 3 kg NEW charge measured at 430 m on hydrophone 1 of the VLA (12.4 m) with the Scholte wave arrival indicated in red. On the time axis, time 0 s corresponds to the predicted time of arrival of the pressure wave at 430 m.

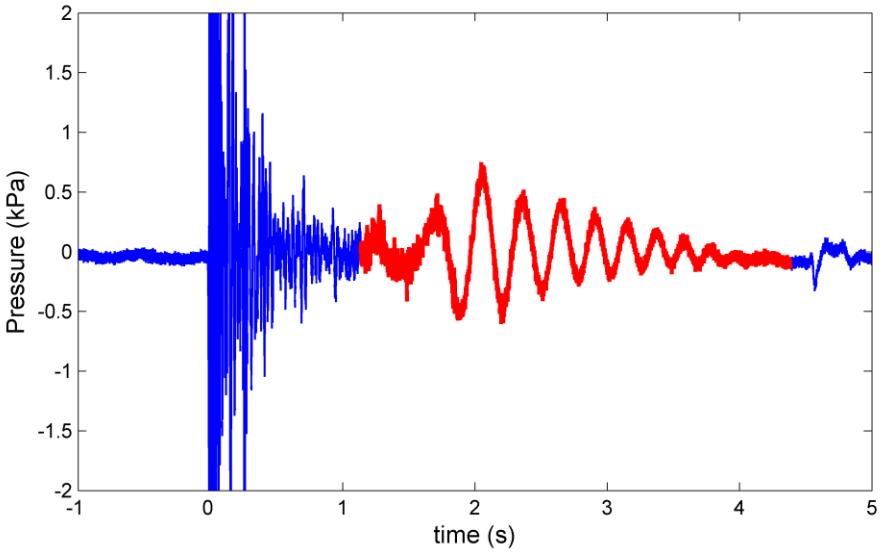

Figure 4.2. Time series of the 6 kg NEW measured at 430 m on hydrophone 1 of the VLA (12.4 m) with the Scholte wave arrival indicated in red. On the time axis, time 0 s corresponds to the predicted time of arrival of the pressure wave at 430 m.

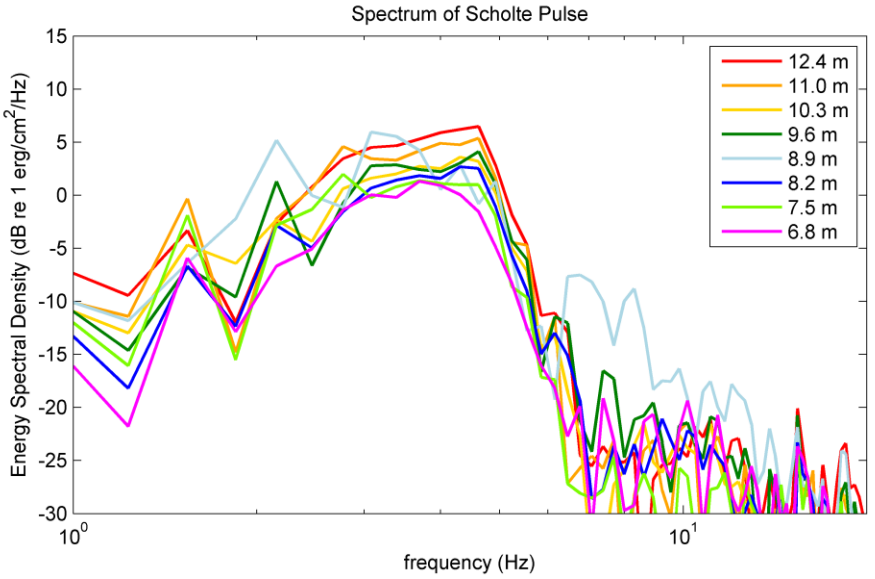

Figure 4.3. Energy spectral density of the Scholte wave from the 3 kg NEW charge recorded at 430 m range on the VLA. Data from hydrophone 2 (11.7 m) has not been included due to signal noise.

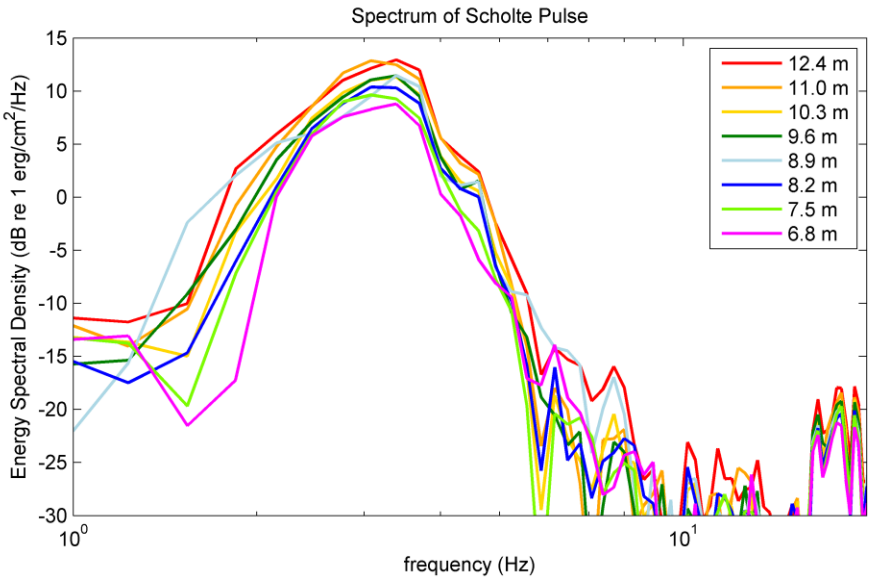

Figure 4.4. Energy spectral density of the Scholte wave from the 6 kg NEW charge recorded at 430 m range on the VLA. Data from hydrophone 2 (11.7 m) has not been included due to signal noise.

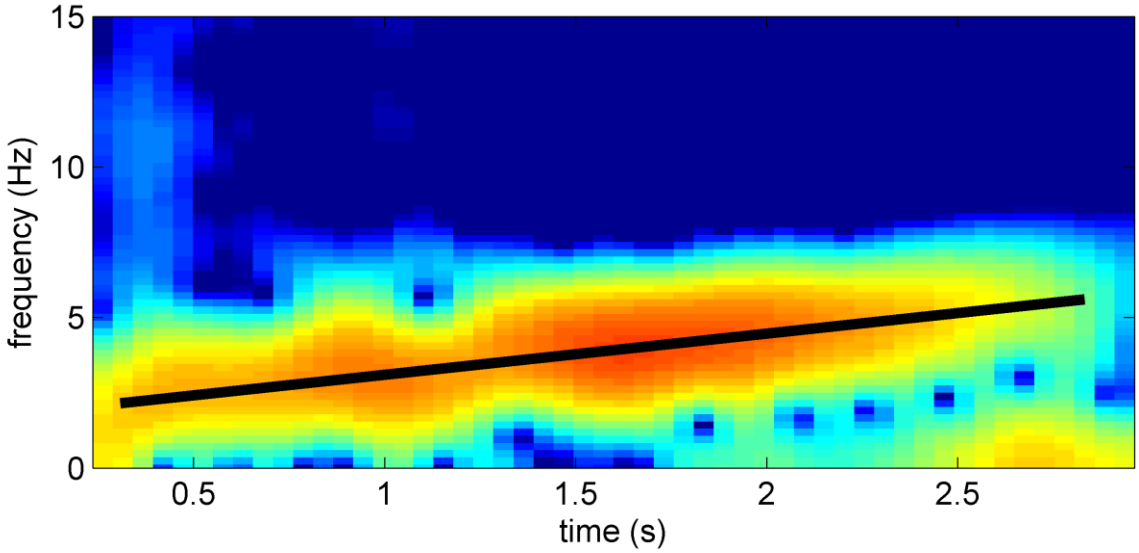

Figure 4.5. Spectrogram of the Scholte wave from the 3 kg NEW charge measured at the 430 m range on hydrophone 1 of the VLA (12.4 m depth). The black line indicates the dispersion trend.

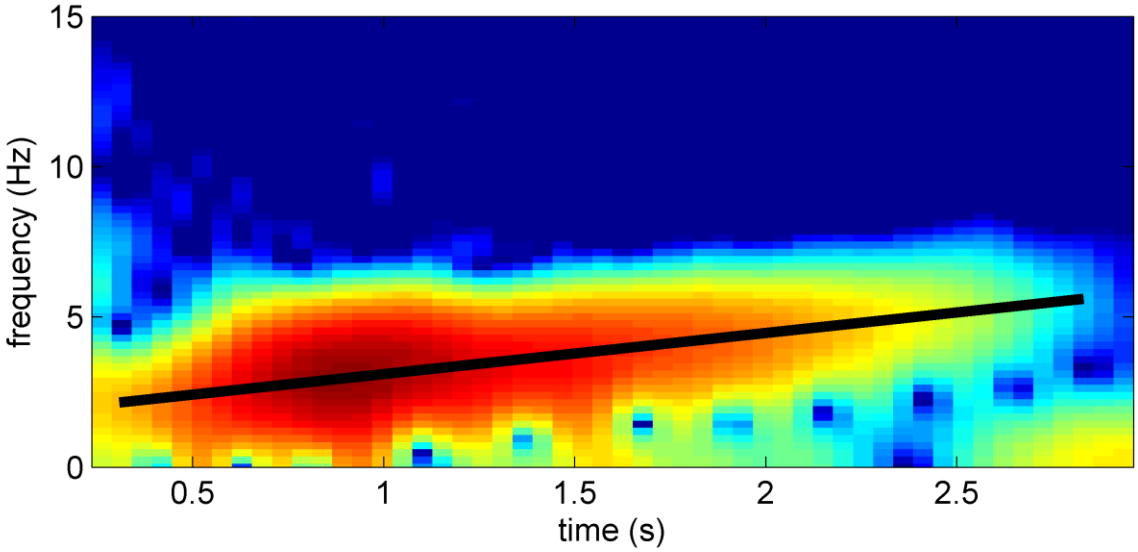

Figure 4.6. Spectrogram of the Scholte wave from the 6 kg NEW charge measured at the 430 m range on hydrophone 1 of the VLA (12.4 m depth). The black line indicates the dispersion trend.

4.4.2 *Best Fit Model*

Through iterative forward modeling, we have found the best fit model for the 3 kg-TNT equivalent charge is;

$$c_s(z) = (102 \pm 7)\, z^{(0.375 \pm 0.008)} \tag{4.28}$$

and for the 6 kg-TNT equivalent charge;

$$c_s(z) = (102 \pm 7)\, z^{(0.367 \pm 0.007)} \tag{4.29}$$

The resulting time series of these model results are compared to the band-passed filtered data (Figure 4.7), with reasonable agreement in both magnitude and phase evident.

In this study we have assumed that the main contribution to the error is from uncertainty in the source-receiver range, so our error bounds are given by the best fit model parameters at ±50 m from the measurement range of 430 m (Figure 4.8). In the future, a more robust approach that includes measurement range as a model parameter may be employed. For the purpose of this dissertation, however, we feel that the method used is sufficient for demonstrating that the explosion-generated Scholte waves traveling in the sandy seabed at the measurement site can be modeled using a power law dependent shear wave speed profile with c_{ob} and β in Eq. (2.19) being site dependent.

As an additional check on our results, the group velocity curves for the modeled and measured data (Figure 4.9) have also been computed following the method of Ohta et al. [86]. The basic dispersion properties seen in the data are captured by the model results, although the comparison is limited to frequencies less than 4.5 Hz owing to low signal levels at higher frequencies. The dispersion effects observed can be explained qualitatively by remembering that Scholte waves decay within one wavelength of the water sediment interface. As lower frequencies have longer wavelengths, they penetrate to greater depths in the seabed. With the shear wave speed in the seabed increasing with depth, the low frequencies penetrate to depths with higher speeds. As a result, the low frequencies arrive first followed by higher frequencies. This leads to the dispersion trends in the data shown in Figure 4.5 and Figure 4.6.

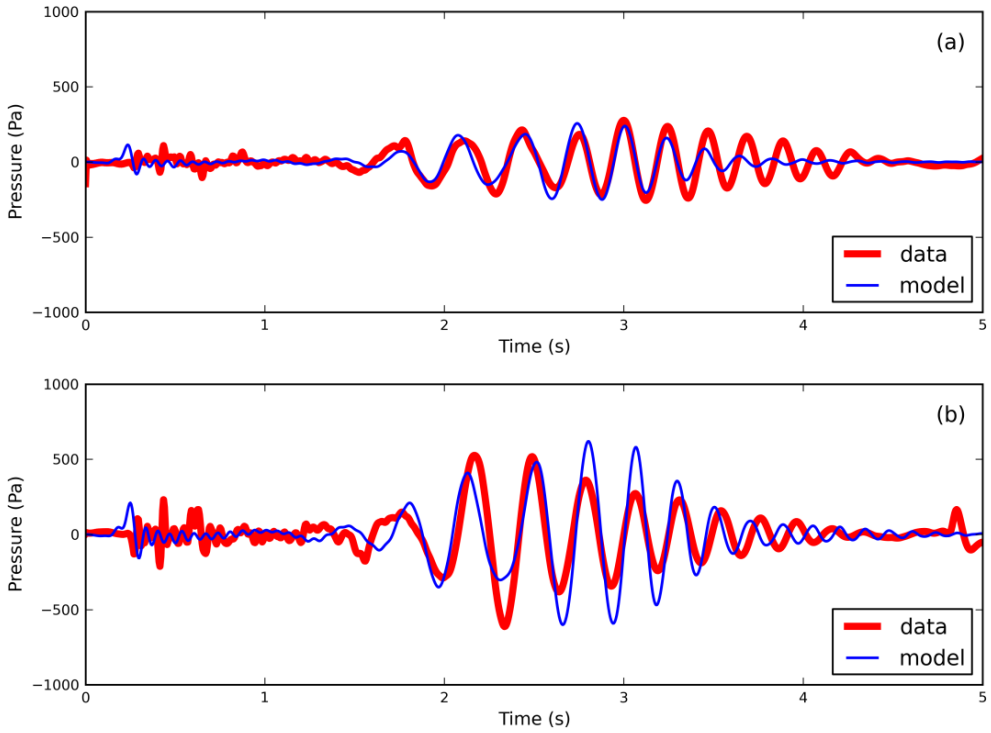

Figure 4.7 Measured data from hydrophone 1 of the VLA measured at 12.4 m depth (thick line) compared to (a) the best fit model (thin line) for the 3 kg NEW charge given by Eq. (4.28), and (b) the best fit model for the 6 kg NEW charge given by Eq. (4.29). The region starting at 0.28 s represents the main waterborne arrival, the level for which is highly reduced above 15 Hz being examined here.

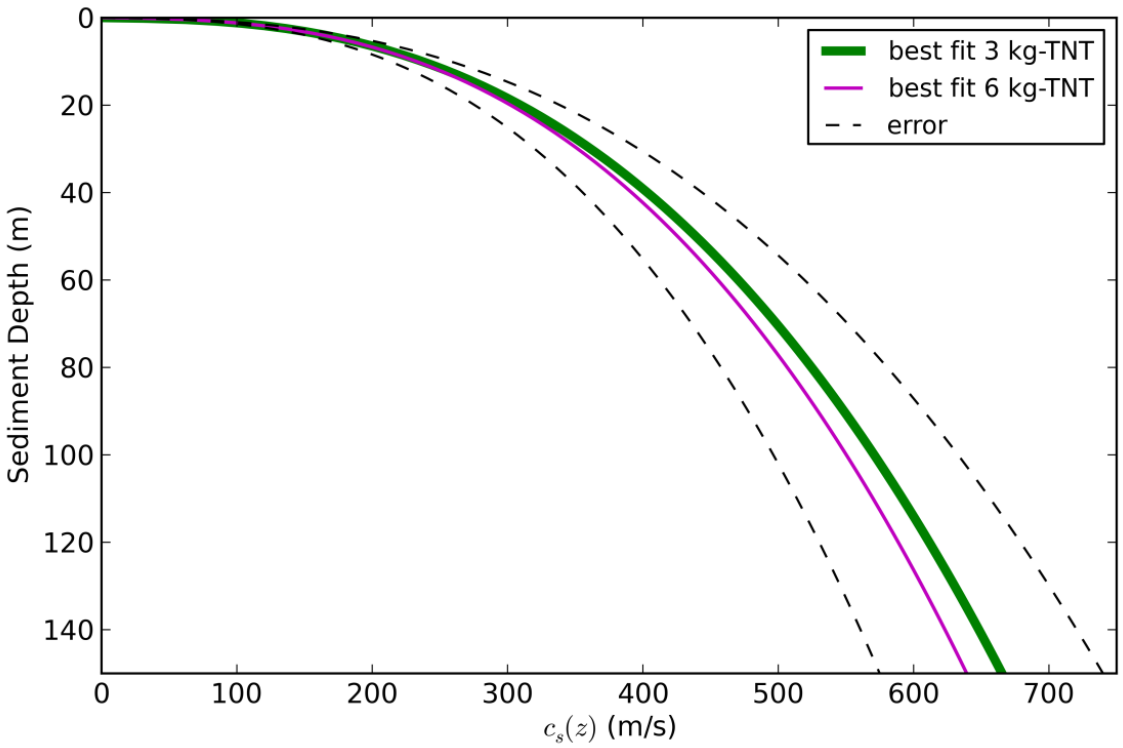

Figure 4.8. Best fit shear wave speed profile for the 3 kg NEW charge given by Eq. (4.28) (thin solid line) and the 6 kg NEW given by Eq. (4.29) (thick solid line) at 430 m range. The error bounds (dashed lines) shown in the figure represent the overall minimum and maximum profiles for the two charges. The lower error bound is given by the best fit profile for the 6 kg NEW equivalent charge at 380 m, and the upper error bound is given by the best fit profile for the 3 kg NEW equivalent charge at 480 m.

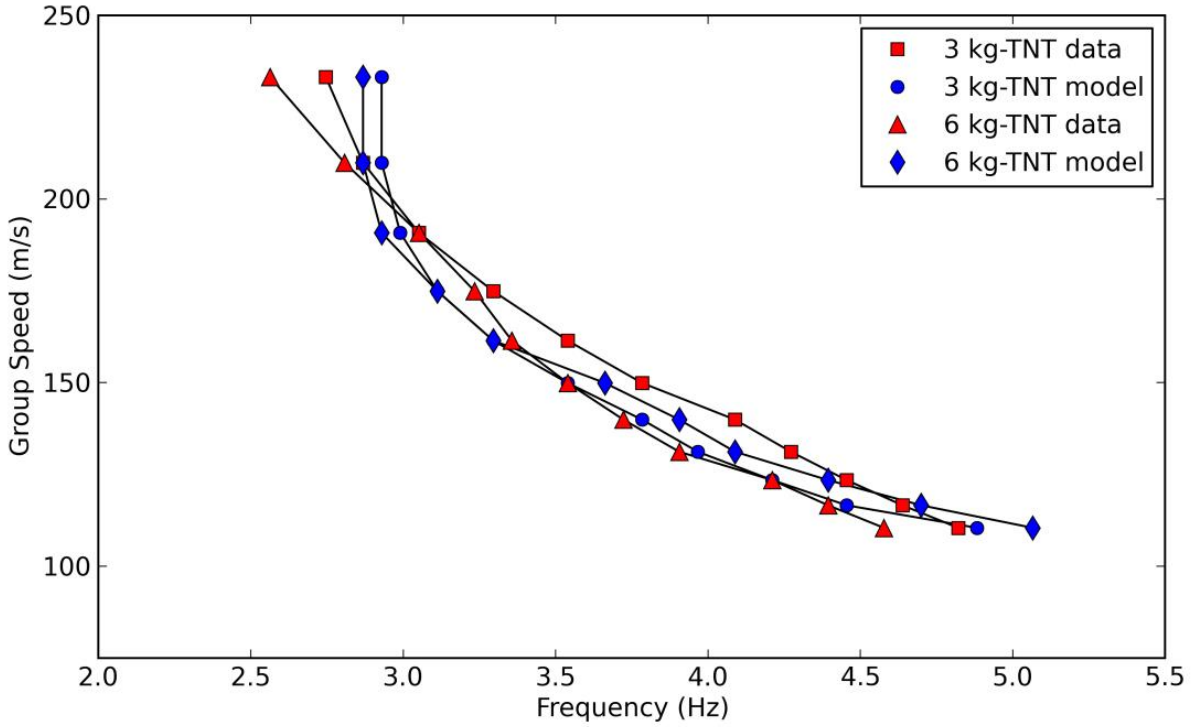

Figure 4.9. Comparison of the group speeds for the measured data (red squares, red triangles) and the best fit model results (blue circles, blue diamonds) for the 3 kg NEW equivalent and the 6 kg NEW equivalent charges.

4.5 SUMMARY AND CONCLUSIONS

In this chapter we have used a forward modeling approach and an empirical source model from Chapman [16], [17] to show that the explosion-generated Scholte waves traveling in the sandy seabed at the measurement site can be modeled using a power law dependent shear wave speed profile described by Eq. (2.19). As discussed by Rauch [43], the dispersion characteristics of Scholte waves in sand cannot be reproduced using a homogeneous half-space seabed (e.g. Pekeris waveguide model with elastic seabed) but instead requires a depth-dependent shear wave speed. The model results for the best fit shear wave speed profile, determined through waveform matching, are in good agreement with both the measured data as well as previous studies that put ν in the range of 0.3 to 0.4 [47], [50].

This chapter demonstrates the approach that is used throughout this dissertation where observations from the data are used to develop proposed geoacoustic seabed model for a given measurement site. These models are then tested against the data with the help of numerical propagation models. Throughout the remainder of this work, numerical predictions are computed with the OASES wavenumber integration model.

Chapter 5. EXPERIMENT COMPARISON FOR THREE SHALLOW WATER SITES

5.1 INTRODUCTION

In this Chapter measurements of underwater explosions from Pu`uloa are presented and compared to data collected at Virginia Beach and at Silver Strand Training Complex. The goal of this work is to show that the peak pressure and SEL from the Pu`uloa experiment are significantly lower than those from the other two experiments as a result of high propagation losses resulting from the composition of the Pu`uloa seabed.

All three of these experiments were conducted in shallow water (depth <25m) where sound propagation is heavily affected by interaction with the seabed. At the Pu`uloa measurement site, the seabed is primarily composed of limestone topped by a layer of coral sand of varying thickness (on the order of 1 m), whereas the other two sites are composed primarily of terrigenous sands and clays. Previous studies have shown that high propagation losses can occur in areas where a hard-rock seabed is topped by thin sediment layers [61], [62], with Duncan et. al. [87] identifying these effects in a seabed similar to the Pu`uloa site. The data from the Pu`uloa site provide an opportunity to explore these effects in greater detail and investigate the impact that this type of seabed has on the metrics commonly used in assessing environmental noise, the peak pressure and sound exposure level (SEL) [88].

In Section 5.2, the peak pressure, SEL, and energy spectral density (ESD) from the experiments are compared that show the Pu`uloa metrics are significantly lower than the other two sites (which are in good agreement with each other). The mechanisms responsible for these lower levels are explored In Section 5.3 the receiver-to-receiver path loss for these data are compared to numerical and analytical models to investigate the impact of the seabed on propagation independent of the source. Other mechanisms that could cause high losses at the Pu`uloa site are also considered, including sea surface roughness and bathymetric refraction. Conclusions for this work are presented in Section 5.4.

5.2 EXPERIMENT RESULTS

In this section the peak pressure and SEL from the Pu`uloa experiment are compared to explosion measurements collected at the Virginia Beach training facility and the Silver Strand training complex for all charge and range combinations. We also present the energy spectral density (ESD) for receivers positioned between 350 and 700 m and charges from 3.0 kg NEW to 6.0 kg NEW.

5.2.1 *Peak Pressure and Sound Exposure Level (SEL)*

The peak pressure and SEL for the experiments are shown in Figure 5.1 and Figure 5.2 respectively. The peak pressure is shown with respect to scaled range from Eq. (2.24) and the SEL is shown with respect to the scaling parameter in Eq. (2.27). For both metrics, the Pu`uloa data is always lower than both the Virginia Beach and Silver Strand data with the peak pressure 10 to 30 dB lower and the SEL being 15 to 30 dB lower. The differences in the peak pressure are particularly notable since the Virginia Beach data and Silver Strand data are in good agreement with Arons' empirical equation for peak pressure in Eq. (2.24). Comparing the measured peak pressures to Eq. (2.24) in Figure 5.1 we see that the Pu`uloa data do not agree with the empirical predictions. Although the peak pressure equation was formulated for an unbounded media, it does appear to give reasonable predictions for propagation at the Virginia Beach and Silver Strand sites. For these sites, the peak pressures at the lower bound of scaled range are below the empirical prediction, whereas the upper bounds of the scaled range shows measured peak pressure above the empirical predictions. Based on this observation, it is unclear whether Eq. (2.24) accurately predicts the peak pressure for range and weight combinations outside of those explored in this work.

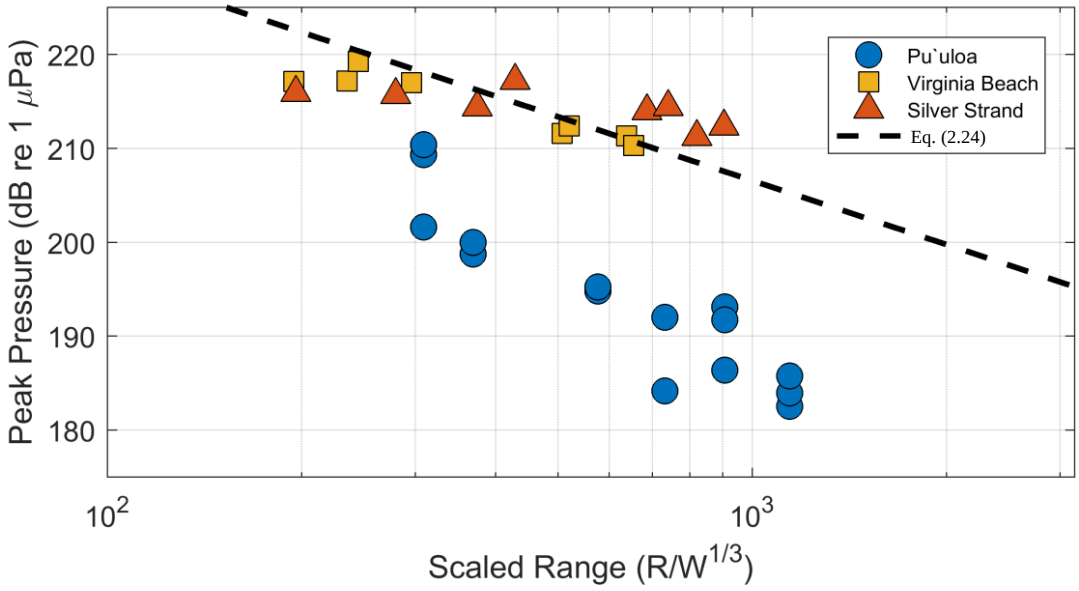

Figure 5.1. Peak pressures from the Pu`uloa and Virginia Beach measurements plotted against scaled range which is a function of the charge weight, W, in kg NEW and the measurement range, R, in meters. These data are also compared to the empirical equation for peak pressure given in Eq. (2.24) For a given scaled range, the Pu`uloa peak pressures are up to 25 dB lower than the Virginia Beach and Silver Strand measurements and empirical predictions.

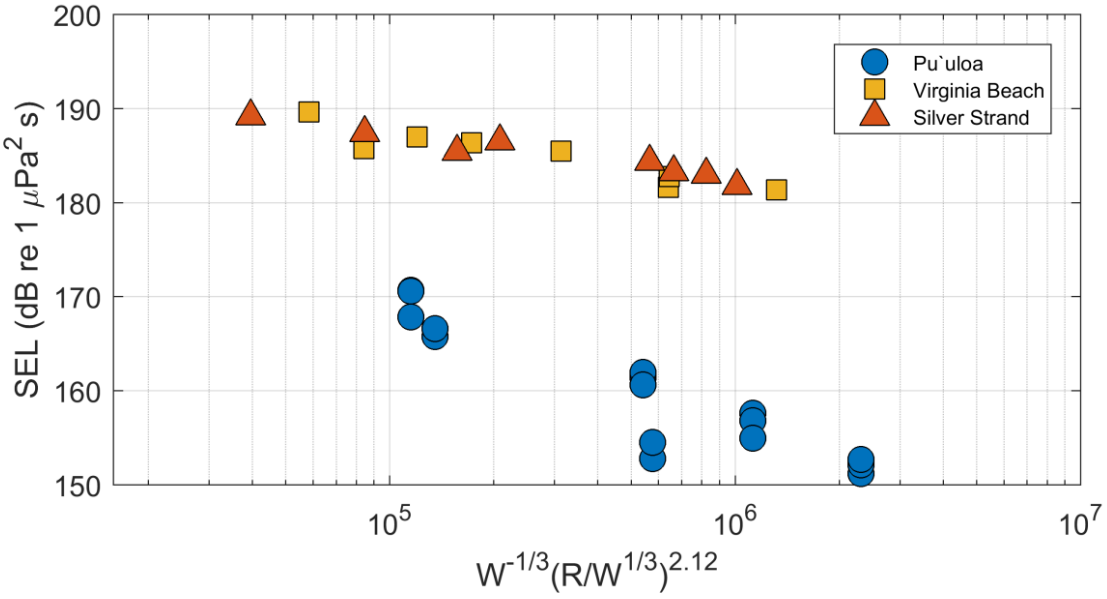

Figure 5.2. Sound Exposure Levels from the Pu`uloa and Virginia Beach measurements plotted against the scaling parameter in Eq. (2.27) which is a function of the charge weight, W, in kg NEW and the measurement range, R, in meters. The SEL for calculated from the Pu`uloa measurements are up to 25 dB lower than values calculated from the Virginia Beach and Silver Strand data.

5.2.2 *Energy Spectral Density*

In Figure 5.3 ESD from the three experiments are presented. Unfortunately, there is not a common combination of range and charge weight between the three experiments that allows for a direct comparison. Instead, the ESD for a range of charge weights and receiver ranges are presented and compared to the ESD from the Pu`uloa experiment of the 4.5 kg NEW charge measured at 512 m.

For the Virginia Beach ESD, two charge weights (3.0 kg NEW and 6.0 kg NEW) recorded at 430 m are presented and for the Silver Strand ESD two 6.0 kg NEW charges recorded at two measurement ranges are presented (358 m and 685 m). These data shows the Pu`uloa ESD is significantly lower than the ESD from the other two experiments with poor agreement from 50 Hz to the 4000 Hz third-octave bands. These differences are highest between the 50 and 1600 Hz

third-octave bands where the differences are as high as 30 dB. The high losses in the Pu`uloa data are also present in the VLA data which were collected along a separate transect.

Additionally, we can show that for similar charge weights and measurement ranges, the 6.0 kg NEW charges from Virginia Beach and Silver strand are consistent for frequencies above 80 Hz with differences typically less than 5 dB. The Silver Strand ESD also show that differences in the receiver range result in differences of less than 5 dB at frequencies between 50 and 1600 Hz. These results show that the differences in the ESD between the Pu`uloa data and the other two experiments is not due to differences in charge weight or measurement range, but is likely due to some other effect. In the following section these results are discussed along with the possible mechanisms that could be responsible for the high losses in the Pu`uloa data.

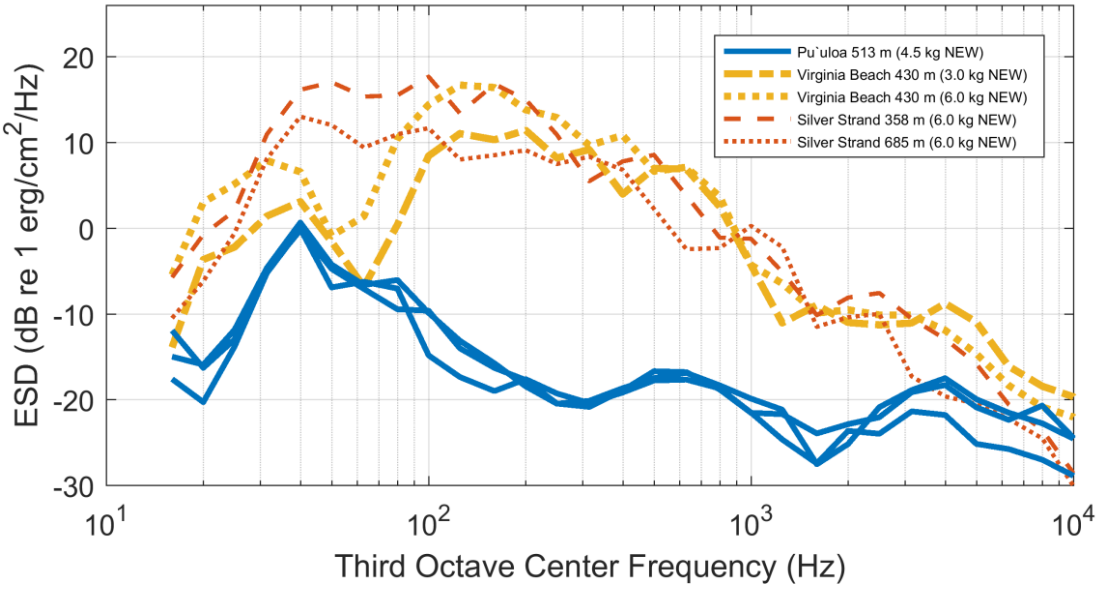

Figure 5.3. Energy spectral density for the 4.5 kg NEW charges from the Pu`uloa experiment measured at 513 m, the 3.0 kg NEW and 6.0 kg NEW charges from the Virginia Beach experiment measured at 430 m, and the 6.0 kg NEW charge measured at the Silver Strand experiment at 358 m and 685 m. While the Virginia Beach and Silver Strand ESD typically differ by less than 5 dB above 80 Hz, the Pu`uloa are up to 30 dB lower for third-octave bands between 80 Hz and 1600 Hz.

5.2.3 *Time-Frequency Analysis*

Time-frequency analysis is a useful tool for examining how the spectral content of the data changes with time. In this section this is accomplished using a 1024 Hamming window for each time bin and 90% overlap for successive time bins. Spectrograms of the Virginia Beach (Figure 5.4, Figure 5.5, Figure 5.6, and Figure 5.7) and the San Diego data (Figure 5.8 and Figure 5.9) show similar characteristics with both the main arrival and bubble pulse arrival visible. These data show considerable energy between 50 Hz and 1600 Hz. This is distinct from the Pu`uloa data (Figure 5.10 and Figure 5.11) where energy at these frequencies is considerably lower for the 750 m range and almost entirely absent at the 1500 m range. This is consistent with the ESD for these data (Figure 5.3) in which the Pu`uloa measurements exhibit lower levels than data collected at the other two measurement sites. Additionally, the Pu`uloa data collected at 1500 m shows energy levels between 50 Hz and 500 to be close to the ambient levels.

The Silver Strand Data exhibits interesting characteristics with clear modal dispersion features visible in the main water arrival for the 1650 m range (Figure 5.9) at 0.0 s and in the bubble pulse arrival at approximately 0.2 s. This is not visible for the data collected during the same test at 685 m (Figure 5.8). As the Virginia Beach data was collected at a closer range, these dispersion effects are not distinct.

In addition to the hole in the Pu`uloa spectrograms between 50 Hz and 1600 Hz, another interesting feature is observed coming in 0.1 s after the main water arrival. The time offset is too low to be the bubble pulse (arriving at 0.3 s) and does not appear to change between the 750 m and 1500 m range which indicates that it is likely a source effect instead of a propagation effect. One explanation for this feature comes from the work of Cui et. al. [68]; when a source is close to the surface cavitation can occur and a distinct signal of the cavitation region collapse can be observed. This is only clearly observed in the Pu`uloa data and is possibly due to the shallower depth at the detonation location (10 m) compared to the Virginia Beach and Silver Strand sites (16 m and 22 m for respectively). An alternate explanation, also based on the work by Cui et. al, relates to cavitation resulting from detonation of a source above a solid surface. A detailed study of these effects is outside the scope of this work, but does provide motivation for comparing the

measurement from the three experiments independent of the source as site-to-site variation in the source waveform is clearly a possibility.

Further support for this assertion is given by Figure 5.6 and Figure 5.7 for the 0.3 kg NEW charge detonated at mid-water where two bubble pulses are observed as opposed to a single bubble pulse in Figure 5.4 and Figure 5.5 for the 6.0 kg NEW charge detonated on the seabed. The midwater detonation, unlike the bottom detonation, allows for the continued pulsation of the gas sphere. A similar trend is also observed for the 3 kg NEW charge detonated at midwater depth, whereas all bottom detonation measured in these experiments (Silver Strand and Pu`uloa data included) show only a single bubble pulse. This lends further support to analyzing these data independent of the source term.

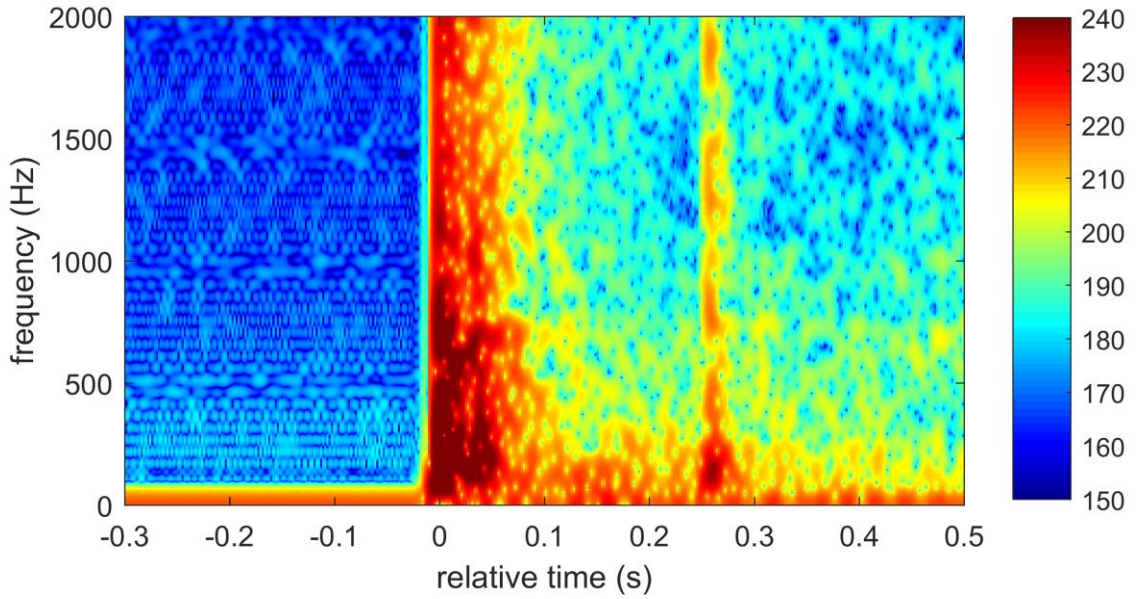

Figure 5.4. Spectrogram from the Virginia experiment for the 6.0 kg charge measured at 430 m range. Color bar in dB re 1 $\mu Pa^2\ s$.

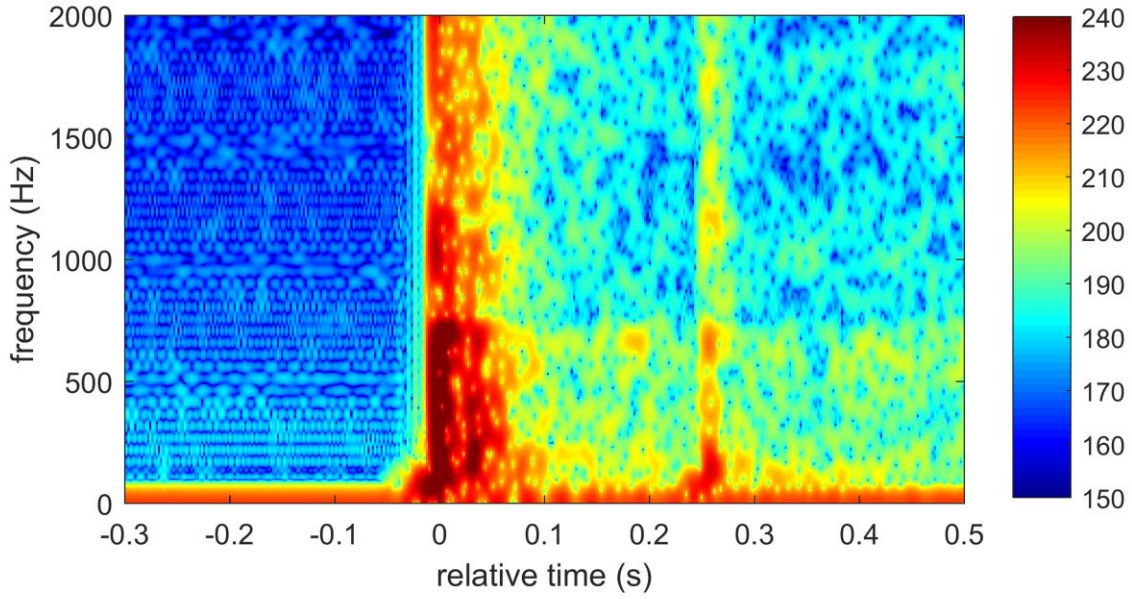

Figure 5.5. Spectrogram from the Virginia experiment for the 6.0 kg charge measured at 950 m range. Color bar in dB re 1 $\mu Pa^2\ s$.

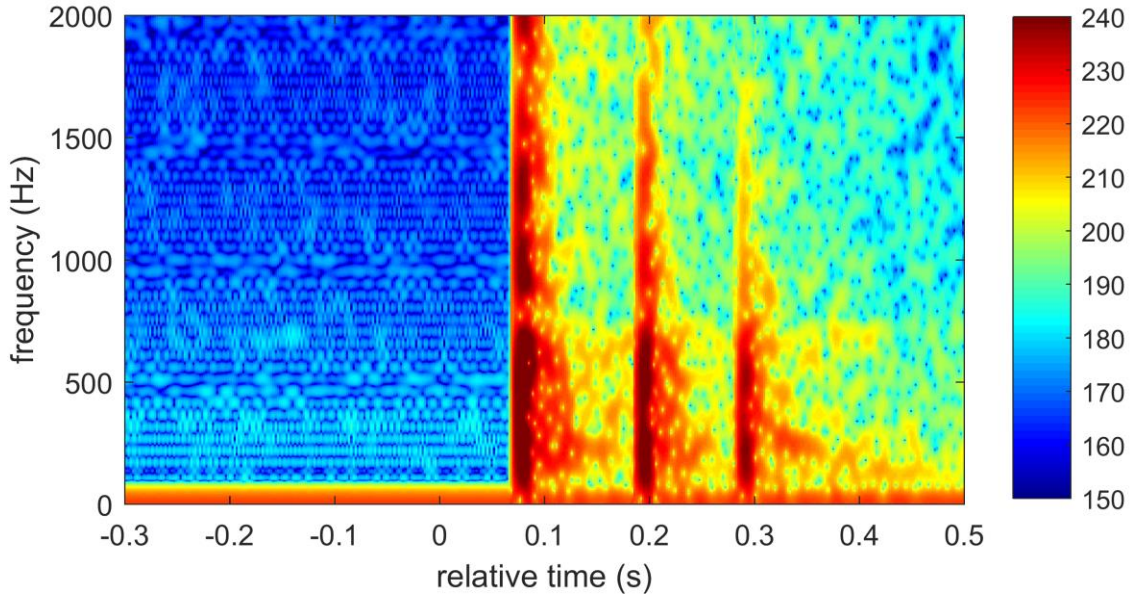

Figure 5.6. Spectrogram from the Virginia experiment for the 0.3 kg charge measured at 165 m range. Color bar in dB re 1 $\mu Pa^2\ s$.

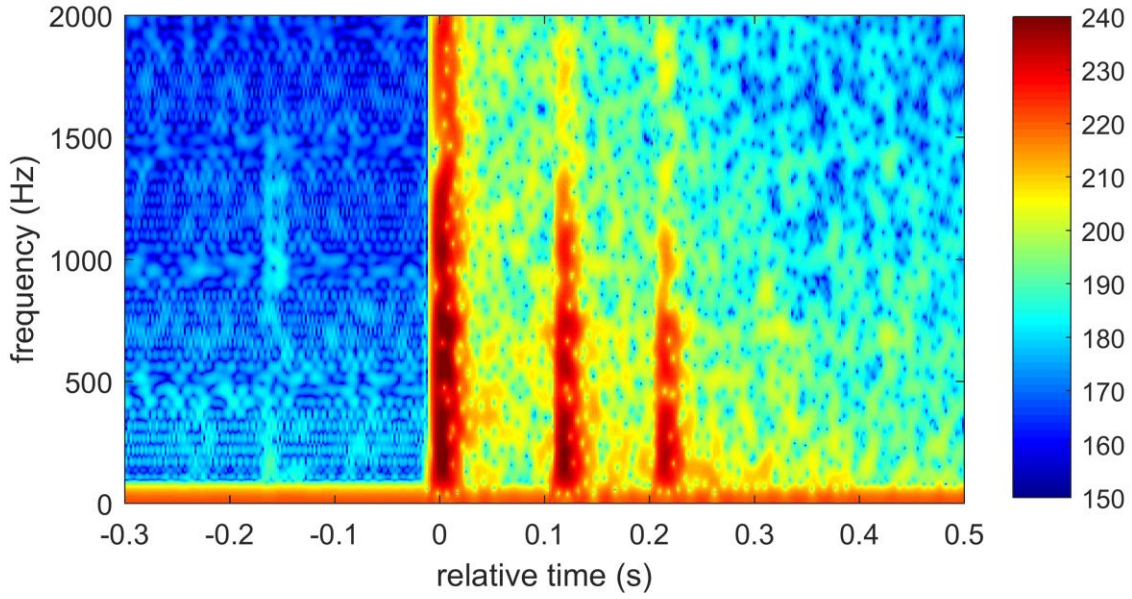

Figure 5.7. Spectrogram from the Virginia experiment for the 0.3 kg charge measured at 430 m range. Color bar in dB re 1 $\mu Pa^2\ s$.

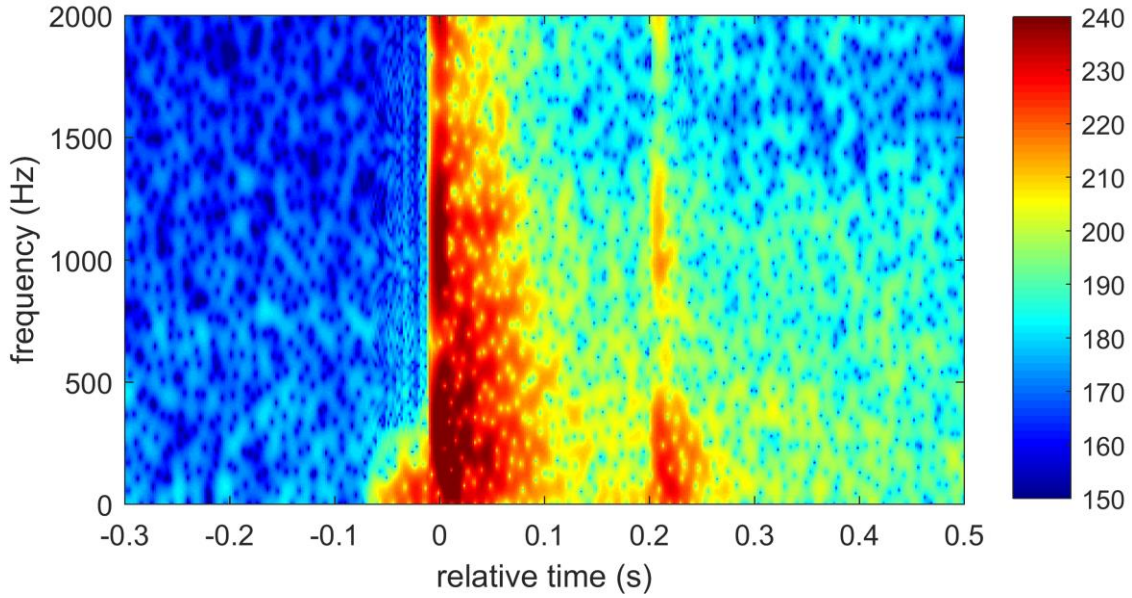

Figure 5.8. Spectrogram from the San Diego experiment for a 6.0 kg charge measured at 685 m range. Color bar in dB re 1 $\mu Pa^2\ s$.

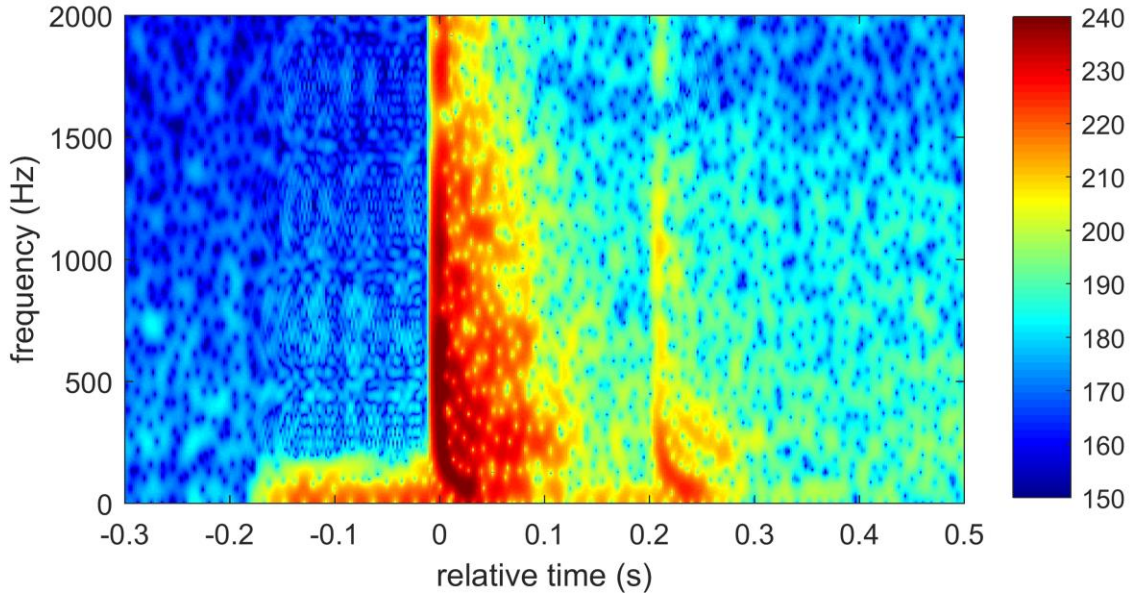

Figure 5.9. Spectrogram from the San Diego experiment for a 6.0 kg charge measured at 1650 m range. Color bar in dB re 1 $\mu Pa^2\ s$.

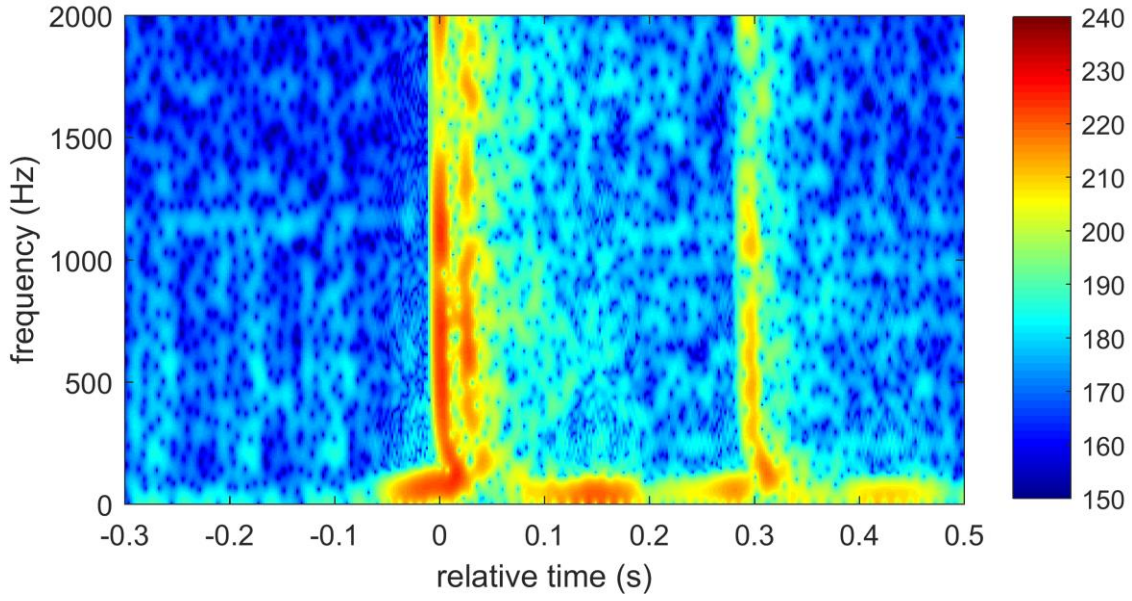

Figure 5.10. Spectrogram from the Pu`uloa experiment for a 4.5 kg charge measured at 750 m range. Color bar in dB re 1 $\mu Pa^2\ s$.

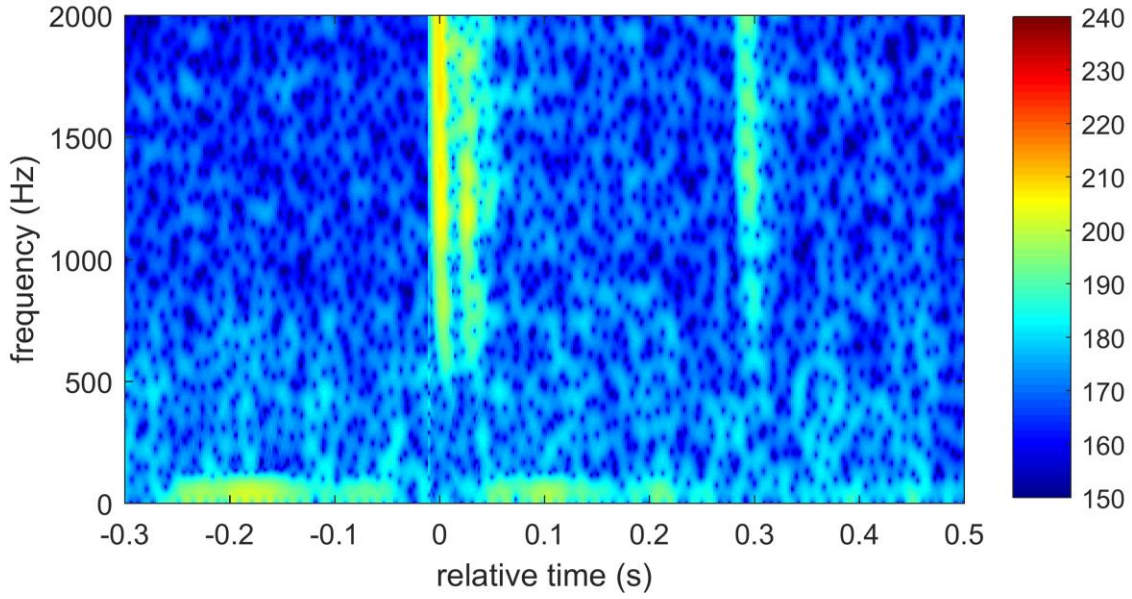

Figure 5.11. Spectrogram from the Pu`uloa experiment for a 4.5 kg charge measured at 1500 m range. Color bar in dB re 1 $\mu Pa^2\ s$.

5.3 DISCUSSION AND MODELLING

In the following section we explore the mechanisms that could cause the peak pressure, SEL, and ESD for the Pu`uloa measurements to be lower than those from the other two experiments. We show that while effects from sea-surface roughness, bathymetric refraction, or effects of the shallow water detonation on the source (e.g., cavitation) could be responsible, the high losses are likely caused by high seabed reflection loss (RL) due to the seabed composition.

In this analysis seabed effects are explored using both numerical propagation models and an analytical RL model. First, a geoacoustic model for each measurement site is presented. Then, using these geoacoustic models, the receiver-to-receiver path loss at each experiment site are computed and compared to predictions from the OASES wavenumber integration model[29]. This allows the effects of the measurement environment, independent of the source, to be explored. An analytical RL model from Chapman and Chapman [63] is then be used to verify the OASES results for the Pu`uloa site and explore the role of shear effects in the RL. The measured and modeled Pu`uloa results are also considered in the context of the equipment self-noise.

Finally we discuss possible losses from sea-surface roughness and bathymetric refraction and show that any resulting attenuation is small when compared to the losses attributed to the seabed.

5.3.1 *Geoacoustic Model*

5.3.1.1 Pu`uloa

The exact composition of the seabed at the Pu`uloa site is unknown, however previous seabed studies [77], [78] and discussions with the Navy divers indicates that it is likely composed of a limestone basement which in some areas is topped by a thin sand layer of varying thickness. For the purposes of this study it is represented as a two layer medium with a thin sand layer overlying a limestone half-space.

Fu et al. [78], in their study of coral sands close to the measurement site, discuss the loose and poorly compacted nature of the sediment resulting from regular wave activity. That study put the compressional wave speed of coral sands between 1600 and 1650 m/s. In this work a compressional wave speed of 1600 m/s is used. The study did not provide a shear wave speed and, in general, studies have not been conducted where the shear wave speed in thin sand layers has been measured. A shear wave speed of 150 m/s has therefore been assumed. Due to poor consolidation resulting from wave and water action, this value could be high for sand in a thin layer. Comparing this value to Eq. (4.28) and Eq. (4.29), however, demonstrates that this assumption is not unreasonable for sand at depths on the order of 1 m where the shear wave speed of sand would be between 0 m/s at the water-sediment interface and 228 m/s at 9 m depths. This estimate is sufficient, however, for the purposes of this study. Fu et al. also presented measurements of the compressional attenuation between 0.5 and 1.4 dB/λ, however this value is much higher than typical literature values. Instead we use a more conservative compressional attenuation of 0.2 dB/λ and a shear attenuation of 1.0 dB/λ. Finally, a density of 2000 kg/m^3 is also used.

For the limestone half-space, the compressional wave speed was estimated by using the precursor arrivals measured on the high sensitivity systems at 1500 m for all test charges. The time series for the precursor arrivals for all nine time series are shown in Figure 5.12 through

Figure 5.20. The time signature before the main water arrival (at 0 s) was measured on the high sensitivity hydrophone and the remainder of the signal was measured on the low sensitivity hydrophone. Time is shown relative to the main water arrival at 0s.

Precursor arrivals are observed on the low sensitivity systems at all receiver ranges; however, comparisons of the data collected at the low and high sensitivity systems at 1500 m indicate that the low sensitivity system is not sensitive enough to measure the onset of the precursor arrival. Using that equipment would lead to underestimates of the compressional speed within the seabed so only data from the high sensitivity system were used. For all of the measurements, the high sensitivity system was saturated by the main water arrival due to the high amplitude. The onset of the main water arrival (corresponding to 0 s in Figure 5.12 through Figure 5.20) is assumed to correspond to the time where the system is saturated.

The arrival time difference between the main water arrival and the start of the precursor arrival for all nine tests gives a compressional wave speed in the range of 2105 m/s to 2231 m/s with an average compressional speed of 2150 m/s and a standard deviation of 51 m/s (Table 5.1). The single element systems were deployed and recovered each day so these errors could be due to spatial variations within the seabed caused by small changes in the receiver locations, or simply due to small differences in the source and receiver range. These values are, however, close to literature values for Limestone [89] so the average value of 2150 m/s is used in this work. Studies have shown the ratio of the compressional to shear wave speeds is 1.9 [89] which would give a shear wave speed in the limestone of 1075 m/s. Additional discussion on estimating the shear wave speed can be found in Appendix D. Relations from Hamilton [90] are also available that relate the density, ρ, to the compressional sound speed, c_p, in limestone;

$$\rho = 0.122\, c_p + 1979 \tag{5.30}$$

Using Eq. (5.30) puts the density in the limestone at 2192 kg/m^3. Finally, a compressional wave attenuation of 0.1 dB/λ and a shear wave attenuation of 0.2 dB/λ is assumed for the limestone half-space. These parameters are summarized in Table 5.2.

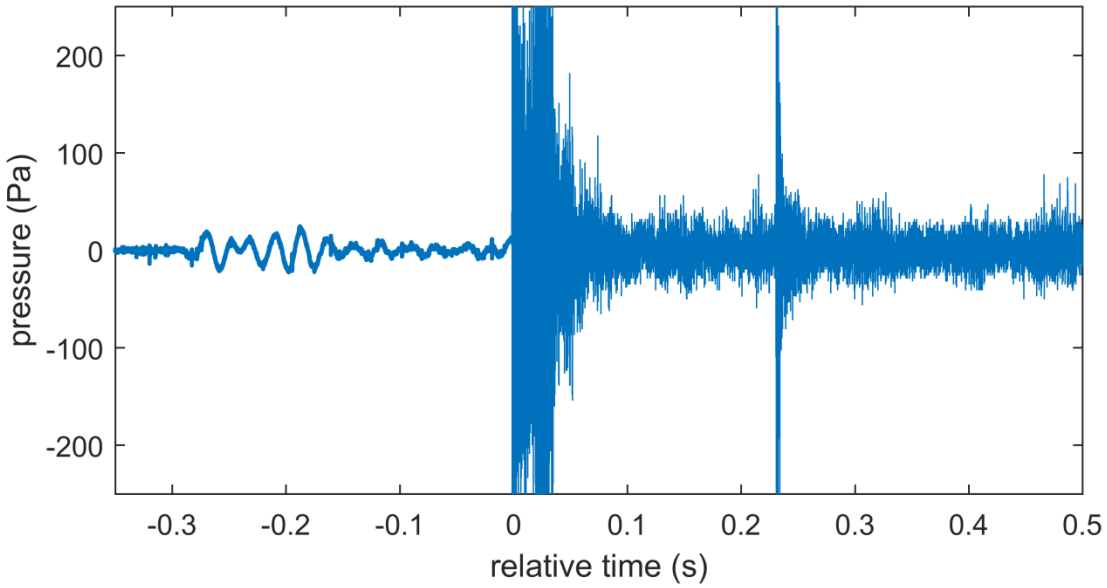

Figure 5.12. Precursor arrival from test 1 of the 2.3 kg NEW charges measured during the Pu`uloa experiment at 1500 m showing a detailed view of the precursor arrival.

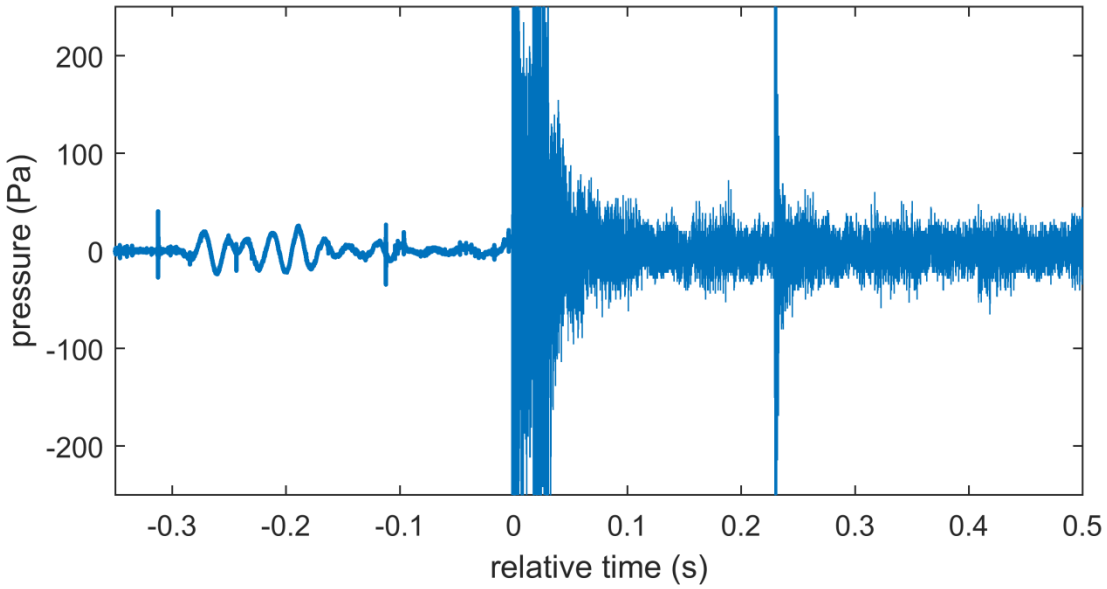

Figure 5.13. Precursor arrival from test 2 of the 2.3 kg NEW charges measured during the Pu`uloa experiment at 1500 m showing a detailed view of the precursor arrival.

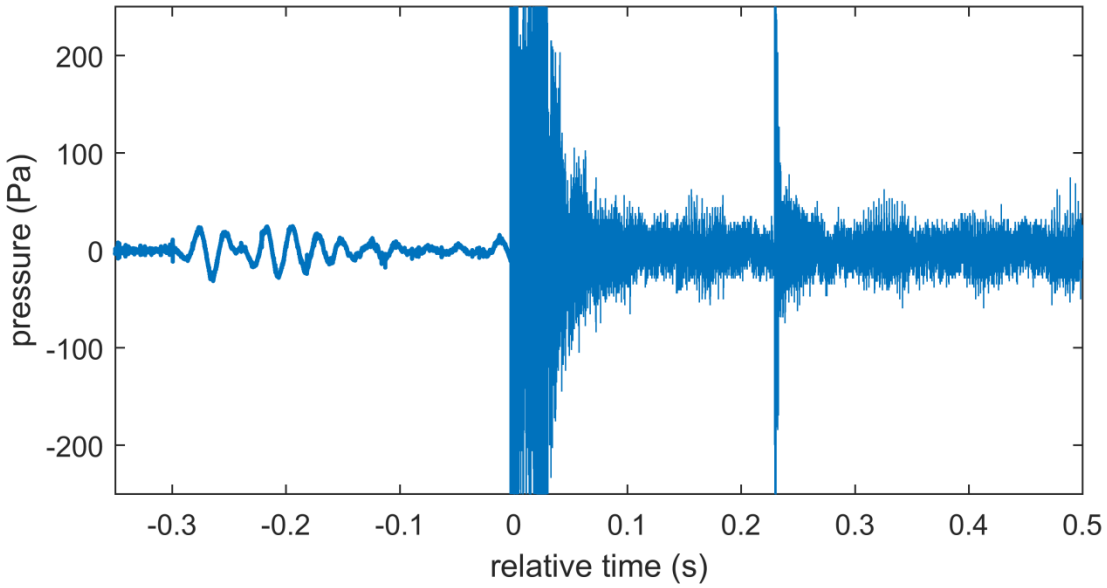

Figure 5.14. Precursor arrival from test 3 of the 2.3 kg NEW charges measured during the Pu`uloa experiment at 1500 m showing a detailed view of the precursor arrival.

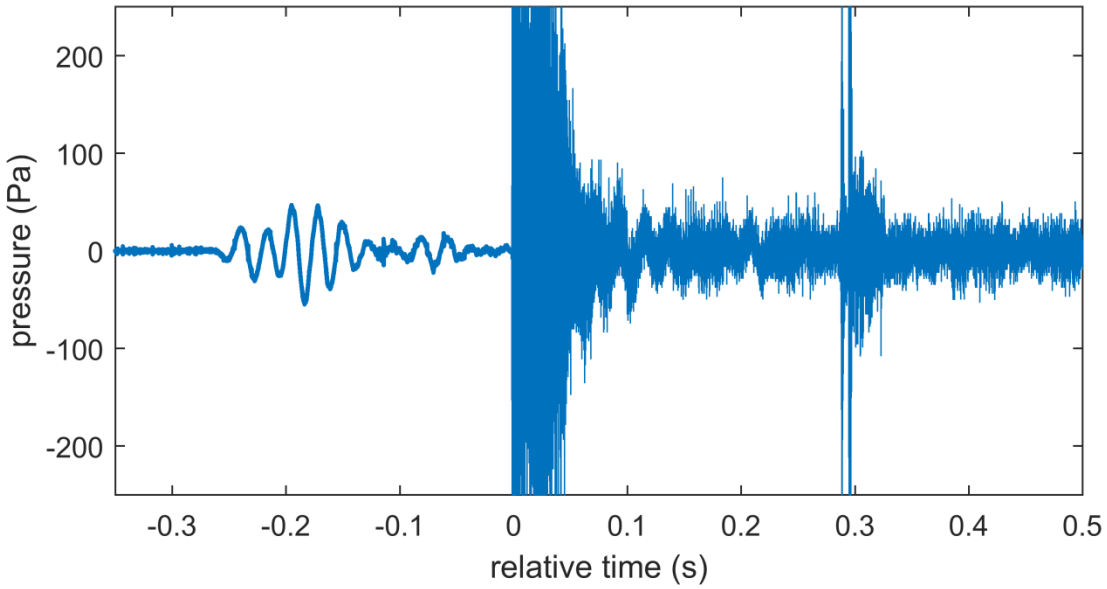

Figure 5.15. Precursor arrival from test 1 of the 4.5 kg NEW charges measured during the Pu`uloa experiment at 1500 m showing a detailed view of the precursor arrival.

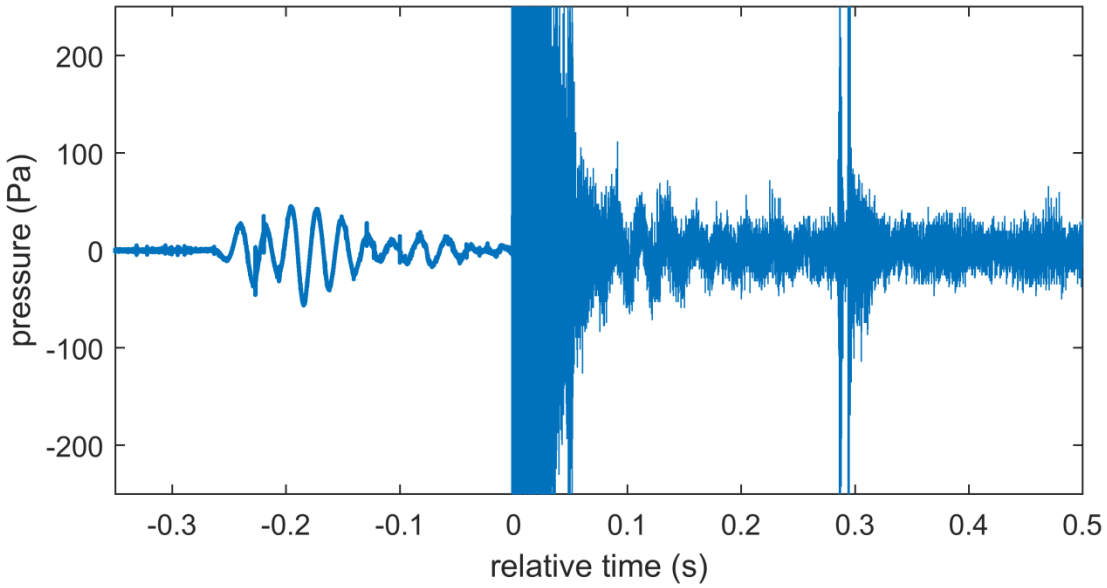

Figure 5.16. Precursor arrival from test 2 of the 4.5 kg NEW charges measured during the Pu`uloa experiment at 1500 m showing a detailed view of the precursor arrival.

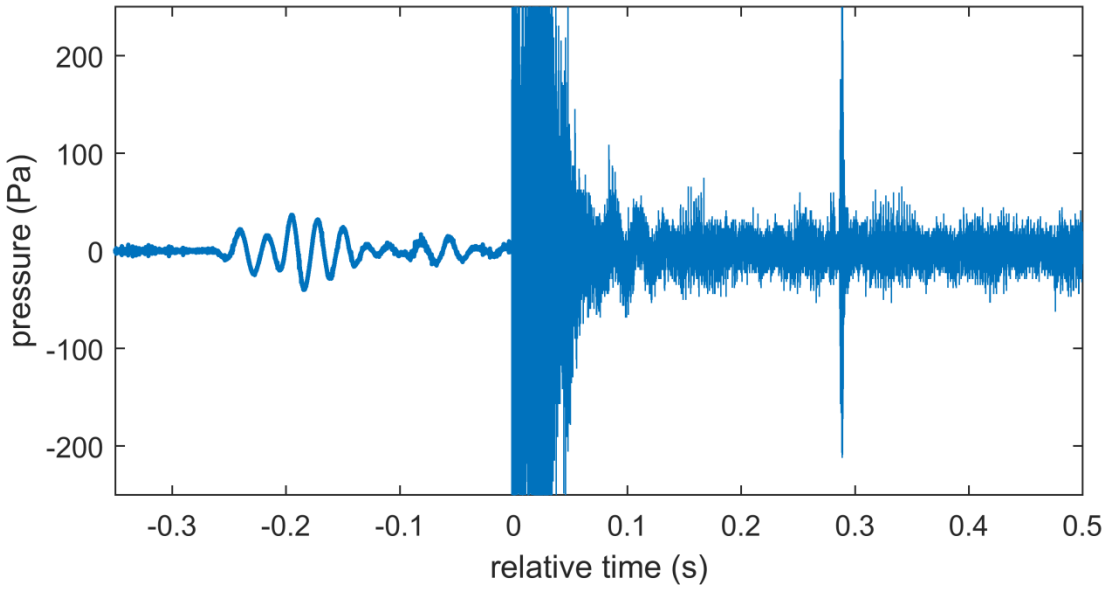

Figure 5.17. Precursor arrival from test 3 of the 4.5 kg NEW charges measured during the Pu`uloa experiment at 1500 m showing a detailed view of the precursor arrival.

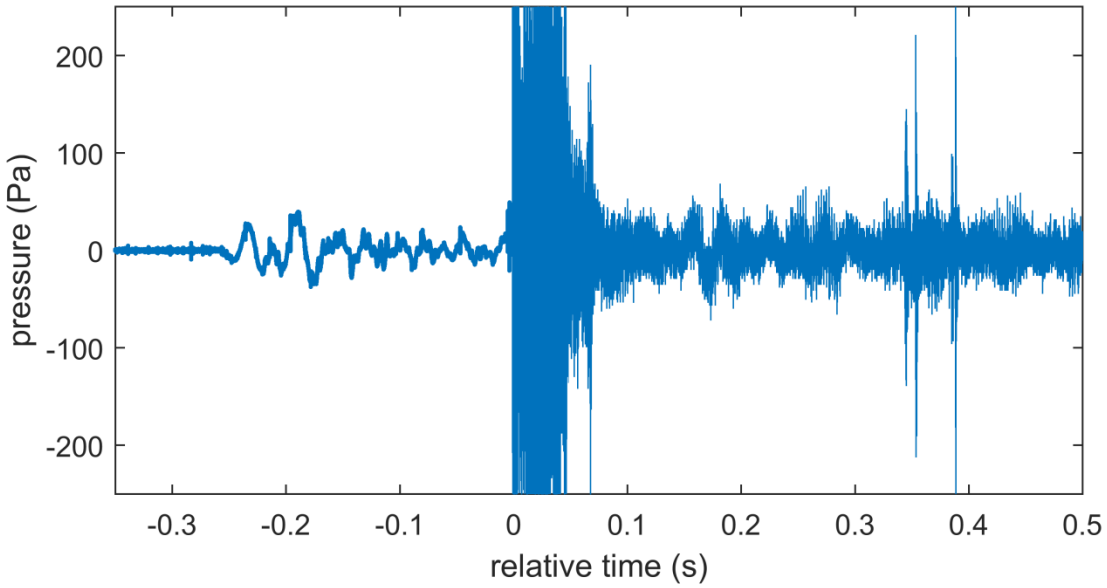

Figure 5.18. Precursor arrival from test 1 of the 8.0 kg NEW charges measured during the Pu`uloa experiment at 1500 m showing a detailed view of the precursor arrival.

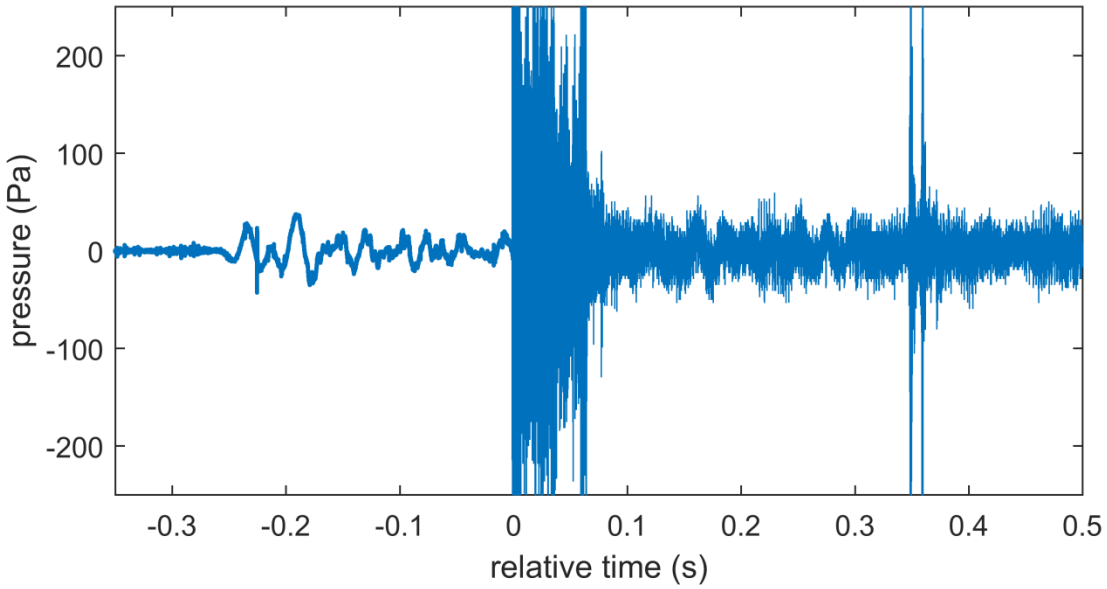

Figure 5.19. Precursor arrival from test 2 of the 8.0 kg NEW charges measured during the Pu`uloa experiment at 1500 m showing a detailed view of the precursor arrival.

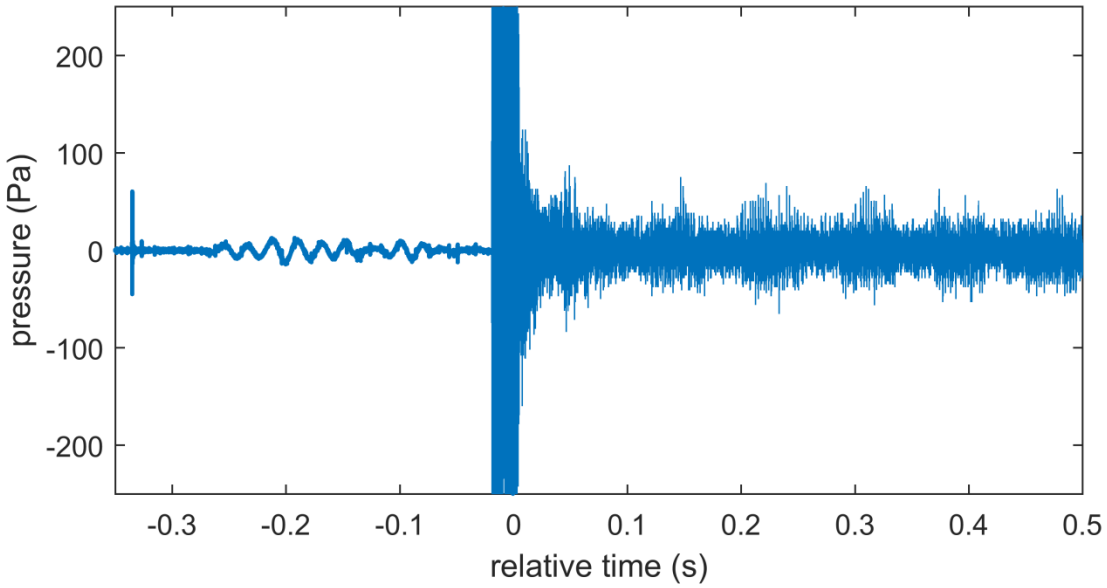

Figure 5.20. Precursor arrival from test 3 of the 8.0 kg NEW charges measured during the Pu`uloa experiment at 1500 m showing a detailed view of the precursor arrival.

Table 5.1. Summary of the Pu`uloa arrival times for the main water arrival and precursor arrivals used for calculating the compressional wave speed in the seabed. A water sound speed of 1537 m/s was used in the calculations.

weight (kg NEW)	**test**	**range (m)**	**water arrival (s)**	**precursor arrival time (s)**	**compressional Speed (m/s)**	**shear speed (m/s)**
2.3	1	1503	0.978	0.679	2214	1165
2.3	2	1503	0.978	0.678	2217	1167
2.3	3	1503	0.978	0.674	2231	1174
8	1	1503	0.978	0.711	2113	1112
8	2	1503	0.978	0.714	2105	1108
8	3	1503	0.978	0.697	2156	1135
4.5	1	1503	0.978	0.707	2125	1119
4.5	2	1503	0.978	0.708	2122	1117
4.5	3	1503	0.978	0.709	2121	1116
2.3	1	758	0.493	0.411	1845	971
2.3	2	758	0.493	0.413	1837	967
2.3	3	758	0.493	0.412	1840	969
8	1	784	0.510	0.434	1808	952
8	2	784	0.510	0.431	1820	958
8	3	784	0.510	0.417	1878	988
4.5	1	513	0.334	0.258	1990	1047
4.5	2	513	0.334	0.266	1931	1016
4.5	3	513	0.334	0.269	1904	1002

Table 5.2. Geoaoustic models for the three measurement sites. Below, *p* denotes the parameter associated with compressional waves and *s* detonates the parameters associated with the shear wave.

Measurement Site	Layer	Thickness (m)	Density (kg/m³)	Sound Speed (m)	attenuation (dB\λ)
Pu`uloa	water	10	1024	1537	-
	Sand	0.5	2000	p 1600 s 150	p 0.2 s 1.0
	Basement	∞	2192	p 2150 s 1075	p 0.1 s 0.2
Virginia Beach	Water	16	1024	1528	-
	Sand	∞	1900	p 1625 s Eq. (4.28)	p 0.2 s 1.0
Silver Strand	Water	22	1024	1493 - 1510	-
	Sand	∞	1900	p 1700 s Eq. (4.28)	p 0.2 s 1.0

5.3.1.2 Virginia Beach

For Virginia Beach, we use the geoacoustic model outlined in the paper by Soloway and Dahl [81] that uses a power-law dependent shear wave speed profile and a constant compressional wave speed. The previous study found the shear wave speed varied with depth into the sediment and was given by Eq. (2.19) with the best fit being $c_s(z) = 102\, z^{0.367}$. While this model assumes a density of 1700 kg/m^3 a more realistic value of 1900 kg/m^3 [57] is used. A sensitivity study has shown that the density does not have a considerable impact on the dispersion of Scholte waves, so this updated density is not expected to impact the results from the previous chapter. A compressional wave attenuation factor of 0.2 dB/λ and a shear attenuation factor of 1.0 dB/λ are also assumed.

The original study assumed a compressional sound speed in the sediment of 1700 m/s, however this study employs a similar approach used for the Pu`uloa data where the precursor arrival (Figure 5.21) is used to calculate the compressional wave speed in the seabed. Using measurements from the single element autonomous systems at all measurement ranges and assuming the peak pressure corresponds to the onset of the main water arrival gives a

compressional wave speed between 1590 m/s and 1657 m/s with an average value of 1625 m/s with a standard deviation of 21 m/s which is a reasonable value for sand (Table 5.3). In a previous paper by Soloway and Dahl 2014 [19] errors in the source-receiver range were estimated to be +/- 50 m. The lower end of this estimate puts the compressional wave speed in the seabed between 1109 m/s and 1570 m/s with an average value of 1388 m/s and a standard deviation of 175 m/s whereas the upper limit puts the wave speed in the range of 1735 m/s to 2115 m/s with an average value of 1873 m/s and a standard deviation of 142 m/s. Both estimates calculated using the estimated range error are outside typical values expected for sand [57], [78] which indicates that the estimate of +/- 50 m range uncertainty used in Chapter 4 was likely high. This does, however, demonstrate the impact range uncertainties can have on these compressional wave speed estimates.

Another potential source of error arises from the assumption of the peak pressure corresponding to the main water arrival introduces some uncertainty as multipath effects could potentially result in the true water arrival arriving at an earlier time. To determine the error caused by this assumption a second analysis was conducted where the main water arrival was assumed to correspond to the first high frequency arrival following the ground wave. An example that considers the 6 kg NEW charge recorded at 430 m is shown in Figure 5.22 where the peak pressure corresponds to 0 s and the first high frequency arrival occurs at -0.00112 s relative to the peak pressure. Estimates of the compressional wave speed in the seabed based on this analysis is in the range of 1590 m/s to 1673 m/s with an average of 1634 m/s and a standard deviation of 25 m/s. While it is important to consider this source of error, it is not expected to have a considerable impact on this study. The initial average estimate of 1625 m/s is in good agreement with literature values and is used in this study for the compressional wave speed in the sand half-space. These parameters are summarized in Table 5.2.

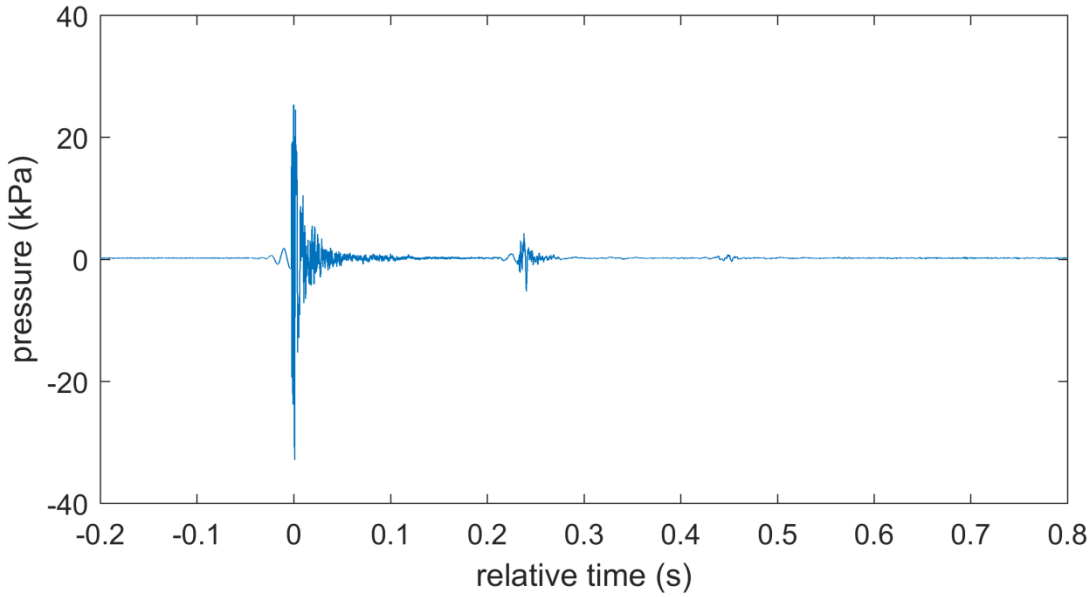

Figure 5.21. Time series from the Virginia Beach experiment for the 6.0 kg charge measured at 950 m range. Time 0 s corresponds to the main water arrival, with the precursor arrival arriving before this.

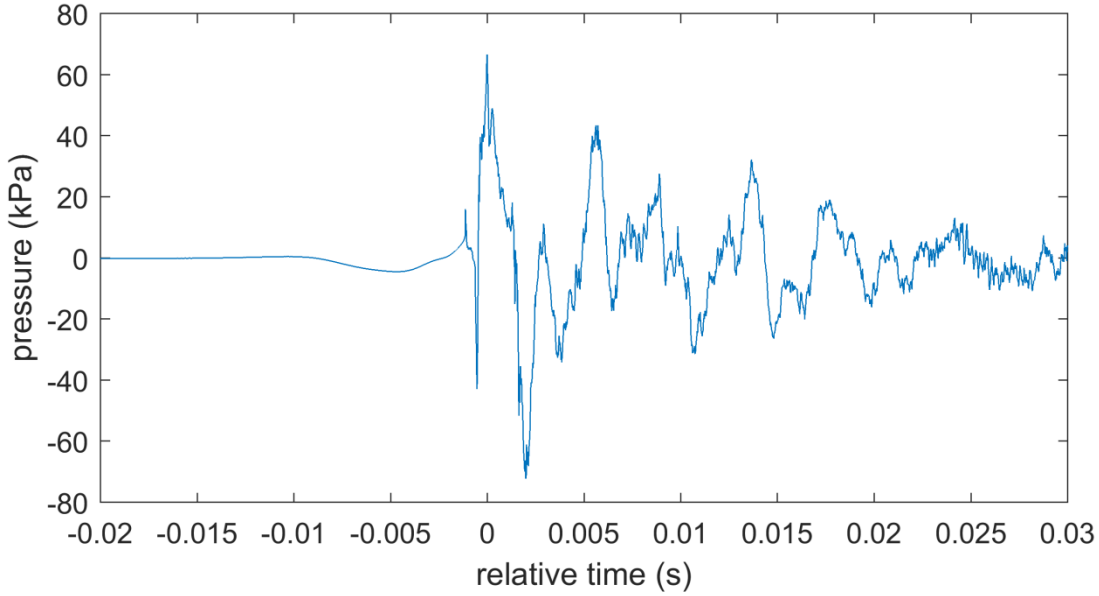

Figure 5.22. Time series from the Virginia Beach experiment for the 6.0 kg charge measured at 430 m range with a compressed time scale in around the main water arrival. Time 0 s corresponds to the main water arrival assumed to correspond to the peak absolute pressure.

Table 5.3. Summary of the Virginia Beach arrival times for the main water arrival and precursor arrivals used for calculating the compressional wave speed in the seabed. A water sound speed of 1528 m/s was used in the calculations.

weight (kg NEW)	test	range (m)	water arrival (s)	precursor arrival time (s)	compressional Speed (m/s)
0.5	1	430	0.281	0.266	1618
1	2	430	0.281	0.267	1610
5	3	430	0.281	0.266	1618
10	1	430	0.281	0.261	1645
0.5	1	165	0.108	0.104	1592
1	2	165	0.108	0.102	1623
5	3	950	0.622	0.578	1643
10	1	950	0.622	0.573	1658

5.3.1.3 Silver Strand

The Silver Strand Measurement site is also characterized by sandy seabed so a similar geoacoustic model to the Virginia Beach site is used. This geoacoustic model differs from the Virginia Beach model in the water sound speed, which is characterized by a thermocline at 15 m (discussed earlier), and in the compressional sound speed which has also been calculated using the precursor arrivals measured on the single element autonomous system at both receiver ranges for all four trials. Calculating the compressional wave speed at the Silver Strand site utilizes a similar approach as Virginia Beach for calculating the compressional wave speed, however it is complicated by the presence of the thermocline. The main water arrival is also assumed to correspond to the peak pressure, and the arrival time of this feature relative to the detonation has been calculated using three water sound speeds; a lower limit of 1493 m/s (Table 5.4), and an upper limit of 1510 m/s (Table 5.5). Differences in the estimates are typically less than 20 m/s. As a result a value of 1500 m/s has been used as the water sound speed to estimate the compressional wave speed in the seabed (

Table 5.6). Utilizing measurements from the single element autonomous systems gives compressional wave speeds between 1650 m/s and 1780 m/s with an average value of 1712 m/s with a standard deviation of 43 m/s which is within the range of reasonable values for sand.

The method used to estimate the error for the Virginia Beach data that assumed the onset of the high frequency signal for Virginia Beach have also been used here. Estimates of the compressional wave speed in the seabed based on this analysis is in the range of 1655 m/s to 1786 m/s with an average of 1722 m/s and a standard deviation of 41 m/s. Considering these errors along with the errors associated with the estimates of the water sound speed give an explanation for the higher standard deviation for this experiment compared to the Virginia Beach estimates. Overall, however, these errors are not expected to adversely impact the receiver-to-receiver path loss study in this chapter. A value of 1700 m/s, which is within a standard deviation of the averaged value, is used for this study. The remaining geoacoustic parameters could differ between the Virginia Beach and Silver Strand sites, however this geoacoustic model is sufficient for the purposes of this work. These parameters are summarized in Table 5.2.

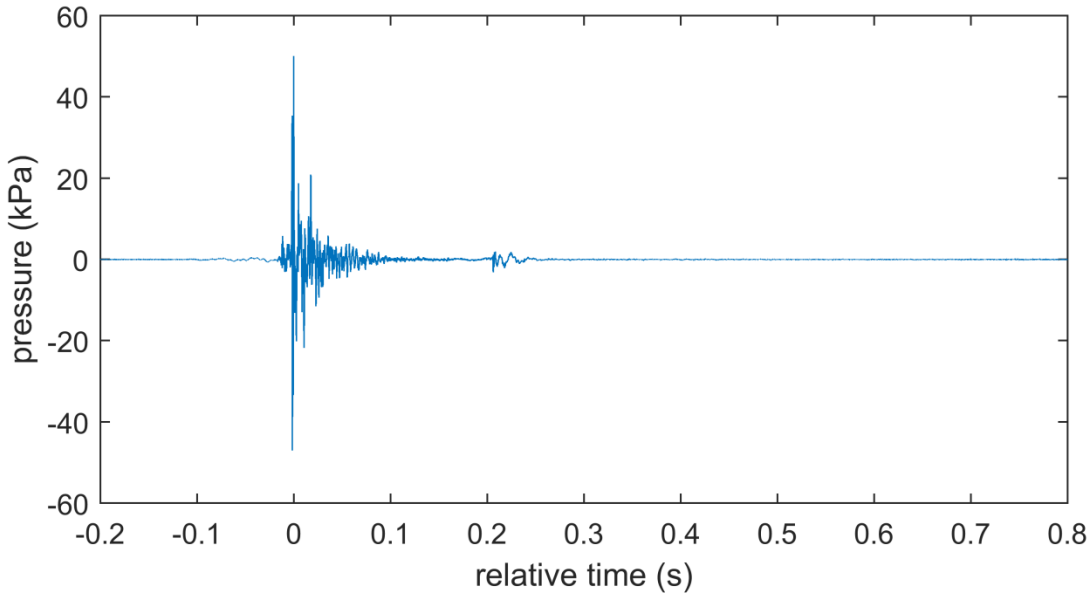

Figure 5.23. Time series from the Silver Strand experiment for the 6.0 kg charge measured at 1255 m range. Time 0 s corresponds to the main water arrival, with the precursor arrival arriving before this.

Table 5.4 Summary of the Silver Strand arrival times for the main water arrival and precursor arrivals used for calculating the compressional wave speed in the seabed. A water sound speed of 1493 m/s was used in the calculations.

weight (kg NEW)	test	range (m)	water arrival (s)	precursor arrival time (s)	compressional Speed (m/s)
6	day 1-1 near	512	0.343	0.301	1699
6	day 1-2 near	784	0.525	0.477	1645
6	day 2-1 near	685	0.459	0.393	1742
6	day 2-2 near	358	0.240	0.216	1658
6	day 1-1 far	1255	0.841	0.731	1716
6	day 1-2 far	1499	1.004	0.877	1710
6	day 2-1 far	1651	1.106	0.931	1774
6	day 2-2 far	1353	0.906	0.803	1684

Table 5.5. Summary of the Silver Strand arrival times for the main water arrival and precursor arrivals used for calculating the compressional wave speed in the seabed. A water sound speed of 1510 m/s was used in the calculations.

weight (kg NEW)	test	range (m)	water arrival (s)	precursor arrival time (s)	compressional Speed (m/s)
6	day 1-1 near	512	0.339	0.298	1721
6	day 1-2 near	784	0.519	0.471	1665
6	day 2-1 near	685	0.454	0.388	1765
6	day 2-2 near	358	0.237	0.213	1679
6	day 1-1 far	1255	0.831	0.722	1738
6	day 1-2 far	1499	0.993	0.865	1732
6	day 2-1 far	1651	1.093	0.918	1798
6	day 2-2 far	1353	0.896	0.793	1706

Table 5.6. Summary of the Silver Strand arrival times for the main water arrival and precursor arrivals used for calculating the compressional wave speed in the seabed. A water sound speed of 1500 m/s was used in the calculations.

weight (kg NEW)	test	range (m)	water arrival (s)	precursor arrival time (s)	compressional Speed (m/s)
6	day 1-1 near	512	0.341	0.300	1708
6	day 1-2 near	784	0.523	0.474	1653
6	day 2-1 near	685	0.457	0.391	1752
6	day 2-2 near	358	0.239	0.215	1666
6	day 1-1 far	1255	0.837	0.727	1725
6	day 1-2 far	1499	0.999	0.872	1719
6	day 2-1 far	1651	1.101	0.926	1784
6	day 2-2 far	1353	0.902	0.799	1693

5.3.2 *Receiver-to-Receiver Path Loss (PL)*

The motivation for the receiver-to-receiver path loss (PL) analysis is to determine the frequency-dependent losses that are a result of propagation effects within the waveguide that are independent of the source. The PL, as defined here, is a measure of the difference in energy levels between two receivers. While source models exist for the explosives detonated in deep water [16], [17], it is not clear whether these models are valid in shallow water environment where the physics can become more complex and the explosion can break the water surface or cavitation can occur [68]. By looking at the PL between receivers we can isolate the effects from the environment allowing different measurement sites to be compared irrespective of the source. Starting with the pressure (either measured or modelled)

$$P(r, z, z_o, f) = S(f)g(r, z, z_o, f) \tag{5.31}$$

where P is the pressure field, f is the frequency, $S(f)$ is the frequency dependent source pressure, r is the measurement range, z_o is the source depth, z is the receiver depth, and $g(r, z, z_o, f)$ is the frequency dependent Green's function, the PL can be calculated as

$$PL(f) = 20\log_{10}(|S(f)g(r_1, z_1, z_o, f)|) - 20\log_{10}(|S(f)g(r_2, z_2, z_o, f)|) \quad (5.32)$$

$$= 20\log_{10}\left(\frac{|g(r_1, z_1, z_o, f)|}{|g(r_2, z_2, z_o, f)|}\right)$$

where PL is the path loss in dB and the subscripts 1 and 2 referring to the near and far receiver ranges respectively. Note, the path loss (PL) quantifies the change in energy between two receivers. As $g(r, z, z_o, f)$ is an output of numerical propagation models like OASES, which is used in this work, Eq. (5.32) is used for calculating the path loss from modelled data as a source term is not required. For the measured data, the receiver-to-receiver path loss can be calculated directly from the measured pressure;

$$PL(f) = 20\log_{10}\left(\frac{|P(r_1, z_1, z_o, f)|}{|P(r_2, z_2, z_o, f)|}\right) \quad (5.33)$$

Following the notation in Eq. (5.32) the third-octave path loss is defined as follows;

$$PL_{1/3}(f) = 10\log_{10}\left(\frac{\int_{f_{low}}^{f_{high}} |g(r_1, z_1, z_o, f)|^2 df}{\int_{f_{low}}^{f_{high}} |g(r_2, z_2, z_o, f)|^2 df}\right) \quad (5.34)$$

With f_{low} and f_{high} corresponding to the lower band limit and upper band limit of the third-octave bands. For the measured data, pressure $P(r, z, z_o, f)$ can be substituted for the Green's function, $g(r, z, z_o, f)$, in Eq. (5.34).

5.3.2.1 Measured Path Loss

The receiver-to-receiver path loss for the Pu`uloa, Virginia Beach, and Silver Strand experiments are shown in Figure 5.24, Figure 5.25, Figure 5.26 respectively. For a given charge weight, Pu`uloa data are generally consistent. Comparing the 750 m to 1500 m range PL for the 2.3 kg NEW and 8.0 kg NEW charges we see distinct differences for the two charge weights with the 2.3 kg NEW charges generally showing lower path loss between the 63 Hz and 800 Hz third-octave bands. The PL for the 2.3 kg NEW and 8.0 kg NEW charges are expected to be in good agreement given they were measured at the same receiver locations. Additionally, one the 8.0 kg NEW charges exhibits lower path losses than the other two. During the experiment one of the

charges misfired resulting in a lower than expected yield, however since the receiver-to-receiver path loss is independent of the source this should not impact the results.

To explain these differences, the ESD for the 4.5 kg NEW charges are compared to the equipment self-noise as shown in Figure 5.27. Between 80 and 650 Hz the ESD for the 1500 m receiver is equal to the equipment noise and the 500 m data is 25 dB above the noise (this is the measured receiver-to-receiver path loss shown in Figure 5.24 for the same charges). Similar results are shown for the 2.3 kg NEW and 8.0 kg NEW charges measured at 750 m and 1500 m with the 2.3 kg NEW exhibiting lower levels that are closer to the noise floor. This greatly limits the measurable path loss for third-octave bands between 80 and 1250 Hz and likely results in lowered measured values.

The low signal to noise ratio provides an explanation for the differences in the receiver-to-receiver path loss differences as well as the discrepancy between one of the 8 kg NEW charges and the other two charges of the same weight. Unlike the Pu`uloa experiment, the Virginia Beach data and the Silver Strand data are well above the noise floor with the measured receiver-to-receiver path loss giving an accurate representation for all third-octave bands.

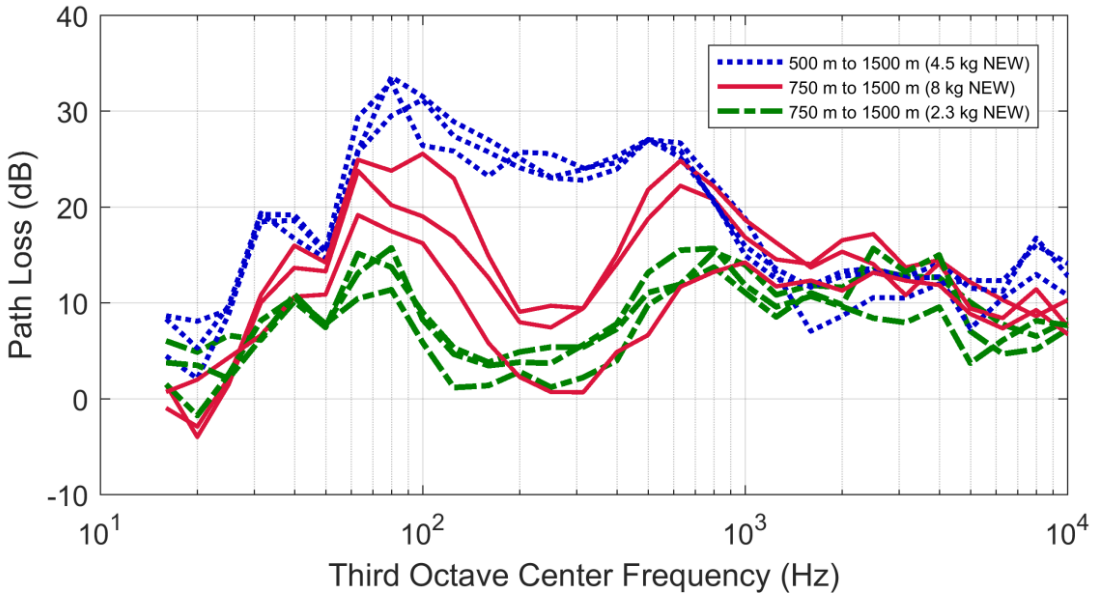

Figure 5.24. Measured receiver-to-receiver path loss from the Pu`uloa experiment. The 500 m to 1500 m ranges are from the 4.5 kg NEW charges (dotted line), and the 750 m to 1500 m ranges are from the 2.3 kg NEW (dashed line) and 8.0 kg NEW charges (solid line).

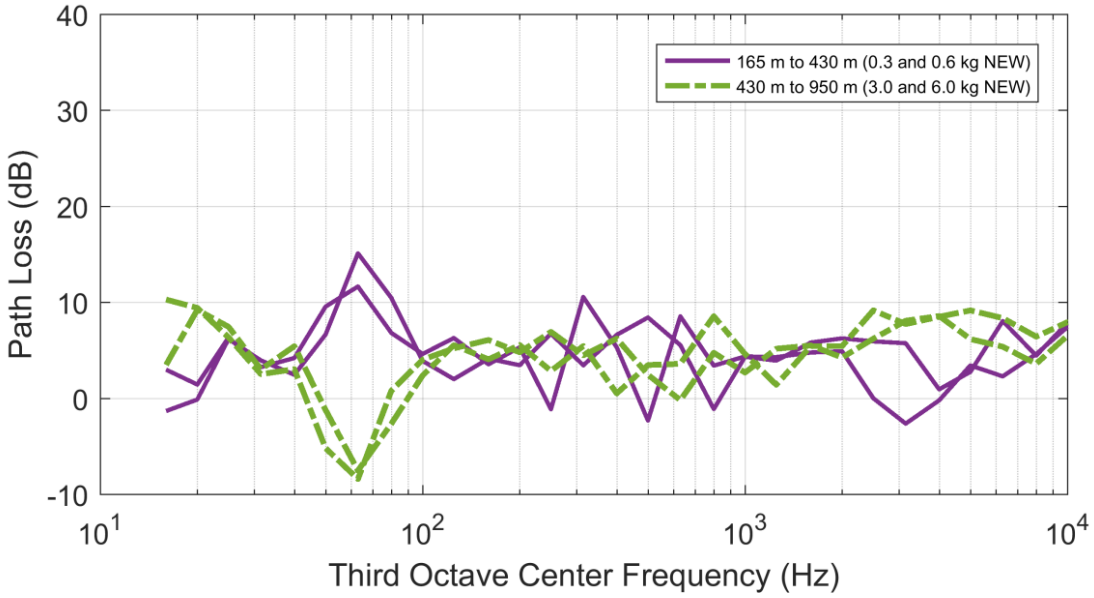

Figure 5.25. Measured receiver-to-receiver path loss from the Virginia Beach experiment. The 165 m to 430 m ranges are from the 0.3 and 0.6 kg NEW tests, and the 430 to 950 m ranges are from 3.0 and 6.0 kg NEW charges.

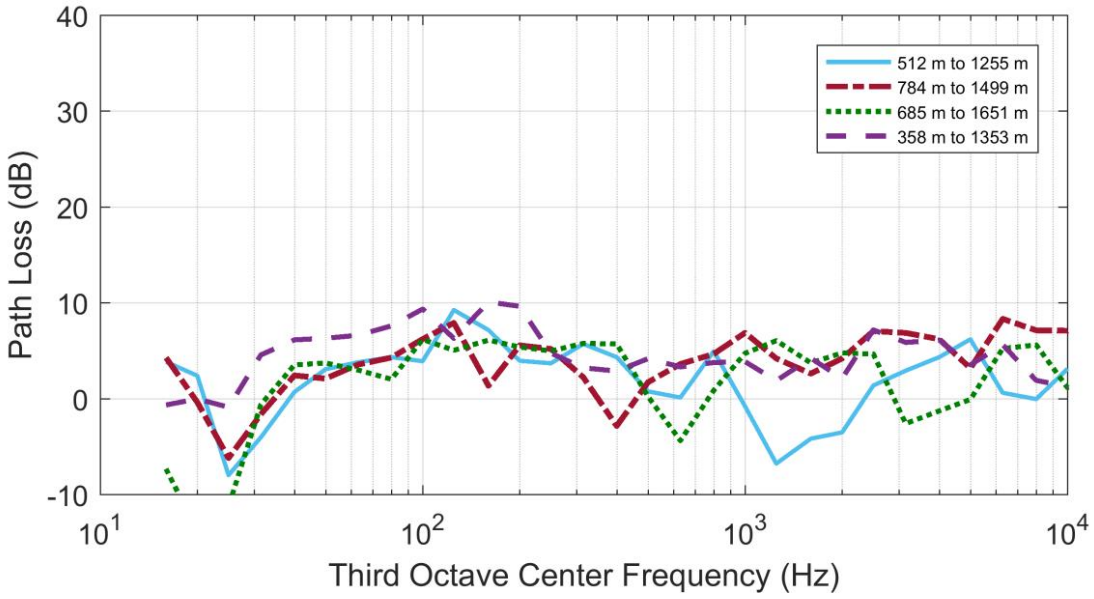

Figure 5.26. Measured receiver-to-receiver path loss from the Silver Strand Training Complex experiment. All four tests are 6.0 kg NEW charges.

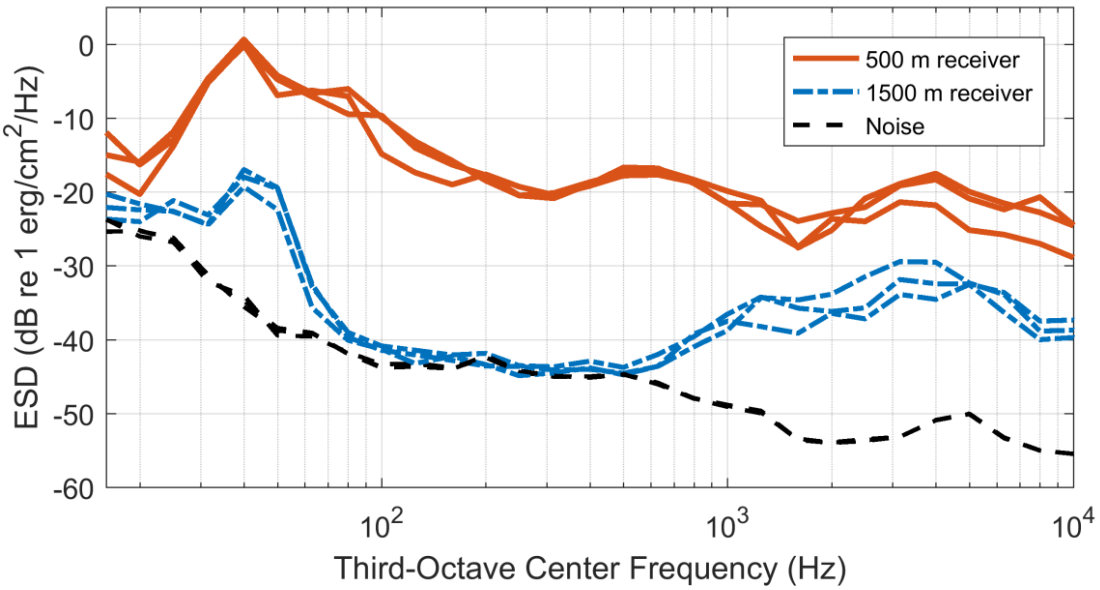

Figure 5.27. Comparison of the equipment self -noise to the ESD for the three 4.5 kg NEW charges measured at 500 m and 1500 m. Between 80 and 650 Hz the ESD for the 1500 m receiver is buried in the noise. The 500 m data is 25 dB above the noise.

5.3.2.2 Modelled Path Loss

Predictions for the receiver-to-receiver path loss have been computed for the two experiments using the OASES wavenumber integration model [29] to calculate the frequency dependent Greens function between 14.1 Hz and 11,220 Hz. This corresponds to the lower and upper limits of the 16 Hz and 10,000 Hz third-octave bands respectively. Third-octave band receiver-to-receiver path losses for the simulations are then computed and compared to the measured data (Figure 5.28). The Pu`uloa data in Figure 5.28 are from one of the 4.5 kg NEW charges with receivers at 500 m and 1500 m, the Virginia beach data are from the 6.0 kg NEW charge measured at 430 and 950 m, and the Silver Strand data are from 6.0 kg NEW charge measured at 512 m and 1255 m. The environments in the simulations are described using the geoacoustic models discussed in Section 5.3.1.

Comparing the Pu`uloa data to the model results shows good agreement with high losses between the 50 Hz and 1600 Hz third-octave bands and comparatively lower loss above 1600 Hz. While the model shows higher losses than the measured data at the 250 Hz third-octave band, this is most likely explained by the low signal to noise ratio in the measurements. Above 1600 Hz the Pu`uloa data and model results are in good agreement and typically differ by less than 5 dB.

Comparing the Virginia Beach model result to the measured 6.0 kg NEW path losses (Figure 5.28) there is reasonable agreement above 100 Hz. There are larger differences at the 400 Hz and 630 Hz third-octave band, but otherwise the differences are typically than 5 dB. In spite of these differences, these results do not show the high path losses between 50 Hz and 1600 Hz observed in the Pu`uloa data. Similar results are observed for the the Silver Strand model above, although some third-octave bands have differences of up to 10 dB. Overall, however, there is reasonable agreement between model and data. Below 100 Hz, there is poor agreement between the Virginia model results and the data and below 40 Hz there is poor agreement between the Silver Strand model results and the data. This is potentially due to seabed refraction and is explored further in the next chapter.

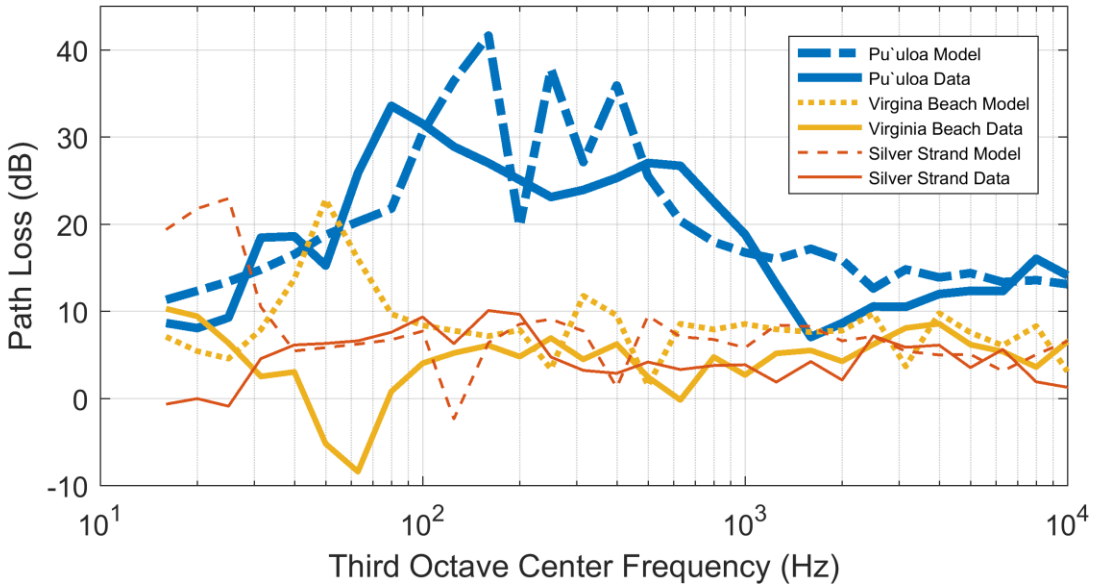

Figure 5.28. Comparison of the measured path loss for the Pu`uloa ,Virginia Beach, and Silver Strand experiments compared to path loss modeled using the OASES wavenumber integration model [29]. The Virginia Beach and Silver Strand model results employed a Pekeris waveguide environmental model, whereas the Pu`uloa model results were computed using a thin (0.5 m) sand layer overlying a limestone half-space.

5.3.3 *Analytical Reflection Loss (RL) Model*

In this section, the RL from a fluid seabed is compared to the RL from a shear supporting seabed. The reflection loss is calculated using Eq. (2.22), with the reflection coefficient, R, calculated using an analytical reflection coefficient model from Chapman and Chapman [63] described in Eq. (2.21) (herein referred to as the Chapman-Chapman model). The goal of this comparison is to demonstrate how shear effects in the seabed are contribute to the high losses observed in the Pu`uloa data (Figure 5.24).

The RL has been calculated using the geoacoustic model for the Pu`uloa site. The seabed is modeled as a thin sand layer (0.5 m thickness) overlying a limestone half-space, and two cases are considered; the first for a fluid seabed model (shear waves are not supported) shown in Figure 5.29(a) and, the second, a fully elastic seabed model shown in Figure 5.29(b).

By comparing the two models we see that above 1000 Hz the RL are consistent. Below 1000 Hz, for grazing angles less than 45°, relatively high RL is observed in the elastic model (Figure 5.29(b)) but not in the fluid model (Figure 5.29(a)). The high RL in the elastic seabed model are consistent with the Pu`uloa data and the modeled path losses (Figure 5.24). This indicates that the high losses between 50 and 1600 Hz (for the case with acceptable signal to noise) are likely due to the conversion of compressional waves to shear waves in the elastic seabed. Above 1600 Hz, in-sediment attenuation effects in the thin sand layer dominate and results in losses more consistent with a sandy seabed. This is supported by the reasonable agreement of the Pu`uloa data to the Virginia Beach and Silver Strand data.

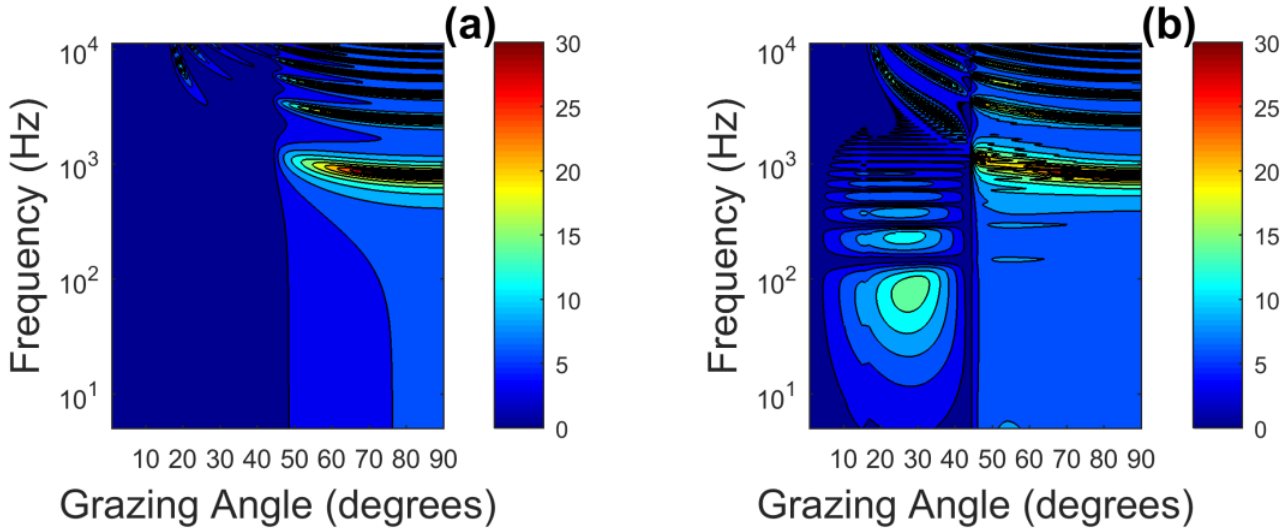

Figure 5.29. The RL (Eq. (2.21)) calculated using the Chapman-Chapman reflection coefficient model from Eq. (2.22) for a two layer seabed model consisting of a sediment layer with thickness 0.5 m and a limestone half-space for (a) a fluid seabed model and (b) an elastic seabed model. The color bar is in dB.

5.3.4 *Sea Surface Roughness and Bathymetric Refraction*

Sea surface roughness and bathymetric refraction are both mechanisms that can cause increased attenuation in shallow water environments. While the effects of the sea surface could potentially play a role, we would not expect the effects to occur over a narrow frequency band as seen in these data. Instead, the effects would be more pronounced as frequency increases. A similar

analysis was undertaken by Hughes et al. [61] which ruled out seabed roughness as the primary mechanism causing increased losses at low frequencies.

Bathymetric refraction, which can also cause high losses that are frequency dependent, is unlikely given that the slope of the seabed perpendicular to the source-receiver transect is less than 0.5^o . The acoustic data recorded offshore on the VLA also show the high losses indicating that bathymetric refraction is not responsible as the bathymetry does not vary considerably perpendicular to this transect (Figure 3.1).

5.4 CONCLUSIONS

In this chapter, measurements from underwater explosions collected at the U.S. Navy Pu`uloa Underwater Detonation Range have been presented and compared to data collected at a training range 7 km off the coast of Virginia Beach, VA and at the Silver Strand Training Complex. The peak pressure and SEL from the Hawaii data were shown to be up to 25 dB lower than levels measured during the other two experiments. Looking at the ESD of these data at third-octave bands between 50 and 1600 Hz, the Pu`uloa data were up to 25 dB lower than the other two measurements. Outside of this frequency band the three experiments are in reasonable agreement and typically differ by less than 5 dB.

By computing the path loss between receivers and comparing these to numerical models computed with OASES, the effects of the seabed at the different measurement sites were compared independent of the source. The modeled path losses for the Pu`uloa site were in reasonable agreement with the measurements at ranges and frequencies where signals exceed the equipment noise floor when the seabed was modelled as a limestone bottom topped with a thin sand layer. The measured data differed from the model results by 20 dB at the 250 Hz third-octave band, this was explained by comparing the ESD of the Pu`uloa measurements to the equipment noise floor. Due to low signal to noise ratio at the 1503 m range, the measureable receiver-to-receiver path loss was limited to the difference between the close range (between 500 m and 800 m) and the noise floor of the far range. The predicted path losses for the other two experiments were also in good agreement with the measurements when the seabed was modelled as unconsolidated sandy sediment, consistent with the geoacoustic environment.

The receiver-to-receiver path losses for the Pu`uloa experiment were also considered using an analytical reflection loss model to compare the reflection loss for a fluid seabed to an elastic seabed. This comparison showed that the high losses are most likely a result of the conversion of compressional to shear waves in the seabed, and these effects would not occur in a seabed where shear effects are neglected (or a seabed with low shear speed). At higher frequencies, the losses are consistent with a sandy seabed due to attenuation in the thin sand layer. While sea surface roughness and bathymetric refraction can cause similar effects, they are unlikely the root cause. Based on these results, the Pu`uloa peak pressure and SEL (Figure 5.1 and Figure 5.2) are likely lower than the other two sites as a result of the high losses between 50 and 1600 Hz.

Chapter 6. SEABED REFRACTION

6.1 INTRODUCTION

Simple propagation loss models, like practical spreading [30], can only explain monotonic decreases in waveguide energy. This, however, is not true when seabed refraction occurs as a result of a sound speed gradient in the seabed. In this type of a configuration, the propagation up to a certain range resembles that in a simple waveguide. However, at greater ranges that depend on the sound speed profile in the seabed and the height of the source above the ocean bottom, there is an increase in energy resulting from refracted energy re-entering the waveguide [53].

Propagation in shallow water environment where the water depth is on the order of a few wavelengths is characterized by significant interaction with the sea surface and seabed. The composition of the seabed is site specific with each bottom type (hard rock, sand, chalk, clay, for example) having unique effects on the sound propagation. This chapter focuses on sandy environment where seabed properties have been shown to be depth-dependent [91]. If the sound speed increases with depth into the seabed, as is the case with sand, sound propagating into the ocean bottom can undergo refraction. In deep water, these effects have been studied by Frisk [53] and by Stickler [56]. However, comparatively less work has been done to investigate how these effects manifest in shallow water where effects such as low frequency cut-off, described by Eq. (2.18), can occur.

In the previous chapter, model results computed for the Virginia Beach measurement site using a Pekeris waveguide for the environmental model were in poor agreement with measured data between 40 and 100 Hz (Figure 5.28). This chapter explores these results and demonstrates that this poor agreement is likely due to refraction effects within the seabed that are not accounted for in the homogeneous half-space seabed model that characterizes a Pekeris waveguide. By modifying the compressional sound speed in the seabed to increase linearly with depth, low frequency path losses are in good agreement with the data. The frequencies where refraction effects are most significant are also shown to be closely related to the cutoff frequency in the waveguide. It should be noted that the primary goal of this chapter is not to describe the best fit

model for the measurement environment, but instead explain the physical mechanisms that contribute to the observed receiver-to-receiver path losses.

6.2 RECEIVER-TO-RECEIVER PATH LOSS

Similar to the analysis in the previous chapter, to circumvent the limitations of an unknown source, receiver-to-receiver path losses can be calculated allowing the effects of the underwater environment on sound propagation to be studied irrespective of the source used as shown in Eq. (5.32).

The receiver-to-receiver path losses from the Virginia Beach experiment (Figure 5.25) show an unusual trend between 40 Hz and 100 Hz. The 430 m to 950 m path losses for the 50 Hz, 63 Hz and 80 Hz third-octave bands have negative values, corresponding to an increase in energy between the two receivers, with a distinct extrema at the 63 Hz third octave band. Between 40 and 100 Hz the path-losses between the 165 m to 430 m receivers are almost mirror images of the path loss between the 430 m to 950 m receivers. All third-octave bands with this frequency band are positive, corresponding to a decay of energy with range with a maximum path loss observed at the 63 Hz third-octave band.

While multi-path propagation in shallow water can result in complicated patterns of constructive and destructive interference, the nature of the path losses between 40 Hz and 100 Hz are unusual given they are nearly mirror images of one another and consistent for charges of different weights measured at the same receiver ranges. In the previous chapter, path losses at the Virginia Beach measurement site were calculated using a Pekeris Waveguide for the environmental model (Figure 5.28). Above 100 Hz the data and model results are in reasonable agreement, however the receiver-to-receiver path losses are in poor agreement in the frequency bands considered here. This indicates that some other mechanism not accounted for in the Pekeris waveguide model is responsible for these effects. The following sections show that these losses are likely a result of seabed refraction caused by a depth dependent compressional wave speed in the seabed. We also show that the frequencies where refracted arrivals are observed are closely related to the cutoff frequency of the waveguide.

6.3 GEOACOUSTIC MODELS

In this study two geoacoustic models for the seabed is considered; a Pekeris Waveguide model used in the previous chapter and a depth-dependent seabed model where the compressional wave speed increases with depth into the seabed. For both models, the sound speed in the water is 1528 m/s, the density is 1024 kg/m^3, and the thickness of the water layer is 16 m.

6.3.1 *Homogeneous Half-Space Seabed Model*

The goal of using a homogeneous half-space seabed model is to consider propagation in an environment where there refraction in the seabed does not occur. This estimate puts the compressional wave speed between 1590 m/s and 1650 m/s. For this study, the average value of 1625 m/s discussed in the previous chapter is used. The density for the seabed is assumed to be 2000 $\mathrm{kg/m^3}$ based on literature values [57], and a shear speed of 300 m/s is used. Compressional and shear attenuation factors of 0.2 dB/λ and 1.0 dB/λ respectively is also assumed based on the previous work by Soloway and Dahl 2015 [81].

6.3.2 *Depth Dependent Seabed Model*

The depth dependent seabed model is motivated by a previous study by Soloway and Dahl 2015 [81] which used Scholte interface waves to find a power-law dependent shear wave speed profile. The best fit model from this study, which is used for the shear speed in the depth dependent seabed model, is $c_s(z) = 102\, Z^{0.367}$ where c_s is the shear wave speed in m/s and Z is the depth below the water-sediment interface in meters. The previous chapter assumed a constant compressional wave speed in the seabed, however in this chapter the compressional wave speed in the sandy seabed is modeled using a linear sound speed profile that increases with depth below the water-sediment interface described in Eq. (2.20). In this study c_o is given a fixed value and a range of values of β are explored as it is the gradient within the seabed that is responsible for refraction. In the following sections the value of c_o is fixed at 1590 m/s, so that the effects of β on the seabed refraction can be explored.

Similar to the homogeneous half-space model, a density of 2000 kg/m^3, a compressional wave attenuation factor of 0.2 dB/λ and a shear attenuation factor of 1.0 dB/λ are assumed. The value for the density differs slightly from the study by Soloway and Dahl 2015 and has been updated to better reflect literature values for sand.

6.4 METHODOLOGY

6.4.1 *CW Model*

To investigate whether a depth dependent seabed is responsible for the unusual receiver-to-receiver path losses at the Virginia Beach measurement site (Figure 5.25) a continuous waveform (CW) model (e.g. continuous, single frequency source) is first employed to investigate the relation between the seabed gradient and the resulting sound field for a range of frequencies. This helps determine two important points; (1) whether for typical values of β the range at which refracted arrivals re-enter the waveguide are in the vicinity of the 950 m receiver (e.g. the 430 receiver is in the shadow zone and the 165 m receiver is at a close enough range that the pressure field has not experienced considerable decay) and (2) help determine whether there is a relation between the cutoff frequency in the waveguide and the frequencies where the negative path losses occur. Green's function for the CW model results are computed using the OASES wavenumber integration model [29] with the environment defined using the geo-acoustic models in the previous section and a source infinitely close to the seabed (16 m source depth but no contact with the interface occurs). As OASES cannot model an elastic layer with a linear sound speed profile, the gradient is approximated using an equal layer travel time approach from Godin and Chapman [92] (this is referred to as a Goupillaud medium in geophysics). The Green's function is computed for ranges between 1 m and 1000 m in 9 m increments and depths between the sea surface and the seabed (0 m to 16 m) in 0.5 m increments.

6.4.2 *Equal Layer Travel Time Model for Linear Sound Speed Gradient*

The field is also computed for a range of frequencies to investigate the relationship between the cutoff frequency and the refraction effects within the seabed. An equal layer travel time approach, based on the methods employed by Godin and Chapman [92], has been used to model

the continuous, linear sound speed profile in Eq. (3) using a series of stacked layers. The idea behind this approach is to choose a sound speed and thickness for each layer such that the travel time through all layers, $\Delta\tau$, is the same. Following the approach of Godin and Chapman, this requires that the travel time through each layer is equal to;

$$\Delta\tau = \int_{z_m}^{z_{m+1}} \frac{dz}{c_p(z)} \tag{6.35}$$

where z is the depth below the water-sediment interface, $c_p(z)$ is the depth dependent sound speed, and m denotes the layer where $m = 0, 1, 2, \ldots, M$ for a seabed represented by M layers and the water sediment interface denoted $m = 0$. The sound speed through each layer is then equal to;

$$c_m = \frac{\Delta z}{\Delta\tau} = \frac{z_{m+1} - z_m}{\Delta\tau} \tag{6.36}$$

where Δz is the thickness of layer m. Substituting Eq. (2.20) into Eq. (6.35) and integrating gives the travel time in the layer;

$$\Delta\tau = \frac{1}{\beta} \ln\left(\frac{c_o + \beta z_{m+1}}{c_o + \beta z_m}\right) \tag{6.37}$$

Defining the thickness of the first layer ($m = 1$) as z_1 the travel time in the first layer from $z_0 = 0$ m to z_1 is;

$$\Delta\tau_1 = \frac{1}{\beta} \ln\left(\frac{c_o + \beta z_1}{c_o}\right) \tag{6.38}$$

As the travel time through all layers is the same, this is equivalent to setting Eq. (6.38) equal to Eq. (6.37)

$$\Delta\tau = \frac{1}{\beta} \ln\left(\frac{c_o + \beta z_1}{c_o}\right) = \frac{1}{\beta} \ln\left(\frac{c_o + \beta z_{m+1}}{c_o + \beta z_m}\right) \tag{6.39}$$

Rearranging Eq. (6.39), the depth of layer $m+1$ can then be found with respect to layer m;

$$z_{m+1} = \frac{1}{\beta}\left[\frac{(c_o+\beta z_1)(c_o+\beta z_m)}{c_o} - c_o\right] \tag{6.40}$$

Eq. (6.39) and Eq. (6.40) are then used in Eq. (6.36) to calculate the sound speed through layer m.

Defining the depths and sound speeds of each layer using Eq. (6.40) and Eq. (6.36) respectively, the seabed for this study is divided into 75 layers and the thickness of the first sediment layer, z_1, is set to 2 m. A sensitivity study (Appendix C) has shown that these values give good results and choosing a larger number of layers or a smaller value for z_1 does not impact the model results. Layer M, where m = 75, in the seabed is a half-space at a depth of between 160 m and 180 m (depending on β) with bottom properties that are calculated for layer M using Eq. (6.36)

The Green's function within the water column with respect to depth is calculated between 1 m and 16 m in 1 m increments, and with respect to range from 1 m to 1000 m in 9 m increments. For this study, c_o in Eq. (2.20) has been fixed at 1620 m/s and the field is calculate for four values of β; 0.5 s^{-1}, 1.5 s^{-1}, 2.0 s^{-1}, and 2.5 s^{-1}. The value for c_o is fixed as β is the parameter that controls the degree to which refraction occurs. These results are also compared to CW results computed for the half-space seabed model described in the previous section. A sensitivity study exploring the effects of the thickness of the first layer, z_1, the seabed density, ρ, the depth of the half-space, D_{max}, and the sounds speed at a depth z = 0 m, z_1, can be found in Appendix C.

6.4.3 *Cutoff Frequency of Pekeris Waveguide*

A simple analytical equation determining the cutoff frequency in a waveguide with a depth dependent seabed is not available, however an approximation can be made if we consider the effects at the interface between the water layer and the first layer in the depth dependent seabed (defined by a sound speed of c_o). If the environment is considered as a Pekeris waveguide, the cutoff frequency is given by Eq. (2.18). The water sound speed in this environment was measured to be 1528 m/s and the sound speed in the seabed is between 1590 and 1650 m/s as

discussed in the previous Chapter. Using these values in Eq. (2.18) gives a cutoff frequency between 63 Hz and 86 Hz; this is roughly the frequency range being considered. In the following section the CW model for a range of seabed gradients, β, is considered for frequencies lower than this cutoff frequency (40 Hz), close to the cutoff frequencies (60 Hz and 80 Hz) and above the cutoff frequency (100 Hz). The goal being to demonstrate the frequencies of the negative path losses in Figure 5.25 are closely related to the cutoff frequency in the waveguide.

6.4.4 *Broadband Path Loss Model*

As the primary goal of this work is to understand the measured receiver-to-receiver path loss, a broadband model of the path loss in the homogeneous half-space medium and the gradient medium are compared to the measured data. The third-octave band path loss is presented requiring the field to be computed for discrete frequencies from 14.1 Hz (lower band limit of 16 Hz third-octave band) to 11,220 Hz (upper band limit of the 10,000 Hz third octave band) using a frequency spacing of 0.25 Hz up to a frequency of 32,000 Hz (samples/s). While the measured data were sampled at 62,500 samples/s, this sampling frequency was selected for computational efficiency. The measured data were therefore down-sampled accordingly to ensure an accurate comparison.

Similar to the CW model, the path is computed using OASES with the seabed defined using the geoacoustic models described in Chapter 5 and the measurement geometry, including source and receiver depths, defined in the measurement descriptions.

6.5 RESULTS AND DISCUSSION

6.5.1 *CW Model*

The results for the CW model (Figure 6.1) showing the magnitude of the Green's function, $20\log_{10}|g(r,z,z_o,f)|$, for 40 Hz and a low gradient of 0.5 s^{-1}, do not show evidence of refraction at the ranges considered in this work. Increasing the gradient to 1.5 s^{-1}, effects from refraction are evident with the 165 m receiver in the nearfield, the 430 m receiver in a shadow zone, and the 950 m receiver at a range where the refracted energy is returned to the waveguide.

The level of the 950 m receiver is up to 6 dB higher than at the 430 m range, similar to the measured path loss. Increasing the gradient to 2.0 s^{-1}, the amplitude of the refracted arrival increases and the range where the refracted energy re-enters the waveguide is shifted to smaller ranges. This is expected as the larger gradient causes the rate of refraction within the seabed to increase. This trend is continued as the gradient is further increased to 2.5 s^{-1}. This indicates that both the measurement range and the gradient within the seabed determine the magnitude of the path loss that is observed between receivers.

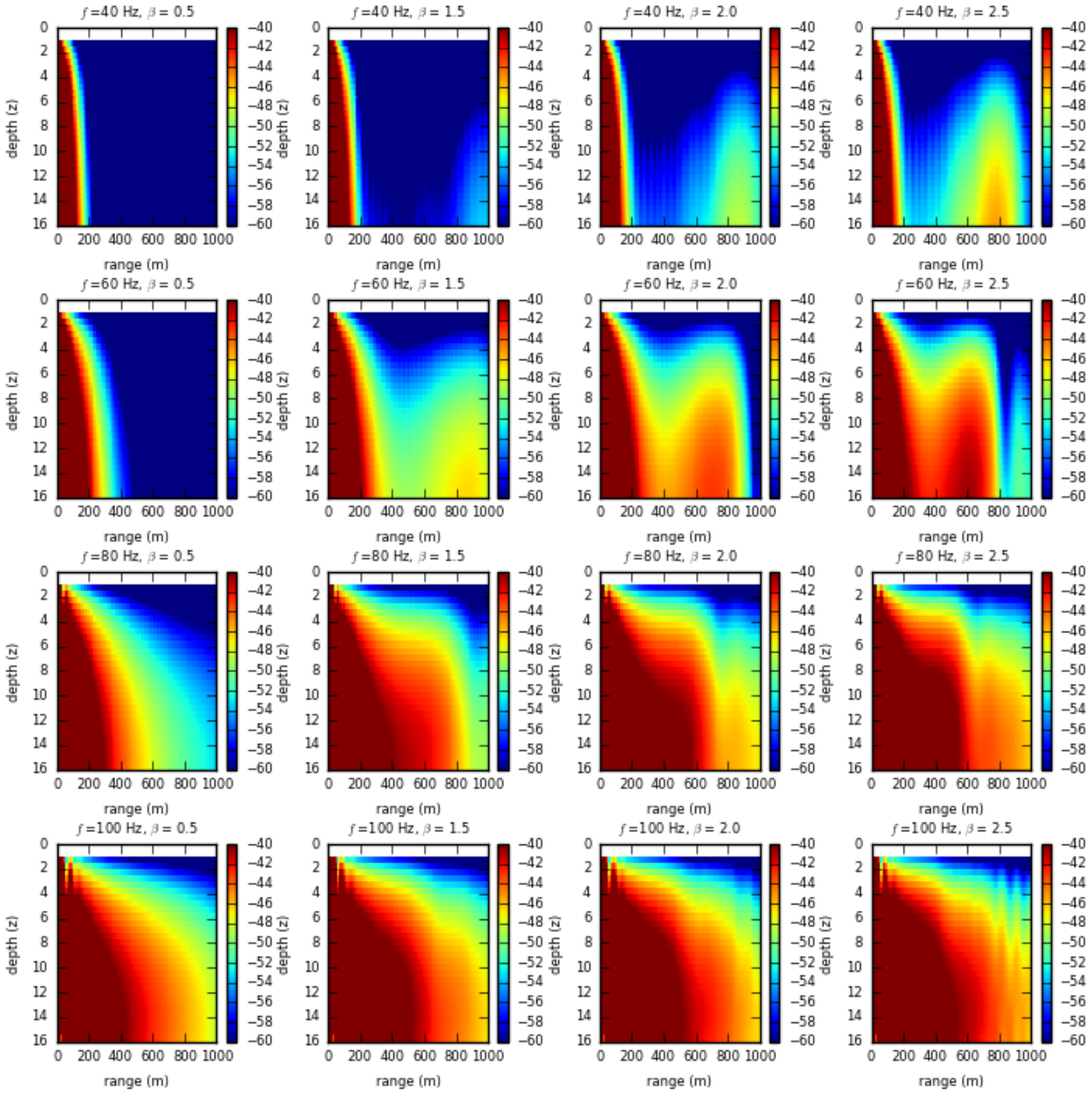

Figure 6.1. CW model results showing the magnitude of the Green's function, 20log10(|g(r,z,zo,f)|), for a range of β increasing from left to right and frequencies increasing from top to bottom. For these figures, a value of 1590 m/s for c_o in Eq. (2.20) was used. The colorbar is in units of dB.

6.5.2 *Cutoff Frequency*

Having considered the effects of refraction for 40 Hz, the CW model is repeated for 60 Hz, 80 Hz and 100 Hz (Figure 6.1); 60 Hz and 80 Hz are within the possible range of the cutoff frequency determined using Eq. (2.18) and 100 Hz is a higher frequency where trapped modes are expected to occur. The CW field for 60 Hz shows similar trends as the 40 Hz case, however the amplitude of the refracted arrivals are comparatively higher for a given value of β. Another observable trend is that the range where the refracted energy re-enters the waveguide is shorter for the 60 Hz case, although similar to 40 Hz, increasing β decreases this range.

Increasing the frequency to 80 Hz (Figure 6.1) shows a dramatic departure from the 40 Hz and 60 Hz results. For low values of β the field begins to resemble a field dominated by single mode propagation. As β is increased to 1.5 s^{-1} evidence of refracted arrivals can be observed, however the refracted energy entering the waveguide is not distinct from the single mode propagation and no shadow zone is observed. Increasing the gradient to 2.0 s^{-1} shows weak refracted arrivals at 850 m, however the amplitude of this arrival is significantly lower than the field at 450 m which is dominated by the trapped modes. Alternatively, the range at which the refracted energy re-enters the seabed coincides with the trapped mode propagation. When β is increased to 2.5 s^{-1}, the results are similar to the 2.0 s^{-1} case, although the refracted energy re-enters the waveguide at a closer range of 700 m.

Further increasing the frequency to 100 Hz shows increasing β has a minimal impact on the field with minor effects from refraction visible beyond 800 m. Similar to the 80 Hz case, a shadow zone which would be responsible for the negative path losses observed in the measurements (Figure 5.25) are not present indicating that while some energy at this frequency undergoes refraction in the seabed, the overall effect on the field is small. The field is instead dominated by single mode propagation. Based on the cutoff frequency for a Pekeris waveguide, this analysis supports the hypothesis that the negative path loss is related to the waveguide cutoff frequency.

6.5.3 *Modelled Path Loss*

The modelled receiver-to-receiver path loss calculated using Eq. (5.32) has been computed for the homogeneous half-space seabed model and for the gradient seabed model (Figure 6.2). A value of 1.5 s^{-1} for β has been selected based on observation from the CW analysis. This value was selected as the CW model showed the most distinct shadow and lit zones around the 430 m and 950 m receivers respectively. The model results are compared to data from the 0.3 kg test measured at the 165 m to 430 m receiver ranges (Figure 6.2a) and data from the 6.0kg test measured at the 430 m to 950 m receiver ranges (Figure 6.2b)

Comparing the modelled receiver-to-receiver path loss to the data for the 165 m to 430 m range (Figure 6.2a) shows that, in general, the path losses for both seabed models are in good agreement above 100 Hz with differences typically less than 5 dB. The highest loss in the data of 15 dB occurs at the 63 Hz third-octave band whereas the highest path losses for the two seabed models occurs at 50 Hz third-octave band; however the loss is higher at 20 dB for the gradient seabed model and 25 dB for the homogeneous half-space model. To determine whether this difference in frequency is due to the assumed compressional wave speed values, a sensitivity study looking at the impact of the seabed compressional sound speed on the path loss shows that increasing the sound speed decreases the frequency where the peak loss occurs and decreases the magnitude of the loss. Overall, it can be concluded that both seabed models give reasonable agreement with the data although the gradient seabed model gives a slightly better fit due to the lower value of the maximum path loss.

Moving on to the 430 m to 950 m receiver-to-receiver path losses (Figure 6.2b), it is immediately apparent that the homogenous half-space model differs considerably from the data below the 100 Hz third octave band. For the gradient seabed model, the overall trends observed in the data are reproduced with a similar negative valued path loss. The gradient seabed model does differ from the data at the frequency where this negative path loss occurs (63 Hz for the data and 40 Hz for the model) and in the magnitude with the data having a magnitude of -8 dB and the gradient seabed model having a magnitude of -4 dB. Above 100 Hz both models are in reasonable agreement with the data with differences of less than 5 dB. Interestingly, comparing the

homogeneous half-space seabed model to the gradient seabed model above 80 Hz shows the two are almost identical with only minor differences of less than 2 dB.

In order to explore the relation between the third-octave band where the negative path loss occurs and the value of c_o, a second gradient seabed model is considered with a lower value of 1550 m/s for c_o (Figure 6.3). By lowering c_o in Eq. (2.20) the location of the minimum value increases from 40 Hz to 50 Hz (Figure 6.3b) and the magnitude of this minimum decreases from -4 dB to -5 dB. Overall, these differences are small compared to the differences between the data and homogeneous half-space model which differ by up to 21 dB and 12 dB at the 50 Hz and 63 Hz third-octave bands respectively.

As noted for both receiver combinations, above 100 Hz both the homogeneous half-space and gradient seabed models are in reasonable agreement with both the data and in good agreement with each other. The real differences occur at frequencies below 100 Hz where results indicate that a gradient seabed model provides a significantly better fit to the data. Additionally, these results also indicate that the gradient in the seabed is responsible for negative path losses at the 430 m to 950 m ranges. These results are in good agreement with the CW models shown in Figure 6.1.

The reasonable agreement between the gradient model and Pekeris waveguide environmental models above 100 Hz can be understood by considering these results in the context of the waveguide cutoff frequency. As the homogeneous half-space model has a compressional wave speed of 1590 m/s, from Eq. (2.18) this gives a cutoff frequency of 63 Hz. The disagreement between the homogeneous half-space seabed model and the gradient seabed model are highest at frequencies below cutoff. This indicates that refraction due to a sound speed gradient in the seabed is likely responsible for the negative path losses observed in the data. Additionally, it also indicates that above the cutoff frequency these refracted arrivals do not play a significant role as the wave field is dominated by energy trapped in the waveguide. This is in agreement with the CW model results shown in Figure 6.1.

While the Silver Strand data discussed in the previous chapter are not the focus of this study, it is of interest to see whether the agreement between the measured data and half-space model results for the receiver-to-receiver path loss in Figure 5.28 can be improved using the depth dependent seabed model. For simplicity the geoacoustic model for the Virginia Beach environment is employed with two differences; c_o for Silver Strand in Eq. (2.20) is set to 1650 m/s (instead of 1590 m/s for Virginia Beach) corresponding to the lower limit of the estimated compressional sound speed (see Section 5.3), and the sound speed profile in the water column has a depth dependence following the experimental description in Chapter 2.These models are summarized in Table 6.1.

These results (Figure 6.4) are similar to the half-space model results (Figure 5.28) with reasonable agreement to the data above 40 Hz with differences typically less than 5 dB. Below 40 Hz, however the agreement is dramatically improved. Where the model results differed by up to 20 dB in the half-space seabed model, the differences are now less than 5 dB indicating the refraction effects likely contribute to the observed receiver-to-receiver path losses. The third-octave bands where these effects are observed in the Silver Strand data are likely lower than in the Virginia Beach data due to the deeper waveguide depth (22 m vs 16 m) and higher compressional sound speed in the seabed.

Table 6.1. Geoaoustic models for the three measurement sites. Below, *p* denotes the parameter associated with compressional waves and *s* detonates the parameters associated with the shear wave.

Measurement Site	**Layer**	**Thickness (m)**	**Density (kg/m³)**	**Sound Speed (m/s)**	**attenuation (dB\λ)**
Pu`uloa	water	10	1024	1537	-
	Sand	0.5	2000	p 1600 s 150	p 0.2 s 1.0
	Basement	∞	2192	p 2150 s 1075	p 0.1 s 0.2
Virginia Beach	Water	16	1024	1528	-
	Sand	∞	1900	c_o* 1590 β* 1.5 s^{-1} s Eq. (4.28)	p 0.2 s 1.0
Silver Strand	Water	22	1024	1493 - 1510	-
	Seabed	∞	1900	c_o* 1650 β* 1.5 s^{-1} s Eq. (4.28)	p 0.2 s 1.0

* co and β from Eq. (2.19)

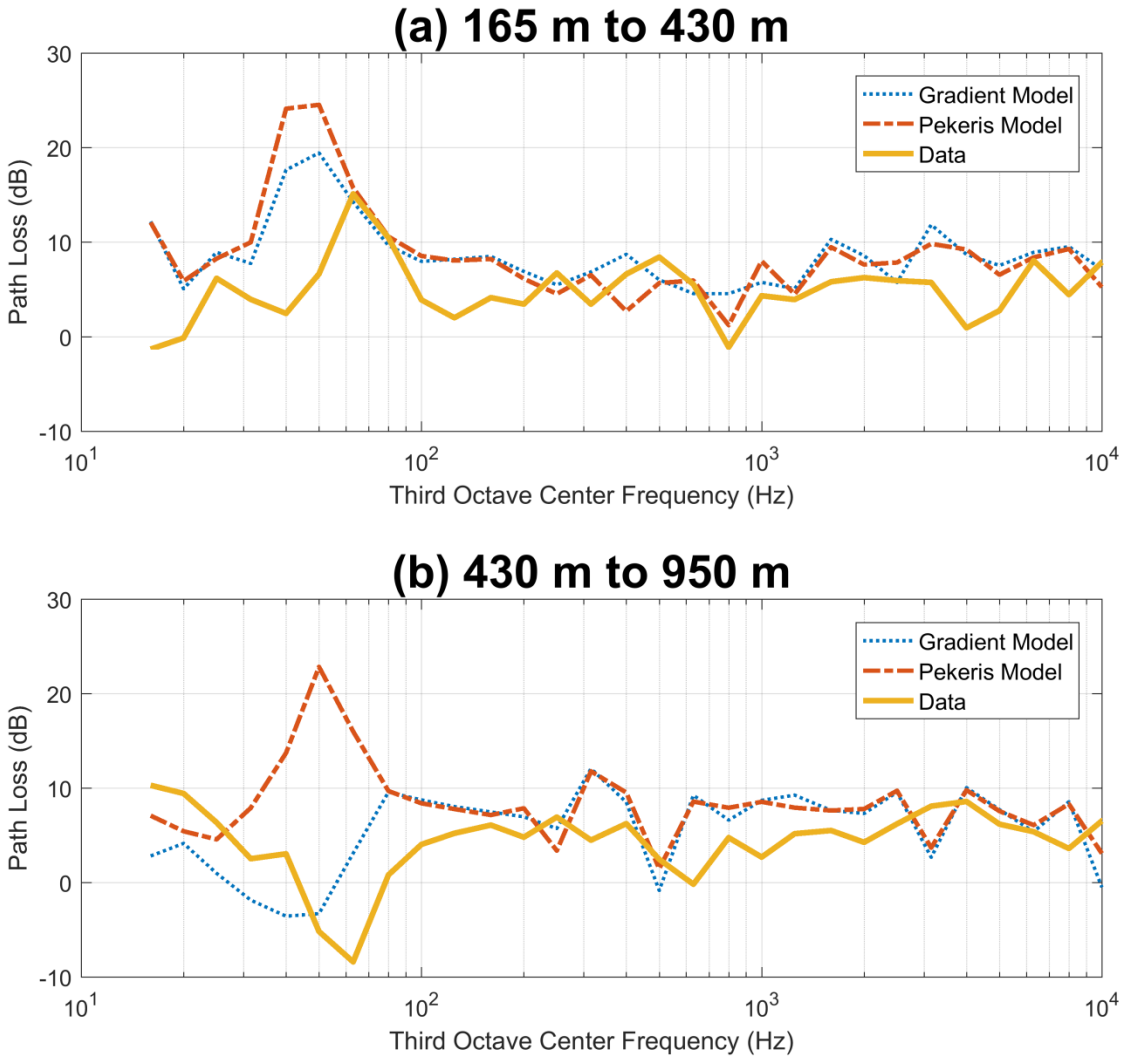

Figure 6.2. Measured path loss (yellow) compared to model results for a homogeneous half-space model (red) and a gradient seabed model with c_o in Eq. (2.20) of 1590 m/s (blue) for the (a) 165 m to 430 m range and (b) the 430 m to 950 m range.

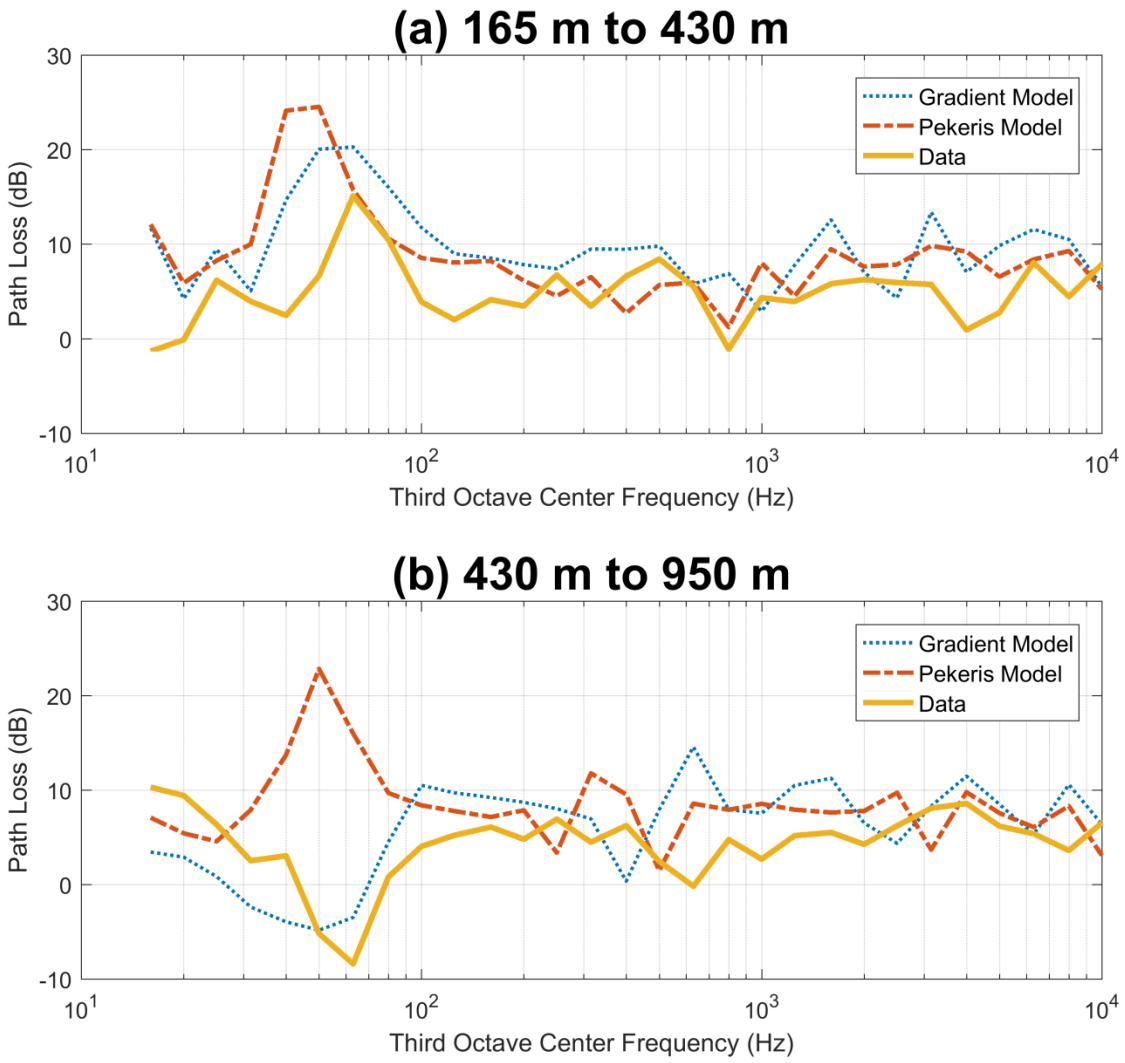

Figure 6.3. Measured path loss (yellow) compared to model results for a homogeneous half-space model (red) and a gradient seabed model with c_o in Eq. (2.20) of 1550 m/s (blue) for the (a) 165 m to 430 m range and (b) the 430 m to 950 m range.

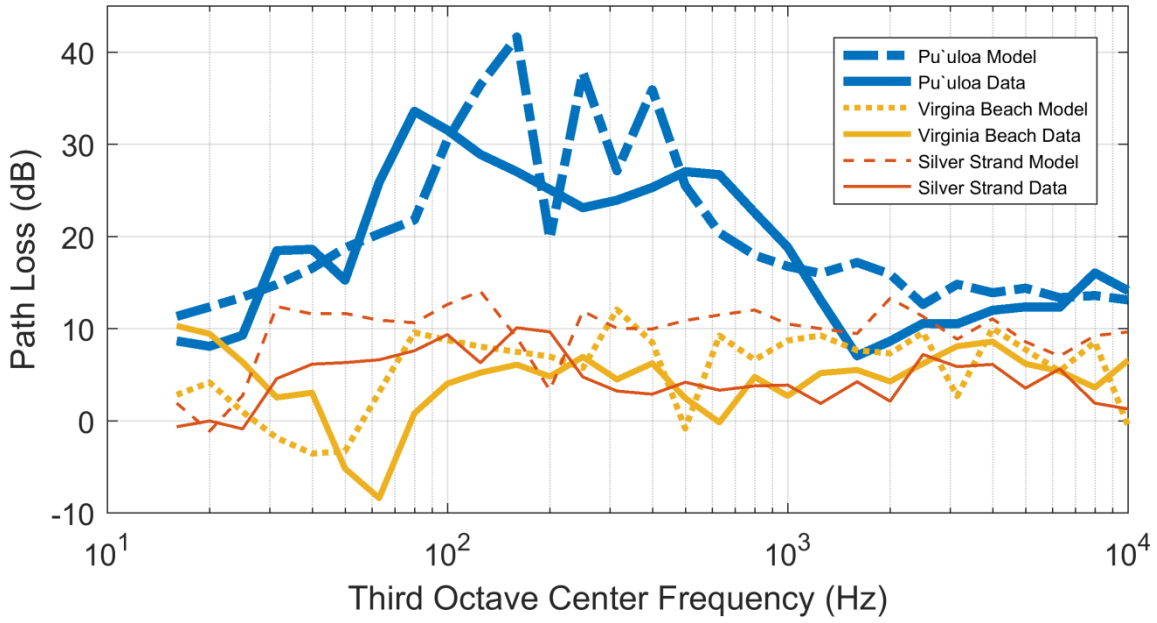

Figure 6.4. Comparison of the measured and modelled path loss for the Pu`uloa experiment compared to Virginia Beach and Silver Strand experiment model results. The Virginia Beach and Silver Strand model results employed a depth dependent sound speed profile in the seabed characterized by Eq. (2.20), whereas the Pu`uloa model results were computed using a thin (0.5 m) sand layer overlying a limestone half-space.

6.6 CONCLUSIONS

In this chapter the receiver-to-receiver path losses for the Virginia Beach experiment, presented in Chapter 5, were explored in greater depth; specifically, an unusual trend observed between the 40 and 100 Hz third-octave bands where path losses between the 430 m and 950 m receivers were found to have negative losses at 63 Hz indicating a large increase of energy with an increase in range. Modelled path losses using a Pekeris Waveguide seabed model were found to be in poor agreement with the measured data at these frequencies with a distinct positive peak within this frequency band.

It was hypothesized that these effects resulted from seabed refraction cause by an upward refracting, depth-dependent sound speed gradient in the seabed. A CW model for a range of frequencies and gradients, β, was used to determine (1) whether for typical values of β the range

at which refracted arrivals re-enter the waveguide are in the vicinity of the 950 m receiver (e.g. the 430 receiver is in the shadow zone and the 165 m receiver is in the near field) and (2) help determine whether there is a relation between the cutoff frequency in the waveguide and the frequencies where the negative path losses occur by comparing the frequencies where refraction effects are observed to the cutoff frequency in a Pekeris waveguide. Additionally, broadband path-losses for a Pekeris waveguide and for a gradient seabed model were compared to the measured data. The Pekeris model was found to be in poor agreement with the measured data between the 40 Hz and 100 Hz third-octave bands whereas the gradient seabed model predicted the negative losses observed in the data. Above the 100 Hz third-octave band, both models are in reasonable agreement with the data and each other.

Finally, these results were considered within the context of environmental noise predictions where simple propagation models are often used that only consider energy losses that increase with range; this results in a monotonic decrease of energy with increasing range. This work, however, showed that at some frequencies the sound field initially decreases with range and then increases due to refracted energy re-entering the waveguide. This increase in energy beyond a certain range can differ from levels predicted by simple range dependent loss model and Pekeris Waveguide models by up to 25 dB with levels measured on receivers at 900 m being similar to levels measured at 200 m.

Chapter 7. SUMMARY AND CONCLUSIONS

7.1 EXPERIMENT SUMMARY

Underwater explosives are regularly detonated on Navy ranges as part of training exercises. In order to comply with environmental regulations, the Navy must submit environmental impact assessments (EIA) every five years to outline their impact on the environment; this includes the impact of the noise levels produced during training where explosives are used. Few measurements of underwater explosions between 1 kg and 20 kg have been collected at short ranges (less than 2 km) where the sound levels are high enough to adversely impact marine animals [10], [18], [19]. To fill this gap, experiments were conducted at three training ranges to measure the noise levels produced by explosives; the U.S. Navy Pu`uloa Underwater Detonation Range, Pearl Harbor, HI, (Pu`uloa) at a training range 7 km off the coast of Virginia Beach, VA [19], [27] (Virginia Beach) and at the Silver Strand Training Complex, Naval Base Coronado, Coronado, CA (Silver Strand) [28]. All three of these experiments were conducted in shallow water (depth <25m) where sound propagation is heavily affected by interaction with the seabed.

7.2 PEAK PRESSURE AND SOUND EXPOSURE LEVEL

In Chapter 5 the peak pressure and SEL for the three experiments were compared (Figure 5.1 and Figure 5.2 respectively). This showed that the Pu`uloa data were always lower than both the Virginia Beach and Silver Strand data with the peak pressure 10 to 30 dB lower and the SEL being 15 to 30 dB lower. The differences in the peak pressure were particularly notable since the Virginia Beach data and Silver Strand data are in good agreement with empirical predictions given by Eq. (2.24). Comparing the measured peak pressures to Eq. (2.24) in Figure 5.1 showed that the Pu`uloa data did not agree with the empirical predictions.

7.3 ENERGY SPECTRAL DENSITY

In Chapter 5 the ESD from the three experiments were also presented (Figure 5.3). This showed the Pu`uloa ESD were significantly lower than the ESD from the other two experiments, with particularly poor agreement from 50 Hz to the 4000 Hz third-octave bands. These differences

were highest between the 50 and 1600 Hz third-octave bands with differences of up to 30 dB. Additionally, it was shown that for similar charge weights and measurement ranges, the 6.0 kg NEW charges from Virginia Beach and Silver strand are consistent for frequencies above 80 Hz with differences typically less than 5 dB. Looking at the Silver Strand ESD also shows that varying the receiver range results in differences of less than 5 dB at frequencies between 50 and 1600 Hz. The high losses in the Pu`uloa data were also observed in the VLA data collected along a separate transect. These results showed that differences in the ESD between the Pu`uloa data and the other two experiments were not entirely due to differences in the charge weight or measurement range, but was likely due to some other effect. This motivated a receiver-to-receiver path loss study which explored the impact of the seabed on propagation independent of the source.

7.4 RECEIVER-TO-RECEIVER PATH LOSS

While the measured peak pressure and SEL from the explosion measurements can be useful for those crafting EIAs for underwater noise, it is important to understand why the levels from the Pu`uloa site are so much lower than the other two. Spectrograms of the measured data (Figure 5.4 through Figure 5.11) also showed that the Pu'uloa data (Figure 5.10 and Figure 5.11) exhibited an additional feature in the data (possibly cavitation effects) that are not present in the other time series form Virginia Beach and Silver Strand. This further motivated studying the receiver-to-receiver path loss in Chapter 5 in which propagation can be considered independent of the source as demonstrated in Eq. (5.32). Comparing the measured receiver-to-receiver path losses (Figure 5.28) showed that above 1600 Hz the three data sets are in reasonable agreement varying by less than 10 dB whereas between 50 Hz and 1600 Hz the Pu`uloa path losses are up to 30 dB higher than those measured at the other two sites. This was similar to the results observed in the ESD comparison in Figure 5.3.

Predictions of the path losses were computed by modelling the Pu`uloa seabed as a thin elastic sand layer over an elastic half-space and the other two sites as Pekeris waveguide with sandy half-space bottoms. These goacoustic models were based on previous seabed studies and observation made by the Navy divers assisting with the experiments Results of this analysis

showed very good agreement between measured and modelled data at third-octave bands above 100 Hz. The poor agreement in the Virginia Beach data below the 100 Hz third-octave bands was considered as part of Chapter 6.

To ensure the physics involved in the high losses in the Pu`uloa data were understood, an analytical reflection loss model from Chapman and Chapman [63] was used to model a fully fluid seabed and an elastic seabed. This showed that the high losses at the measurement site were likely due to the conversion of compressional to shear waves through two mechanisms; shear resonance effects in the thin sand layer and the excitation of Stoneley waves at the sediment-basement interface (as described by Hughes et al. [61] and Hovem and Kristensen [62] respectively).

Other potential loss mechanisms were also considered including bathymetric refraction and losses from scattering due to a rough sea surface. Bathymetric refraction was ruled out as the slope of the seabed perpendicular to the source receiver transect was not steep enough to cause significant refraction effects (approximately 0.5^{o}). Losses due to surface roughness were also ruled out as they would increase with increasing frequency, whereas the losses in the Pu`uloa data occurred between 50 Hz and 1600 Hz third-octave bands and are not observed at higher frequencies.

7.5 NEGATIVE PATH LOSSES AND SEABED REFRACTION

Predicted path losses for both the Virginia Beach data are in reasonable agreement with the measured data above the 100 Hz third-octave band however there is poor agreement at lower frequencies. Of particular interest are unusual trends observed in the path loss between the 430 m and 950 m measurement ranges where negative losses are observed at 63 Hz (Figure 5.25). Although modelling the Virginia Beach measurement site as a Pekeris Waveguide gives reasonable agreement above 100 Hz, it was established in Chapter 4 that the seabed has depth dependent properties. This indicated that these features could be a result of seabed refraction

caused by a compressional sound speed gradient in the seabed that increases with depth according to a linear sound speed profile described in Eq. (2.20).

By looking at a CW model for frequencies between 40 Hz and 100 Hz and a range of values of the gradient β it was shown that, when β is close to 1.5 s^{-1}, the 430 m receiver could be located within a shadow zone and energy travelling in the seabed could re-enter the waveguide at the 950 m range creating a lit zone. This trend was confirmed by comparing receiver-to-receiver path loss predictions for a Pekeris waveguide and the linear gradient seabed to the measured data (Figure 6.2). This showed that both models gave similar results above 100 Hz third-octave bands; however, the linear sound speed gradient model was in much better agreement with the measurements at third-octave bands below 100 Hz. Similar to Virginia Beach, the Silver Strand receiver-to-receiver path loss was recalculated using a linear gradient seabed model and showed improved agreement below 40 Hz (Figure 6.4) compared to the Pekeris environment model (Figure 5.28).

7.6 CONCLUSIONS

While predictive models can be a useful tool in planning, they require validation to ensure their accuracy. This is accomplished through acoustic monitoring of noise generating activities to obtain ground truth data on the resulting noise levels. Using these measurements, parameters in the predictive model can be optimized to give more accurate predictions and provide a better understanding of the mechanisms that contribute to the propagation loss.

These validation measurements are not only valuable for benchmarking specific EIA studies. They can also be used more broadly to inform the initial stages of future EIAs. By using data from a measurement environment with similar characteristics, appropriate propagation models can be selected and benchmarked. It is important, however, that the characteristics of the measurement environment are taken into account to ensure levels are not over or under predicted by selecting an inappropriate seabed model. It is therefore important for the measured data to be defined within the context of the measurement site to ensure others using the experimental validation apply it to appropriate scenarios.

Having reviewed the results of this work, the goals are revisited;

a) Present the measurements of small underwater explosions (charges weighing between 0.5 kg and 20 kg) with an emphasis on the metrics commonly used to describe environmental noise including the peak pressure and the sound exposure level.
b) Understand why received levels at the Pu`uloa measurement site are so much lower than at the other two sites.
c) Provide context about the measurement environments so that these data can be more effectively utilized by both researchers and policy makers for studying environmental noise and in the development of mitigation measures to protect marine life from harmful noise levels.

Goal a) was achieved through the presentation of the measured peak pressures and sound exposure levels. Through goal b), it has been shown that the high losses in the Pu`uloa data are most likely a result of losses resulting from the conversion of compressional waves into shear waves in the seabed. The high losses between 40 Hz and 1600 Hz occur as the seabed is composed of a thin elastic sand layer is overlying an elastic half-space. Without the thin sand layer, the high losses would extend beyond 1600 Hz whereas if the sand layer was relatively thick (thickness of sand layer much greater than the wavelength of incident sound) then the results would be similar to those from a sand half-space.

Goals a) and b) provide the foundation for achieving goal c), providing context for these measurements; the primary focus of this work. Comparing the peak pressure and SEL from the Virginia Beach and Silver Strand measurement sites shows similar results. This is understandable given the seabed at both sites is characterized by sandy sediments. This demonstrates that these data could be used as a guide for future EIAs for sites with similar characteristics and seabed composition. In fact, the Virginia Beach data were successfully used in the Silver Strand experiment to inform equipment settings and measurement locations. This ensured the signal did not saturate the equipment nor lead to a low signal-to-noise ratio. Using these data as references in the Pu`uloa experiment, however, led to significant overestimates of the noise levels. Based on these estimates, the equipment setting were selected which led to a

low signal-to-noise ratio discussed in Chapter 5 (Figure 5.27). Conversely if the Pu1uloa data were used to inform an EIA or validation experiment at a sandy site, the noise levels would be underestimated and the equipment settings would be too low leading to signal saturation. This demonstrates not only the utility of these data but also the limitation on their use; it is important to use the correct tool for the job at hand.

As demonstrated in this work, the seabed has a considerable impact on the environmental noise levels, but an exact reproduction of the seabed is impossible. It is therefore up to the modeler to decide how detailed the seabed model should be. For Virginia Beach receiver-to-receiver path loss prediction, a Pekeris environment model was compared to a seabed characterized by a linear sound speed gradient (Figure 6.2). While only the gradient seabed model is in good agreement with both the 165 m to 430 m and 430 m to 950 m path losses below 80 Hz, both models are in reasonable agreement with measured data at higher frequencies. For all three experiments considered in this work, a 500 m zone of influence was used. As discussed in Chapter 6, the refracted energy re-enters the waveguide beyond this range (roughly 950 m). This means marine animals with hearing sensitivity in the 40 Hz to 100 Hz range could potentially experience significantly higher noise levels than expected if EIA noise predictions were computed with a Pekeris waveguide model. While it is not the goal of this work to provide recommendations on what to do with this information, this topic should at the very least be recognized and considered so an informed decision can be reached.

7.7 RECOMMENDATIONS AND FUTURE WORK

This work was completed in hopes of it serving as a useful tool for future validation experiments and EIAs for underwater explosion events. In this section several recommendations and lessons learned are be shared along with avenues for future work.

The first set of recommendations is focused on metadata used in the predictive modelling. The collection of metadata for the water column is relatively straightforward compared to the seabed. It involves using echo sounders to determine water depths and CTD sensors to measure the water sound speed. Having shown the importance of the seabed in this work, the primary

recommendation of this research is the importance of detailed seabed characterization. This is not only invaluable for post-experiment analysis, but also provided ground truth data on the seabed. One of the biggest weaknesses of this work is the lack of ground truth data against which the proposed geoacoustic models can be benchmarked. While this could include detailed coring, even simple side scan sonar imaging would provide valuable information on layering within the seabed (as in the Pu`uloa experiment site) or the absence of such features (as in the other two experiment sites). With limited funding, however, a seabed study may not be feasible due to the costs. As an alternative, for areas with recreational beaches or heavy shipping traffic, previous seabed studies may have been conducted (as was the case for the studies in this work). While these are not always available, they can provide valuable insight into the general seabed composition in an area.

There are still several areas that would greatly benefit from additional research. Earlier, a spectrogram of the Pu`uloa data was presented (Figure 5.10 and Figure 5.11) which show possible cavitation effects. A study by Cui et. al. [68] that explored high speed imaging of small explosions detonated close to surfaces (rigid and pressure release) demonstrates the complex effects that the proximity to surfaces can have on the bubble pulse. As demonstrated by Von Benda Beckman et. al. [10], the Chapman source model [16], [17] does not accurately predict noise levels at high frequencies (kHz range) so they provide a source model modified using the data. However, this does not give any insight into the physics involved and could easily be misused if applied to other environments or detonation depths that do not put the source in close proximity to a surface (sea surface or water-seabed interface). Therefore, additional work to model the source waveform of underwater explosions near surfaces would be a valuable contribution.

Another research avenue is the development of a robust, range dependent, 3D elastic propagation model that can be used for broadband noise prediction. In this work, such a code would be very useful for modelling the Pu`uloa data collected at the offshore receiver on the vertical line array. As of now however, the publicly available version of OASES cannot model range dependent propagation. One promising model is the SPECFEM spectral finite element model (https://geodynamics.org/cig/software/specfem3d/). While capable of modelling elastic wave

propagation in range dependent environments, it still needs additional work before it can be used to model broadband noise in shallow water. In general, with the increasing availability of computational resources such as cloud services, the use of finite element models may become a more viable approach as they can utilize parallel computing technologies.

While the data presented here serve as a useful tool, the community would benefit from additional data sets of underwater explosion measurements. The data in this work were typically collected over the course of a few days, so it is unclear how the noise levels would be affected by seasonal variation or even daily fluctuations due to changing weather patterns. This work has also shown how noise levels can vary site-to-site, but it would be valuable to study the noise levels at sites with a variety of seabeds outside of the two studied in this work (sandy sediments and the thin sand layer over limestone).

This work has focused on the physics and technical aspects associated with underwater noise, but the end goal of doing this work is the protection of marine animals that rely on hearing and sonar for their survival. Unfortunately, physics alone cannot achieve this. Numerous other individuals with a range of skill sets are also essential, including navy divers, marine biologists, regulators, and politicians. Understandably, these individuals often do not have the technical background to fully absorb all of the detailed technical information involved in underwater noise prediction; it is also unrealistic to expect all of them to become experts on underwater noise. It is therefore imperative that the results of underwater noise studies be presented in ways that are meaningful to a wide array of professionals with diverse background. At the end of the day, even the best science is useless unless it can be understood by those who need it.

BIBLIOGRAPHY

[1] L. J. May-Collado and S. G. Quiñones-Lebrón, "Dolphin changes in whistle structure with watercraft activity depends on their behavioral state," *J. Acoust. Soc. Am.*, vol. 135, no. 4, pp. EL193–EL198, Apr. 2014.

[2] P. J. O. Miller *et al.*, "Dose-response relationships for the onset of avoidance of sonar by free-ranging killer whales," *J. Acoust. Soc. Am.*, vol. 135, no. 2, pp. 975–993, Feb. 2014.

[3] R. A. Kastelein, L. Hoek, R. Gransier, M. Rambags, and N. Claeys, "Effect of level, duration, and inter-pulse interval of 1–2 kHz sonar signal exposures on harbor porpoise hearing," *J. Acoust. Soc. Am.*, vol. 136, no. 1, pp. 412–422, Jul. 2014.

[4] J. J. Govoni, M. A. West, L. R. Settle, R. T. Lynch, and M. D. Greene, "Effects of underwater explosions on larval fish: Implications for a coastal engineering project," *J. Coast. Res.*, vol. 24, no. 2B, pp. 228–233, Mar. 2008.

[5] N. O. Handegard, T. V. Tronstad, and J. M. Hovem, "Evaluating the effect of seismic surveys on fish — the efficacy of different exposure metrics to explain disturbance," *Can. J. Fish. Aquat. Sci.*, vol. 70, no. 9, pp. 1271–1277, Jun. 2013.

[6] K. C. Buckstaff, R. S. Wells, J. G. Gannon, and D. P. Nowacek, "Responses of Bottlenose Dolphins (Tursiops truncatus) to Construction and Demolition of Coastal Marine Structures," *Aquat. Mamm.*, vol. 39, no. 2, pp. 174–186, 2013.

[7] S. T. Viada *et al.*, "Review of potential impacts to sea turtles from underwater explosive removal of offshore structures," *Environ. Impact Assess. Rev.*, vol. 28, no. 4–5, pp. 267–285, May 2008.

[8] K. A. Cunningham and D. C. Mountain, "Simulated masking of right whale sounds by shipping noise: Incorporating a model of the auditory periphery," *J. Acoust. Soc. Am.*, vol. 135, no. 3, pp. 1632–1640, Mar. 2014.

[9] J. Tougaard, O. D. Henriksen, and L. A. Miller, "Underwater noise from three types of offshore wind turbines: Estimation of impact zones for harbor porpoises and harbor seals," *J. Acoust. Soc. Am.*, vol. 125, no. 6, pp. 3766–3773, Jun. 2009.

[10] A. M. von Benda-Beckmann *et al.*, "Assessing the Impact of Underwater Clearance of Unexploded Ordnance on Harbour Porpoises (Phocoena phocoena) in the Southern North Sea," *Aquat. Mamm. Moline*, vol. 41, no. 4, pp. 503–523, 2015.

[11] D. Kastak, B. L. Southall, R. J. Schusterman, and C. R. Kastak, "Underwater temporary threshold shift in pinnipeds: Effects of noise level and duration," *J. Acoust. Soc. Am.*, vol. 118, no. 5, pp. 3154–3163, Nov. 2005.

[12] J. J. Finneran, "Noise-induced hearing loss in marine mammals: A review of temporary threshold shift studies from 1996 to 2015," *J. Acoust. Soc. Am.*, vol. 138, no. 3, pp. 1702–1726, Sep. 2015.

[13] B. L. Southall *et al.*, "Marine Mammal Noise Special Issue: Exposure Criteria: Initial Scientific Recommendations," *Aquat. Mamm.*, vol. 33, no. 4, pp. 411–522, Dec. 2007.

[14] J. Lamar (John Lamar) Worzel, *Propagation of sound in the ocean. Explosion sounds in shallow water,*. New York]: Geological Society of America, 1948.

[15] D. E. Weston, "Underwater Explosions as Acoustic Sources," *Proc. Phys. Soc.*, vol. 76, no. 2, p. 233, Aug. 1960.

[16] N. R. Chapman, "Measurement of the waveform parameters of shallow explosive charges," *J. Acoust. Soc. Am.*, vol. 78, no. 2, pp. 672–681, Aug. 1985.

[17] N. R. Chapman, “Source levels of shallow explosive charges,” *J. Acoust. Soc. Am.*, vol. 84, no. 2, pp. 697–702, 1988.
[18] M. E. dos Santos, M. N. Couchinho, A. R. Luis, and E. J. Goncalves, “Monitoring underwater explosions in the habitat of resident bottlenose dolphins,” *J. Acoust. Soc. Am.*, vol. 128, no. 6, pp. 3805–3808, 2010.
[19] A. G. Soloway and P. H. Dahl, “Peak sound pressure and sound exposure level from underwater explosions in shallow water,” *J. Acoust. Soc. Am.*, vol. 136, no. 3, pp. EL218–EL223, Sep. 2014.
[20] A. B. Arons, “Underwater Explosion Shock Wave Parameters at Large Distances from the Charge,” *J. Acoust. Soc. Am.*, vol. 26, no. 3, pp. 343–346, 1954.
[21] M. Blaik and E. A. Christian, “Near-Surface Measurements of Deep Explosions I. Pressure Pulses from Small Charges,” *J. Acoust. Soc. Am.*, vol. 38, no. 1, pp. 50–56, 1965.
[22] E. A. Christian and M. Blaik, “Near-Surface Measurements of Deep Explosions II. Energy Spectra of Small Charges,” *J. Acoust. Soc. Am.*, vol. 38, no. 1, pp. 57–62, 1965.
[23] J. B. Gaspin and V. K. Shuler, “Source Levels of Shallow Underwater Explosions,” Naval Ordnance Laborary, White Oaks, Silver Spring, Maryland, NOLTR 71-160, Oct. 1971.
[24] A. C. Kibblewhite and R. N. Denham, “Measurements of Acoustic Energy from Underwater Explosions,” *J. Acoust. Soc. Am.*, vol. 48, no. 1B, pp. 346–351, 1970.
[25] J. B. Gaspin, J. A. Goertner, and I. M. Blatstein, “The determination of acoustic source levels for shallow underwater explosions,” *J. Acoust. Soc. Am.*, vol. 66, no. 5, pp. 1453–1462, 1979.
[26] R. H. Cole, *Underwater explosions*. Princeton: Princeton Univ. Press, 1948.
[27] A. G. Soloway and P. H. Dahl, “Mine Neutralization Exercise (MINEX) Sound Measurement Trial,” Naval Facilities Engineering Command (NAVFAC) Atlantic, Norfolk, Virginia, under Contract No. N62470-10-3011, Task Order CTO 03, issued to HDR Inc., 2014a.
[28] A. G. Soloway and P. H. Dahl, “Noise Source Level and Propagation Measurement of Underwater Detonation Training at the Silver Strand Training Complex, Naval Base Coronado, Coronado, CA,” Prepared for Commander, U.S. Pacific Fleet. Submitted to Naval Facilities Engineering Command, Naval Base Coronado, Coronado, CA, 2015.
[29] Henrik Schmidt, *Ocean Acoustics and Seismic Exploration Synthesis (OASES)*. Department of Ocean Engineering Massachusettes Institute of Technology, 2012.
[30] A. Farcas, P. M. Thompson, and N. D. Merchant, “Underwater noise modelling for environmental impact assessment,” *Environ. Impact Assess. Rev.*, vol. 57, pp. 114–122, Feb. 2016.
[31] D. E. Weston, “Intensity-range relations in oceanographic acoustics,” *J. Sound Vib.*, vol. 18, no. 2, pp. 271–287, Sep. 1971.
[32] Ainslie, M.A., Dahl, P.H., Jong, C.A.F. de, and Laws, R.M., “Practical spreading laws: The snakes and ladders of shallow water acoustics,” in *Proc. 2nd Int. Conf. Exhibit. Underwater Acoust*, 2014.
[33] L. M. Brekhovskikh, *Waves in layered media*, 2d ed. New York: Academic Press, 1980.
[34] T. Lippert and O. von Estorff, “The significance of parameter uncertainties for the prediction of offshore pile driving noise,” *J. Acoust. Soc. Am.*, vol. 136, no. 5, pp. 2463–2471, Nov. 2014.
[35] P. H. Dahl, D. R. Dall’Osto, and D. M. Farrell, “The underwater sound field from vibratory pile driving,” *J. Acoust. Soc. Am.*, vol. 137, no. 6, pp. 3544–3554, Jun. 2015.

[36] J.-X. Zhou, X.-Z. Zhang, and D. P. Knobles, “Low-frequency geoacoustic model for the effective properties of sandy seabottoms,” *J. Acoust. Soc. Am.*, vol. 125, no. 5, pp. 2847–2866, May 2009.
[37] J.-X. Zhou and X.-Z. Zhang, “Shear wave velocity and attenuation in the upper layer of ocean bottoms from long-range acoustic field measurements,” *J. Acoust. Soc. Am.*, vol. 132, no. 6, pp. 3698–3705, Dec. 2012.
[38] J. Worzel, C. Pekeris, and M. Ewing, *Propagation of sound in the ocean. Explosion sounds in shallow water*. New York: Geological Society of America, 1948.
[39] F. Press and M. Ewing, “Propagation of explosive sound in a liquid layer overlying a semi-infinite elastic solid,” *Geophysics*, vol. 15, no. 3, pp. 426–446, Jul. 1950.
[40] W. M. Ewing, *Elastic waves in layered media*. New York,: McGraw-Hill, 1957.
[41] Clarence S. Clay and Herman Medwin, *Acoustical oceanography: principles and applications*. New York: Wiley, 1977.
[42] K. Aki and P. G. Richards, *Quantitative seismology*. Sausalito, Calif.: University Science Books, 2002.
[43] D. Rauch, “Seismic Interface Waves in Coastal Waters: A Review,” SACLANTCEN, La-Spezia, Italy, SR-42, Nov. 1980.
[44] F. Gassmann, “Elastic waves through a packing of spheres,” *Geophysics*, vol. 16, no. 4, pp. 673–685, Oct. 1951.
[45] O. A. Godin and D. M. Chapman, “Dispersion of interface waves in sediments with power-law shear speed profiles. I. Exact and approximate analytical results,” *J. Acoust. Soc. Am.*, vol. 110, no. 4, pp. 1890–1907, Oct. 2001.
[46] A. D. Pierce and W. M. Carey, “Shear wave speed increases with depth to the one-sixth power in sandy-silty marine sediments,” *Proc. Meet. Acoust.*, vol. 4, no. 1, p. 070006, Jul. 2008.
[47] D. R. Jackson and M. D. Richardson, *High-frequency seafloor acoustics*. New York: Springer, 2007.
[48] E. L. Hamilton, “Shear-wave velocity versus depth in marine sediments; a review,” *Geophysics*, vol. 41, no. 5, pp. 985–996, Oct. 1976.
[49] E. L. Hamilton, “Geoacoustic modeling of the sea floor,” *J. Acoust. Soc. Am.*, vol. 68, no. 5, pp. 1313–1340, Nov. 1980.
[50] D. M. F. Chapman and O. A. Godin, “Dispersion of interface waves in sediments with power-law shear speed profiles. II. Experimental observations and seismo-acoustic inversions,” *J. Acoust. Soc. Am.*, vol. 110, no. 4, pp. 1908–1916, 2001.
[51] E. L. Hamilton, “Sound velocity as a function of depth in marine sediments,” *J. Acoust. Soc. Am.*, vol. 78, no. 4, pp. 1348–1355, Oct. 1985.
[52] D. A. Sachs and A. Silbiger, “Focusing and Refraction of Harmonic Sound and Transient Pulses in Stratified Media,” *J. Acoust. Soc. Am.*, vol. 49, no. 3B, pp. 824–840, Mar. 1971.
[53] G. V. Frisk, “Determination of Sediment Sound Speed Profiles Using Caustic Range Information,” in *Bottom-Interacting Ocean Acoustics*, Springer, Boston, MA, 1980, pp. 153–157.
[54] J. S. Hanna, “Short-range transmission loss and the evidence for bottom-refracted energy,” *J. Acoust. Soc. Am.*, vol. 53, no. 6, pp. 1686–1690, Jun. 1973.
[55] R. E. Christensen, J. A. Frank, and W. H. Geddes, “Low-frequency propagation via shallow refracted paths through deep ocean unconsolidated sediments,” *J. Acoust. Soc. Am.*, vol. 57, no. 6, pp. 1421–1426, Jun. 1975.

[56] D. C. Stickler, “Negative bottom loss, critical-angle shift, and the interpretation of the bottom reflection coefficient,” *J. Acoust. Soc. Am.*, vol. 61, no. 3, pp. 707–710, Mar. 1977.
[57] F. B. Jensen, W. A. Kuperman, M. B. Porter, and H. Schmidt, *Computational Ocean Acoustics*. Springer Science & Business Media, 2011.
[58] K. E. Hawker, “The existence of Stoneley waves as a loss mechanism in plane wave reflection problems,” *J. Acoust. Soc. Am.*, vol. 65, no. 3, pp. 682–686, 1979.
[59] K. E. Hawker, “Influence of Stoneley waves on plane-wave reflection coefficients: Characteristics of bottom reflection loss,” *J. Acoust. Soc. Am.*, vol. 64, no. 2, pp. 548–555, 1978.
[60] P. J. Vidmar, “Ray path analysis of sediment shear wave effects on bottom reflection loss,” *J. Acoust. Soc. Am.*, vol. 68, no. 2, pp. 639–648, Aug. 1980.
[61] S. J. Hughes, D. D. Ellis, D. M. F. Chapman, and P. R. Staal, “Low-frequency acoustic propagation loss in shallow water over hard-rock seabeds covered by a thin layer of elastic–solid sediment,” *J. Acoust. Soc. Am.*, vol. 88, no. 1, pp. 283–297, Jul. 1990.
[62] J. M. Hovem and Å. Kristensen, “Reflection loss at a bottom with a fluid sediment layer over a hard solid half-space,” *J. Acoust. Soc. Am.*, vol. 92, no. 1, pp. 335–340, Jul. 1992.
[63] N. R. Chapman and D. M. F. Chapman, “A coherent ray model of plane-wave reflection from a thin sediment layer,” *J. Acoust. Soc. Am.*, vol. 94, no. 5, pp. 2731–2738, Nov. 1993.
[64] S. Ivansson, “Shear-wave induced transmission loss in a fluid–solid medium,” *J. Acoust. Soc. Am.*, vol. 96, no. 5, pp. 2870–2875, Nov. 1994.
[65] P. J. Vidmar and T. L. Foreman, “A plane-wave reflection loss model including sediment rigidity,” *J. Acoust. Soc. Am.*, vol. 66, no. 6, pp. 1830–1835, Dec. 1979.
[66] C. A. Clark, “Wave Propagation Prediction Over a Thin Elastic Sediment and Rock Basement,” *IEEE J. Ocean. Eng.*, vol. 37, no. 3, pp. 494–506, Jul. 2012.
[67] M. A. Ainslie, “Plane-wave reflection and transmission coefficients for a three-layered elastic medium,” *J. Acoust. Soc. Am.*, vol. 97, no. 2, pp. 954–961, Feb. 1995.
[68] P. Cui, A. M. Zhang, and S. P. Wang, “Small-charge underwater explosion bubble experiments under various boundary conditions,” *Phys. Fluids*, vol. 28, no. 11, p. 117103, Nov. 2016.
[69] J. F. Slifko, “Pressure-Pulse Characteristics of Deep Explosions as Functions of Depth and Range,” United States Naval Ordnance Laboratory, NOLTR 67-87, 1967.
[70] J. G. Kirkwood and W. W. Wood, *Shock and detonation waves*. New York: Gordon and Breach, 1968.
[71] J. Wakeley, “Pressure-signature model for an underwater explosive charge,” *U.S. Navy journal of Underwater Acoustics*, vol. 27, no. 2, pp. 445–449, 1977.
[72] K. Murata, K. Takahashi, and Y. Kato, “Measurements of Underwater Explosion Performances by Pressure Guage Using Fluoropolymer,” *J. Mater. Process. Technol.*, vol. 85, no. 1–3, pp. 0924–0136, 2002.
[73] M. E. dos Santos, M. N. Couchinho, A. R. Luis, and E. J. Goncalves, “Monitoring underwater explosions in the habitat of resident bottlenose dolphins,” *J. Acoust. Soc. Am.*, vol. 128, no. 6, pp. 3805–3808, 2010.
[74] S. Temkin, “A Review of the Propagation of Pressure Pulses Produced by Small Underwater Explosive Charges.,” Rutgers University, New Brunswick, NJ, Memorandum NRL-MR-6181, 1988.
[75] A. N. Popper and M. C. Hastings, “The effects of anthropogenic sources of sound on fishes,” *J. Fish Biol.*, vol. 75, no. 3, pp. 455–489, Aug. 2009.

[76] B. L. Southall *et al.*, "Marine mammal noise exposure criteria: Initial scientific recommendations.," *J. Acoust. Soc. Am.*, vol. 125, no. 4, pp. 2517–2517, Apr. 2009.
[77] E. E. Grossman, W. A. Barnhardt, P. Hart, B. M. Richmond, and M. E. Field, "Shelf stratigraphy and the influence of antecedent substrate on Holocene reef development, south Oahu, Hawaii," *Mar. Geol.*, vol. 226, no. 1–2, p. 18, 2006.
[78] S. S. Fu, C. Tao, M. Prasad, R. H. Wilkens, and L. N. Frazer, "Acoustic properties of coral sands, Waikiki, Hawaii," *J. Acoust. Soc. Am.*, vol. 115, no. 5, pp. 2013–2020, May 2004.
[79] P. H. Dahl, L. H. Shannon, A. Soloway, D. R. Dall'Osto, and D. Farrell, "Analysis and Modeling of Acoustic and environmental Measurements, from Underwater Detonation Training Events on the Pu`uloa Underwater Detonation Range, O`ahu, Hawai`i," Applied Physics Laboratory, University of Washington, Seattle, WA, 2016.
[80] C.S. Hardaway, C.H. Hobbs III, and D.A. Milligan, "Investigations of Offshore Beach Sands: Virginia Beach and Sandbridge, Virginia," Virginia Institute of Marine Science, College of William and Mary, Gloucester Point, Virginia, Oct. 1995.
[81] A. G. Soloway, P. H. Dahl, and R. I. Odom, "Modeling explosion generated Scholte waves in sandy sediments with power law dependent shear wave speed," *J. Acoust. Soc. Am.*, vol. 138, no. 4, pp. EL370–EL374, Oct. 2015.
[82] J. Ewing, J. A. Carter, G. H. Sutton, and N. Barstow, "Shallow water sediment properties derived from high-frequency shear and interface waves," *J. Geophys. Res. Solid Earth*, vol. 97, no. B4, pp. 4739–4762, 1992.
[83] G. Nolet and L. M. Dorman, "Waveform Analysis of Scholte Modes In Ocean Sediment Layers," *Geophys. J. Int.*, vol. 125, no. 2, pp. 385–396, 1996.
[84] J. A. Collins, G. H. Sutton, and J. I. Ewing, "Shear-wave velocity structure of shallow-water sediments in the East China Sea," *J. Acoust. Soc. Am.*, vol. 100, no. 6, pp. 3646–3654, 1996.
[85] P. Bergamo, L. Bodet, L. V. Socco, R. Mourgues, and V. Tournat, "Physical modelling of a surface-wave survey over a laterally varying granular medium with property contrasts and velocity gradients," *Geophys. J. Int.*, vol. 197, no. 1, pp. 233–247, Apr. 2014.
[86] K. Ohta, S. Matsumoto, K. Okabe, K. Asano, and Y. Kanamori, "Estimation of Shear Wave Speed in Ocean-Bottom Sediment Using Electromagnetic Induction Source," *IEEE J. Ocean. Eng.*, vol. 33, no. 3, pp. 233–239, Jul. 2008.
[87] A. Duncan, A. Gavrilov, and F. Li, "Acoustic propagation over limestone seabeds," in *Acoustics 2009, Annual Conference of the Australian Acoustical Society*, Adelaide, South Australia, 2009.
[88] P. T. Madsen, M. Johnson, P. J. O. Miller, N. A. Soto, J. Lynch, and P. Tyack, "Quantitative measures of air-gun pulses recorded on sperm whales (Physeter macrocephalus) using acoustic tags during controlled exposure experiments," *J. Acoust. Soc. Am.*, vol. 120, no. 4, pp. 2366–2379, 2006.
[89] E. L. Hamilton, "Vp/Vs and Poisson's ratios in marine sediments and rocks," *J. Acoust. Soc. Am.*, vol. 66, no. 4, pp. 1093–1101, Oct. 1979.
[90] E. L. Hamilton, "Sound velocity–density relations in sea-floor sediments and rocks," *J. Acoust. Soc. Am.*, vol. 63, no. 2, pp. 366–377, Feb. 1978.
[91] E. L. Hamilton, "Sound velocity gradients in marine sediments," *J. Acoust. Soc. Am.*, vol. 65, no. 4, pp. 909–922, Apr. 1979.

[92] O. A. Godin and D. M. F. Chapman, “Dispersion of interface waves in sediments with power-law shear speed profiles. I. Exact and approximate analytical results,” *J. Acoust. Soc. Am.*, vol. 110, no. 4, pp. 1890–1907, 2001.
[93] A. G. Soloway and P. H. Dahl, “Measurements of the peak pressure and sound exposure level from underwater explosions,” *J. Acoust. Soc. Am.*, vol. 134, no. 5, pp. 4116–4116, Nov. 2013.
[94] C.H. Hobbs III, “Investigations of isolated sand shoals and associated deposits Virginia inner shelf,” Virginia Institute of Marine Science, College of William and Mary, Gloucester Point, Virginia, Final Contract Report, Mar. 1996.
[95] S. M. Kimball and J. K. Dame, “Geotechnical evaluation of sand resources on the inner shelf of southern Virginia: Report & Appendices A-B,” College of William and Mary School of Marine Science, Virginia Institute of Marine Science, Virginia Beach, Virginia, Final Report, Aug. 1989.
[96] C. Hobbs III, “Sediments and shallow stratigraphy of a portion of the continental shelf of southeastern Virginia,” Virginia Institute of Marine Science, College of William and Mary, Gloucester Point, Virginia, 1997.

APPENDIX A: VIRGINIA BEACH MEASUREMENTS

A.1) Measurement Site

This section originally appeared in the report by Soloway and Dahl [93]. It has been included in this work for completeness.

The underwater explosion measurements were conducted on 11 September, 2012 at a site located approximately 7 km off the coast of Virginia Beach, Virginia. The measurement site encompasses four locations; the navy detonation site, and the mooring locations of the two measurement vessels involved, as discussed below, one of which was placed in two mooring positions over the course of the day (Figure A.2). For purposes of this report, this area can be considered a rectangular of dimension 950 × 200 m that includes all four locations in Figure A.1 Based on existing bathymetric data from the National Oceanic and Atmospheric Administration, the mean lower low water depth of 14.3 m where mean lower low water is defined as the average of the lower low water height of each tidal day observed over the National Tidal Datum Epoch. Tidal data for the measurement site were estimated using data from the Chesapeake Bay Bridge Tunnel tidal station (located at 36 43.2, N 76 06.84 W, 27 km from the measurement site), obtained from the National Oceanic and Atmospheric Administration Center for Operational Oceanographic Products and Services. Accounting for tidal variation (Figure A.2), this would put the water depth between 14.7 m and 15 m. As exact measurement of the water depth were unavailable, the water depth has been estimated using the bubble pulse period of the 6 kg charge detonated on the seabed [17];

$$T_1 = 2.11\, W^{1/3} Z_o^{-5/6} \tag{7.41}$$

where W is the TNT equivalent charge weight, Z_o is the hydrostatic depth ($Z_o = Z + 10.1$ m), this put the water depth at 15.7 m to 16 m which is the value that is used here. Studies in the vicinity of the measurement site, conducted by the Virginia Institute of Marine Science to determine the feasibility of sand mining [80], [94]–[96], provided data on the seafloor. Data from

bottom grabs and core samples from these studies show a seabed composed of unconsolidated sediments consisting of fine to course sand and clay, with significant spatial variation (Figure A.3).

Profiles of sound speed versus depth in the water column were recorded using a YSI Castaway CTD device, which computes the sound-speed profile from direct measurements of temperature, conductivity (surrogate for salinity), and water depth. Sound-speed profiles were sampled at two times, 8:41:31 and 11:24:23 local time (Figure A.4), and were found to be approximately iso-speed at 1528 m/s. Owing to significant heave motion experienced by the two research vessels we did not allow this instrument to strike the seabed and risk damage, hence the CTD measurements do not extend to the bottom. This should not be considered an issue as the sound speed varies little with depth particularly in the vicinity of the seabed.

During the experiment there existed a swell- wave field originating from the Northeast with this wave field not linked with local wind conditions. Sea surface wave data was obtained from the National Data Buoy Center's (NDBC) Cape Henry 44099 wave buoy located at 36 54.9 N, 75 43.2 W, 19 km Northeast from the test site. During the measurement period significant wave height, defined as four times the root mean square (rms) of the wave-height varied between 1.0 m and 1.2 m; alternatively the rms wave height varied between 0.25 and 0.3 m.

A.2) Test Description

Five explosive charges were deployed as part of the Navy explosive ordnance disposal team's training exercise (Table A.1). These charges had TNT equivalent weights ranging from 0.1–6.0 kg. Depending on test, the detonation occurred at either (approximately) 9 m depth, or on the bottom. Tests 1–4 used C-4 charges with a TNT-equivalence of 1.34 (i.e., 1 kg of C-4 produces an explosive force equivalent to 1.34 kg of TNT), while Test 5 used a CH-6 charge with a TNT-equivalence factor of 1.5.

A.3) Equipment and Measurement Locations

The underwater detonation site location was provided by the Navy. Measurements were made from two Vessels; the R/V *Ocean Explorer* (Vessel 1) located 430 m from the underwater

detonation site for Tests 1–5 and the F/V *Instigator* (Vessel 2) located 165 m away for Tests 1–2 and 950 m away for Tests 3–5 (Figure A.5).

From Vessel 1, acoustic data were recorded using a vertical line array (VLA), and a Loggerhead autonomous recording device (Figure). The VLA elements consisted of nine hydrophones (ITC 1032) with 0.7 m spacing. Data from the VLA were recorded on a multi-channel coherent data acquisition system (Astro-Med DASH-20) with each channel sampled at 62,500 Hz sampling frequency. The Loggerhead consisted of a single hydrophone recording at a sampling frequency of 50,000 Hz. The VLA and Loggerhead were attached to a weighted line secured to a davit. A HOBO data logger (HOBO), used to measure water depth, was also attached to the line and was mounted exactly halfway between Hydrophones 2 and 3. The hydrophone depths of the VLA and Loggerhead were determined using these depth measurements. A summary of the hydrophone depths can be found in Table A.2.

From Vessel 2, acoustic data were also recorded using a Loggerhead system at a sampling rate of 50,000 Hz. Similar to the Vessel 1 setup, the Loggerhead was attached to a boat-mounted line (Figure A.5), and a HOBO data logger was used to determine the hydrophone depths (summarized in Table A.2).

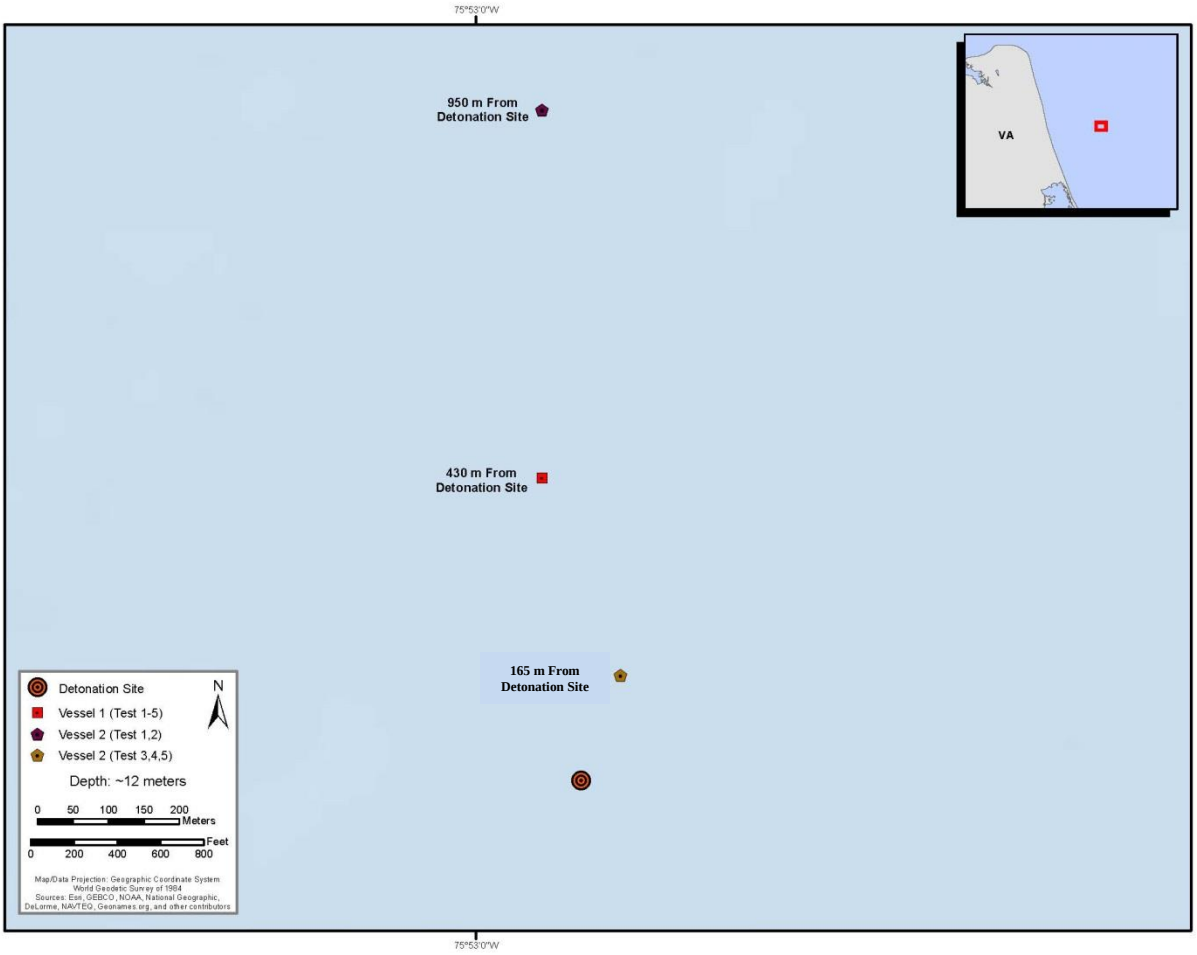

Figure A.1 Map of measurement site with the locations of Vessel 1, Vessel 2, and the detonation site. The measurement site and wave buoy location in relation to the Virginia coastline can be found in the inset map (map by Dara Farrell).

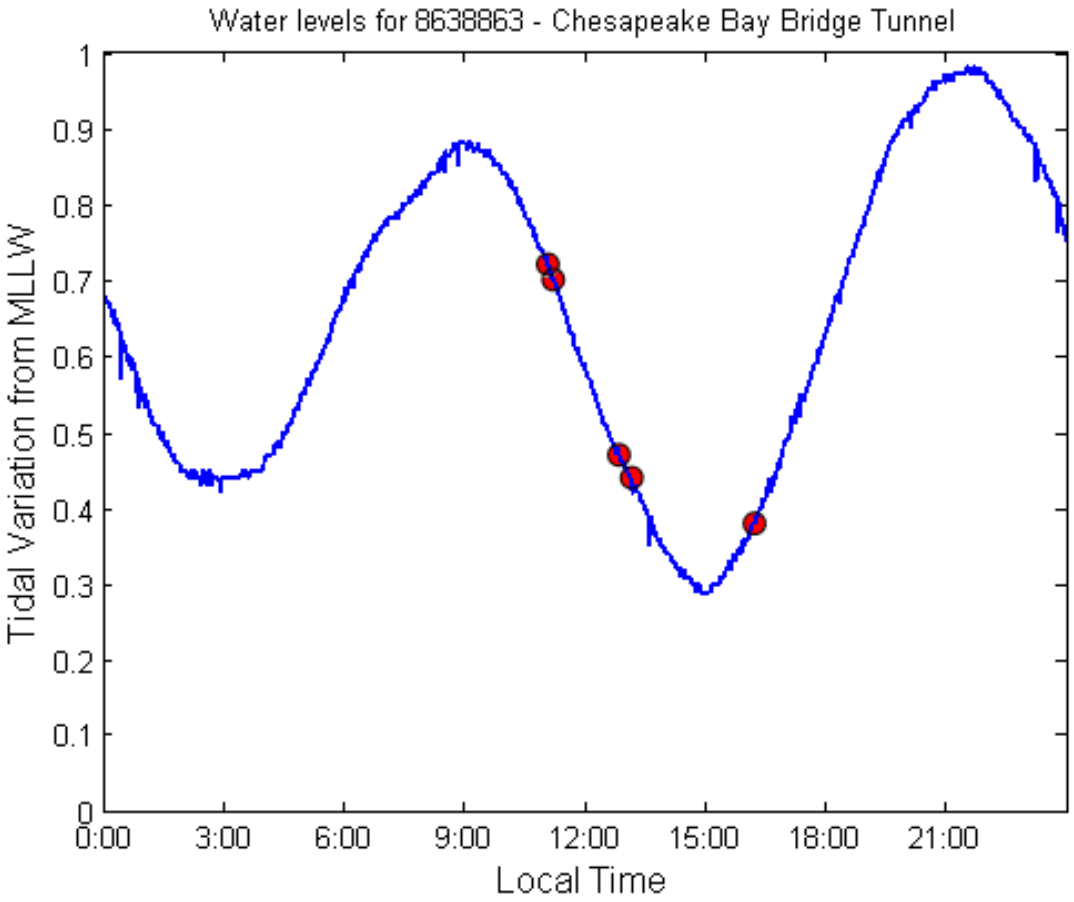

Figure A.2 Tidal variation from Chesapeake Bay Bridge Tunnel tidal station. Height is the tidal variation from the mean low lower water level in meters. Red markers indicate underwater detonation times.

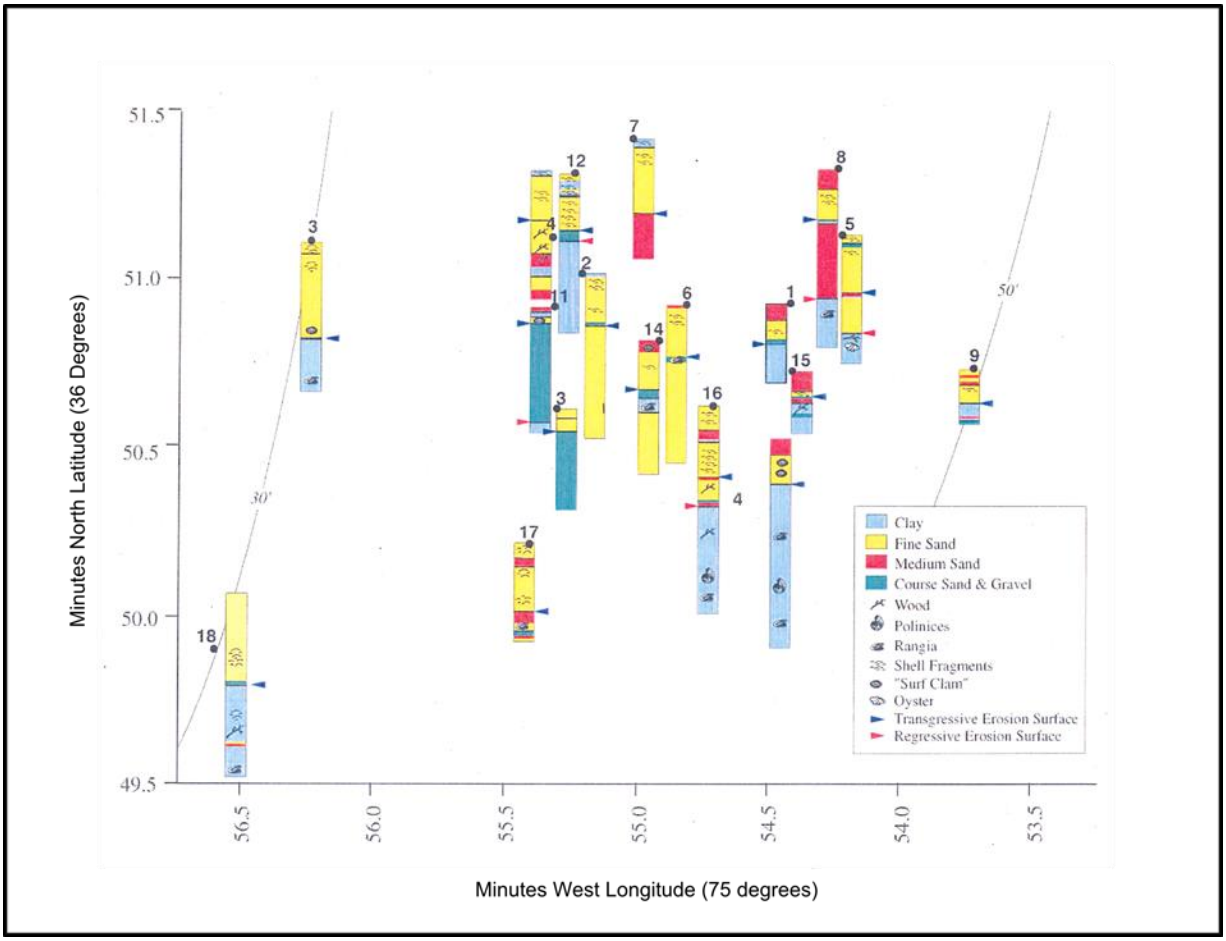

Figure A.3 Schematic showing core samples taken from a site located 1.6 km Northwest of the measurement site. This schematic shows the composition of 18 bottom core samples (numbered 1–18 in the original report), along with 9.1 m (30 ft) and 15.2 m (50 ft) water depth contours. Additional information on the core samples can be found in the original report. [80].

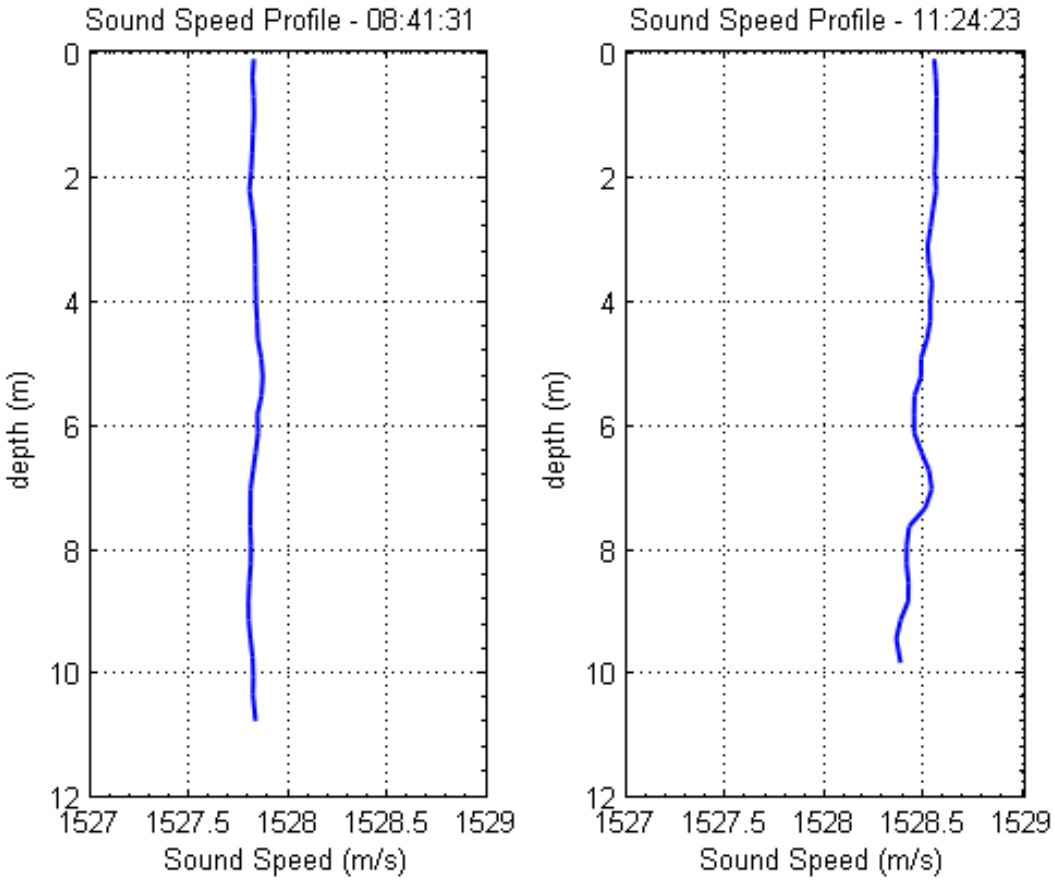

Figure A.4 Sound-speed profiles collected using YSI CastAway CTD device at the corresponding collection times.

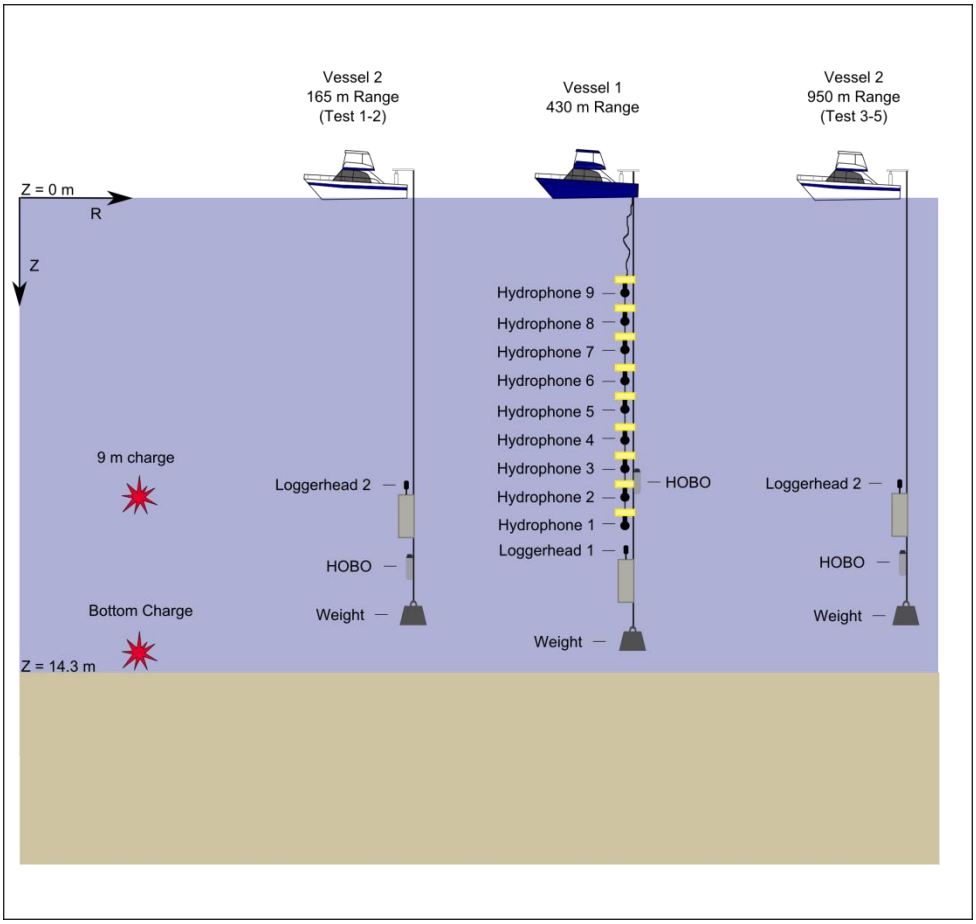

Figure A.5 Experiment geometry for the Virginia Beach MINEX trial. Equipment depths are listed in Table

Table A.1 Test charge summary for the Virginia Beach Experiment

Test	Local Time	Water Depth (m)	Explosive	Charge Depth	Charge Weight (Kg)	TNT Equivalent	TNT Equivalent Weight
1	11:04:09	15.0	C-4	9 m	0.2	1.34	0.3
2	11:12:02	15.0	C-4	Bottom	0.6	1.34	0.6
3	12:49:51	14.8	C-4	9 m	2.3	1.34	3
4	13:09:34	14.7	C-4	Bottom	4.5	1.34	6
5	16:11:59	14.7		9 m	0.07	1.50	0.1

Table A.2: Depth summary of hydrophones and Hobo data loggers for Vessel 1 and Vessel 2 for the Virginia Beach experiment.

Vessel 1 Hydrophone Depth (m)					
	Test 1	**Test 2**	**Test 3**	**Test 4**	**Test 5**
Hydrophone 9	6.6	6.6	6.8	6.8	6.8
Hydrophone 8	7.3	7.3	7.5	7.5	7.5
Hydrophone 7	8.0	8.0	8.2	8.2	8.2
Hydrophone 6	8.7	8.7	8.9	8.9	8.9
Hydrophone 5	9.4	9.4	9.6	9.6	9.6
Hydrophone 4	10.1	10.1	10.3	10.3	10.3
Hydrophone 3	10.8	10.8	11.0	11.0	11.0
Hobo	11.1	11.2	11.3	11.3	11.4
Hydrophone 2	11.5	11.5	11.7	11.7	11.7
Hydrophone 1	12.2	12.2	12.4	12.4	12.4
Loggerhead	12.9	12.9	13.1	13.1	13.1
Vessel 2 Hydrophone Depth (m)					
	Test 1	**Test 2**	**Test 3**	**Test 4**	**Test 5**
Loggerhead	9.5	9.7	10.0	10.4	10.3
Hobo	12.1	12.3	12.7	13.0	13.0

APPENDIX B: SILVER STRAND MEASUREMENTS

B.1) MEASUREMENTS

This section originally appeared in the report by Soloway and Dahl [28]. It has been included in this work for completeness.

Measurements were conducted on 13 and 14 May 2014, at a site located two (2) kilometers from the beach in the Silver Strand Training Complex part of the U.S. Navy's SOCAL Range Complex. On each day, two UNDET events occurred in rapid succession, with a delay of approximately 3 seconds between detonations. All four explosive charges detonated underwater consisted of 4.54 kg of composition 4 (C-4) explosive. The TNT-equivalence of C-4 is 1.34, thus each charge had an explosive equivalence of 6.08 kg of TNT.

Acoustic measurements associated with these UNDETs were collected from two study vessels; the F/V Alexes and El Gato Dos, both chartered sport-fishing boats of length approximately 11 meters. Alexes was designated as the near vessel, positioned closer to the detonations (400–800 meters), and the El Gato Dos was designated as the far vessel, positioned 1,300–1,700 meters from the detonations. The Alexes was positioned approximately at the 22-meter isobath (approximate depths from nautical charts) on both days, and the exact water depth was determined to be 23.7 meters using the depth sounder on Alexes. The El Gato Dos was also positioned on the same 22-meter isobath on 13 May, and on 14 May, it was positioned farther offshore on the 26-meter isobaths. The detonation sites and vessel locations for 13 and 14 May are shown in Figures B.1 and Figure B.2 respectively.

Acoustic measurement systems deployed from the near vessel Alexes consisted of a vertical line array (VLA), and a Loggerhead autonomous hydrophone recording device (Figure B.3). The VLA elements consisted of nine hydrophones (ITC 1032), spaced 0.7 m apart, with receiving voltage sensitivity ranging from -204 to -208 dB re V/μPa depending on the position of the hydrophone. Data from the VLA were recorded on a multi-channel coherent data acquisition system (Astro-Med DASH-20) with each channel sampled at 62,500 samples per second. The

autonomous Loggerhead system consisted of a self-contained data acquisition and storage system (Loggerhead Instruments DSG) and a single hydrophone (HTI-96-min) recording at 100,000 samples per second with a receiving voltage sensitivity of -220 dB re V/μPa. Additionally, a 3-channel geophone system was attached to the bottom of the VLA. This instrument was not part of the formal measurement plan and data from the geophone system are not included in this report, as they require further analysis and interpretation. The long-term goal of the geophone system is to examine acoustic particle velocity associated with UNDETs. Finally, the depths of the hydrophones were monitored continually using two HOBO® data loggers. A summary of the vessel range and hydrophone depths can be found in Table B.1.

Acoustic measurement systems deployed from the far vessel the El Gato Dos consisted of an identical Loggerhead device, and a second single-hydrophone device that was assembled at the University of Washington, referred to here as the USLM. It consisted of a single HTI-96-minute hydrophone recording 50,000 samples per second, with receiving voltage sensitivity of -205 dB re V/μPa. The measurement geometries associated with the Alexes and El Gato Dos are shown in Figure B.3 and a summary of the vessel range and hydrophone depths can be found in Table B.1.

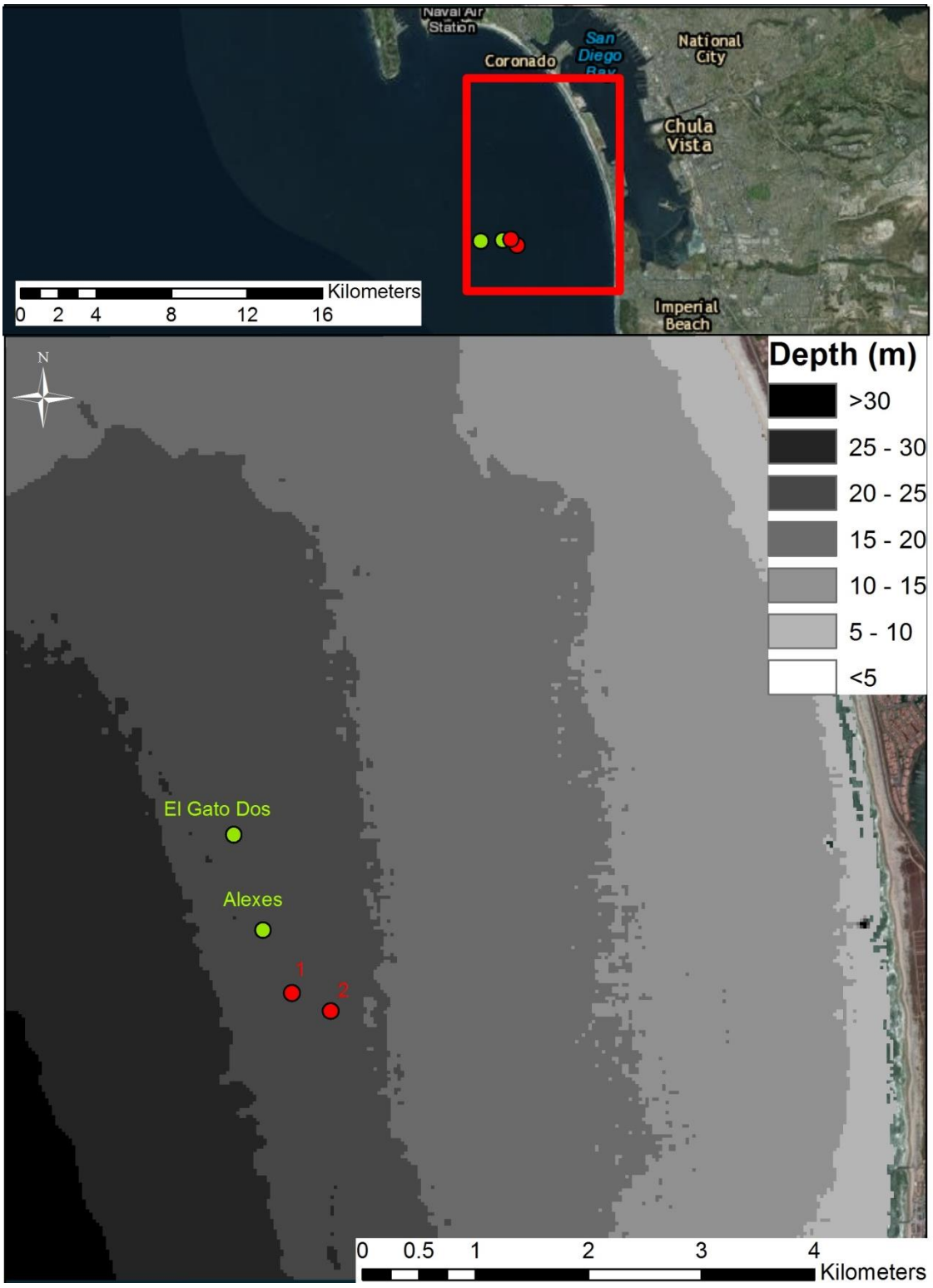

Figure B.1 Map of test site for 13 May 2014, with the locations of Alexes and El Gato Dos (green, labeled) in relation to the two UNDETs (red, numbered). A large-scale view is shown in the top panel (map by Dara Farrell).

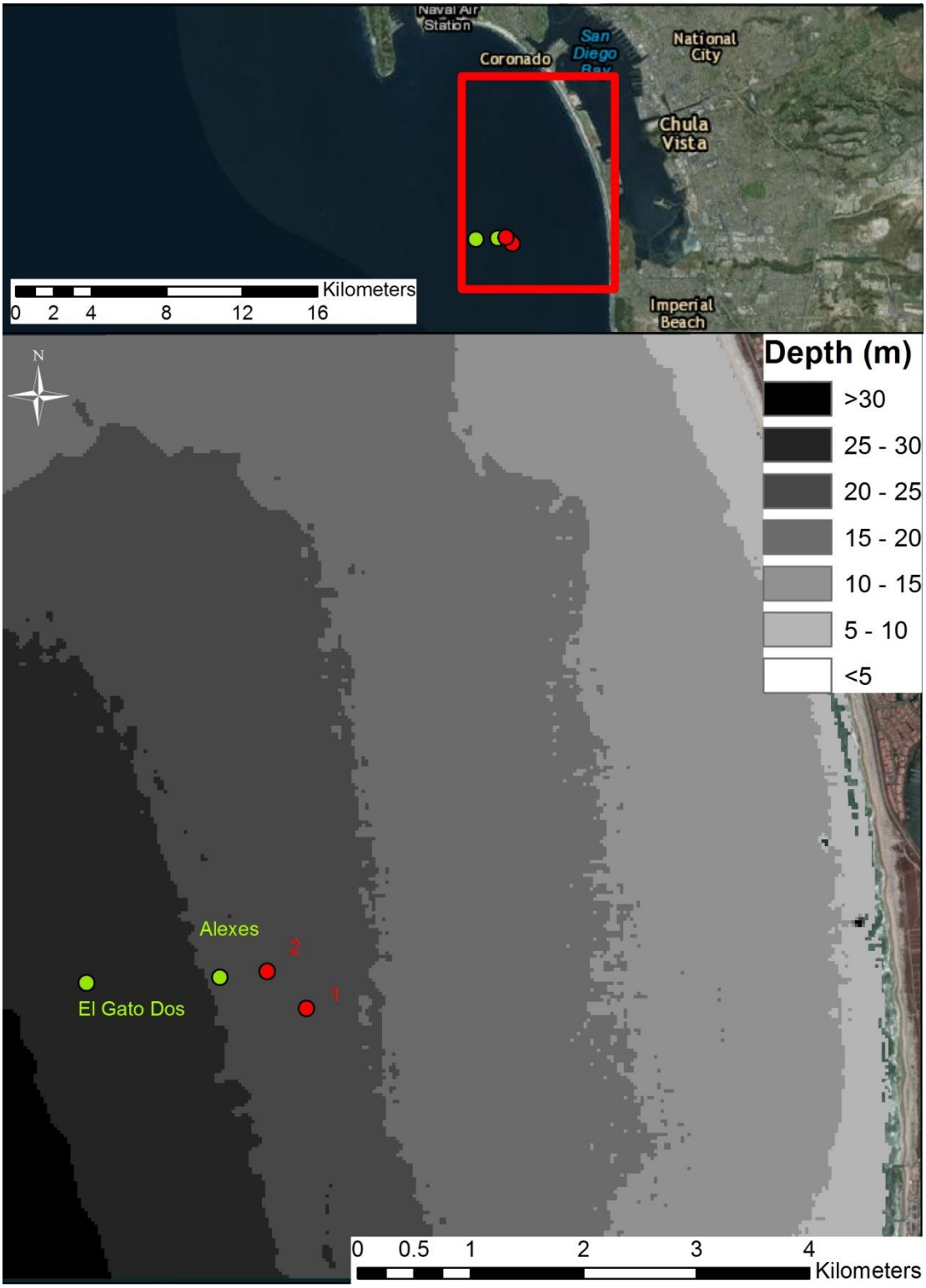

Figure B.2 Map of test site for 14 May 2014, with the locations of Alexes and El Gato Dos (green, labeled) in relation to the two UNDETs (red, numbered). A large-scale view is shown in the top panel (map by Dara Farrell)

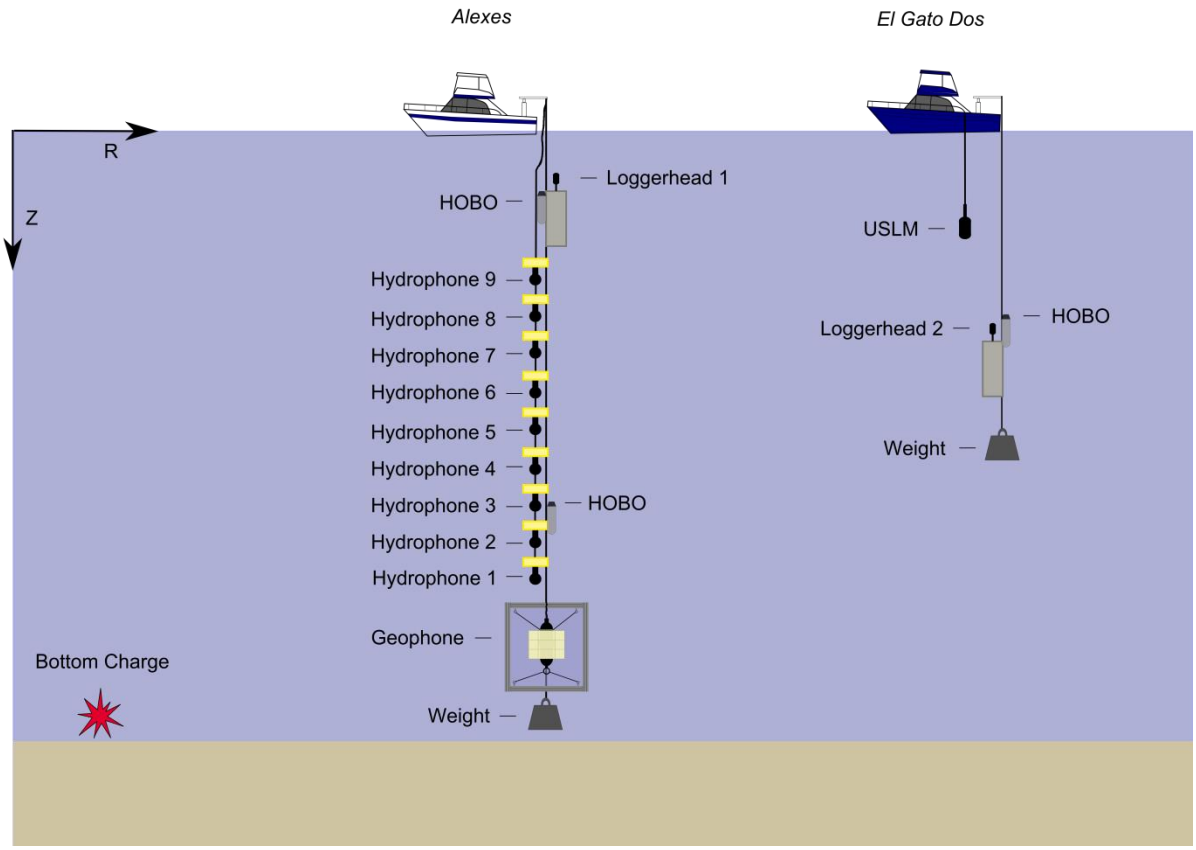

Figure B.3 Measurement instrument geometries for the Alexes and El Gato Dos.

B.2) Environmental Conditions and Measurements

The seabed in the immediate vicinity of the measurements is composed of unconsolidated, sandy sediments (Merkel & Associates, Inc. 2013). Profiles of sound speed versus depth in the water column were recorded from Alexes using a YSI CastAway Conductivity, Temperature, and Depth instrument, which computes the sound-speed profile from direct measurements of conductivity (a surrogate for salinity) and temperature as a function of pressure (a surrogate for depth). The water column at the time of these measurements was characterized by a thermocline between the surface and approximately 15 m, resulting in a sound speed that varied from 1,510 m/s near the sea surface to 1,492 m/s near the seabed, with sound speed in the bottom 10 meters of the water column being approximately constant (Figure B.4).

Sea surface conditions were measured using a Datawell Directional Wave Buoy deployed each day from the El Gato Dos. Both days were generally characterized by relatively calm conditions, during which the root mean square (RMS) wave heights were 0.19 meter (13 May) and 0.16 meter (14 May). Directional wave measurements indicated that the dominant (low frequency) wave field originated from an offshore direction, approximately from the W to WNW. The sea-surface wave measurements are summarized in Figure B.5 and Figure B.6 , respectively, and may be used in conjunction with more refined acoustic modeling efforts in the future.

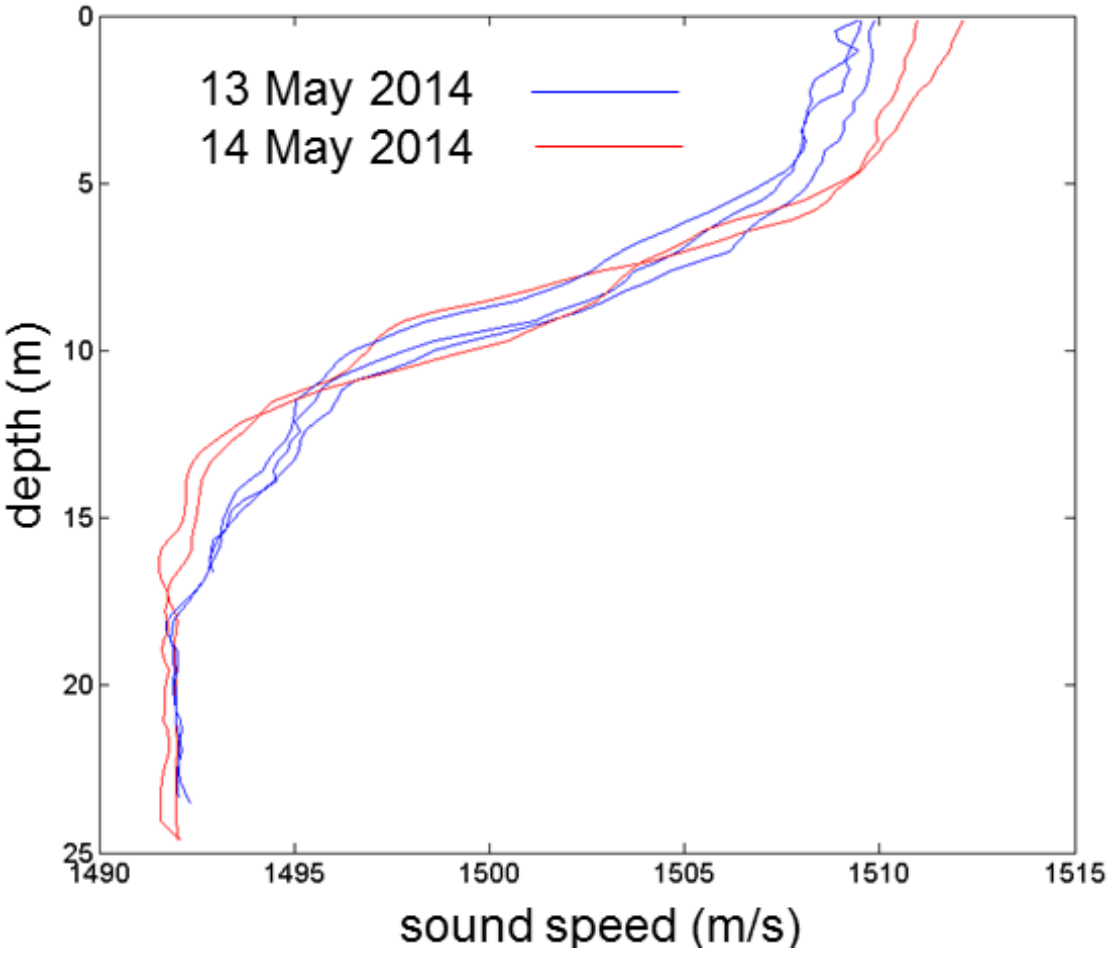

Figure B.4 Sound-speed profiles collected from the Alexes 13 and 14 May, corresponding to the times of the acoustic measurements on these days (Figure by Peter Dahl).

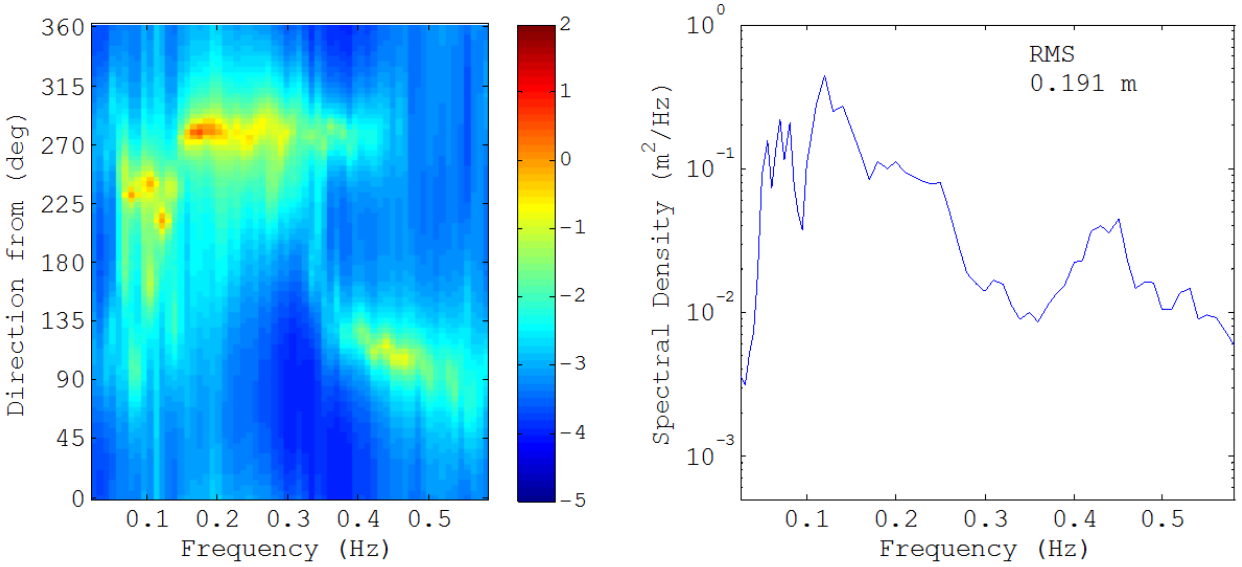

Figure B.5 Surface wave conditions during the 13 May 13 tests (at 1030 local time). Left panel: directional wave spectrum showing the peak in the spectrum at 0.15–0.30 Hz originating from 270°. Right panel: directionally-averaged spectral density. The RMS wave height is 0.19 meters (Figure by Peter Dahl).

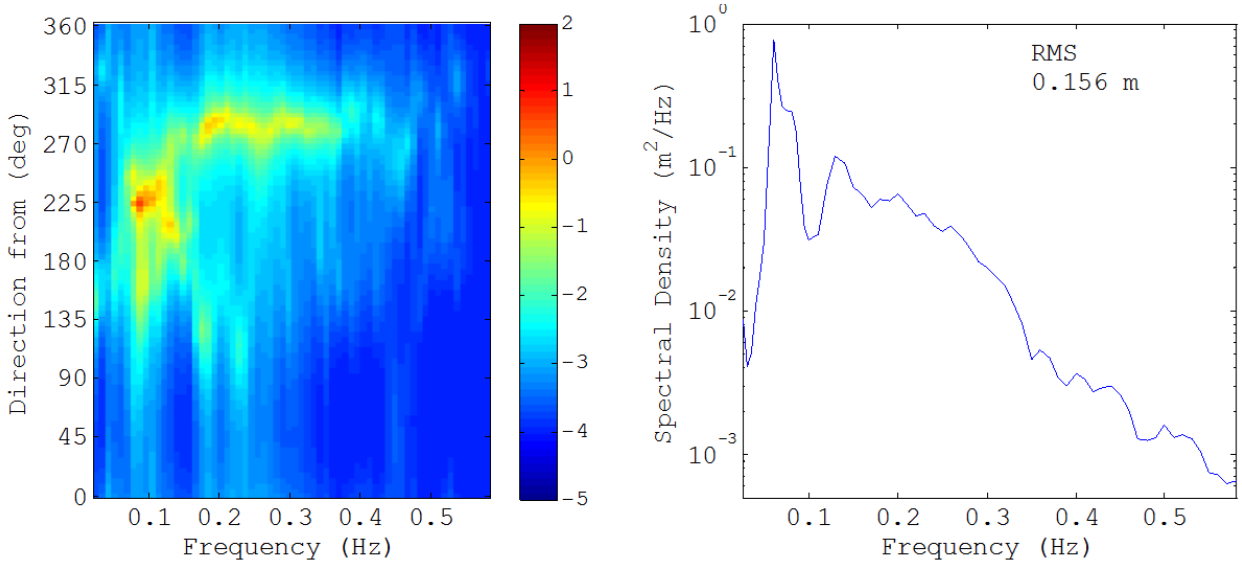

Figure B.6 Surface wave conditions in effect during the 14 May tests (at 10:30 local time): (left side) directional wave spectrum showing the peak in the spectrum at frequency of approximately 0.1 Hz originating from 250°, (right side) directionally-averaged spectral density. The RMS wave height is 0.16 meter (Figure by Peter Dahl)..

Table B.1: Measurement range and depth summary for acoustic measurements from two vessels on 13 and 14 May, 2014 off San Diego, California, along with summary of acoustic measurements expressed in peak pressure and SEL. SEL not currently not estimated from the VLA on 14 May, 2014 until a noise interference issue can be resolved.

Date	Vessel	Test Charge	Measurement System	Depth (m)	Range (m)	Peak Pressure (dB re 1 µPa)	SEL (dB re 1 µPa^2 s)
13-May-14	*Alexes*	1	Loggerhead*	12.3	512	216	189
		2	Loggerhead*	12.3	784	218	188
	El Gato Dos	1	Loggerhead*	15.7	1255	215	186
			USLM**	7.0	1255	215	187
		2	Loggerhead*	15.7	1499	212	185
			USLM*	7.0	1499	212	186
14-May-14	*Alexes*	1	Loggerhead*	11.6	685	215	187
			VLA***	13.1	685	218	-
				13.8		218	-
				14.5		218	-
				15.2		218	-
				15.9		219	-
				16.6		219	-
				17.3		219	-
				18.0		219	-
				18.7		220	-
		2	Loggerhead*	11.6	358	218	191
			VLA*	13.1	358	217	-
				13.8		218	-
				14.5		219	-
				15.2		219	-
				15.9		219	-
				16.6		219	-
				17.3		220	-
				18.0		220	-
				18.7		222	-
	El Gato Dos	1	Loggerhead*	19.9	1651	213	184
			USLM**	7.0	1651	209	184
		2	Loggerhead*	19.9	1353	215	185
			USLM**	7.0	1353	214	187

* Self-contained data acquisition and storage system (Loggerhead Instruments DSG)

** Universal Sound Level Meter

*** 9-hydrophone vertical line array

APPENDIX C: SENSITIVITY STUDY

C.1) Introduction

The goal of this section is to conduct a sensitivity study to explore the impact that varying geo-acoustic parameters have on the receiver-to-receiver path loss at the Virginia Beach measurement site. This sensitivity study is conducted using the Virginia Beach measurement site with the receiver-to-receiver path loss computed for the 430 m to 950 m ranges. The following variables are explored; the starting sound speed in Eq. (2.20) c_o, the maximum depth where the linear sound speed gradient transitions to a half-space seabed, the thickness of the first layer of the stacked layer seabed model described by Eq. (6.40), z_1, and the density in the seabed. ρ.

C.2) Sensitivity Study c_o

The sensitivity study for c_o in the linear sound speed gradient is shown below for 1550 m/s, 1600 m/s, 1650 m/s, and 1700 m/s. The results of this study show the variation impact most third-octave bands. The focus of Chapter 6 is primarily on frequencies between 40 Hz and 100 Hz, where increasing c_o results in a shift of the negative path loss peak to lower frequencies.

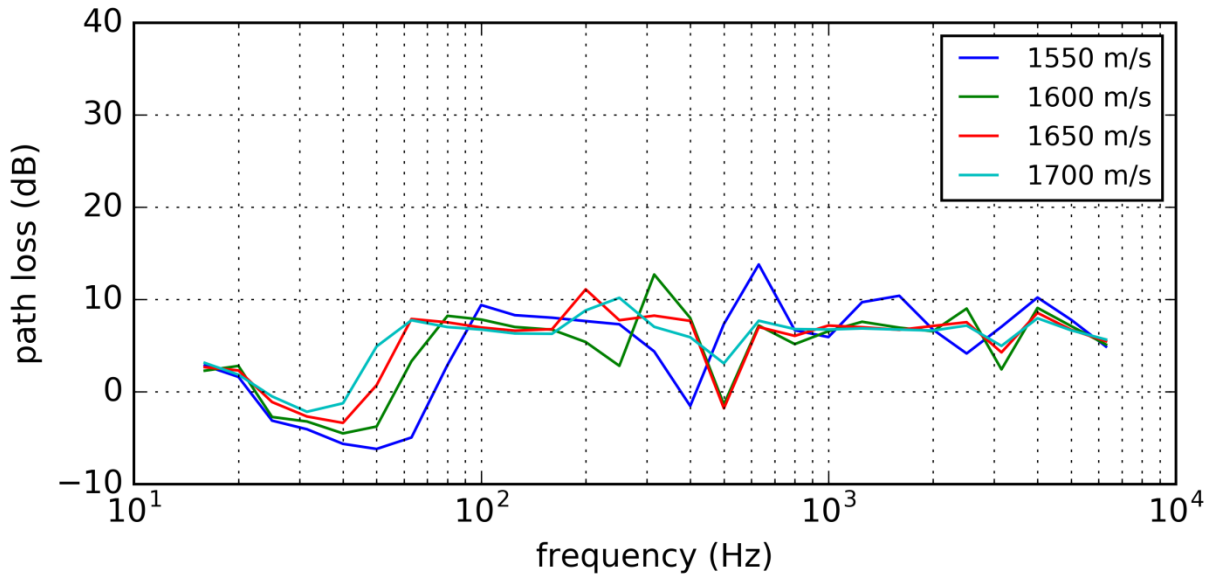

Figure C.1 Effects of varying c_o in the linear sound speed gradient used to model the Virginia Beach data. β is assumed to be 1.5 s^{-1} .

C.3) Sensitivity Study Half-Space Depth

The sensitivity study for D_{max} varies the depth at which the half-space in the seabed begins. The broadband path loss has been computed between the 430 and 950 m range receivers for 100 m, 200 m, 300 m and 400 m depths. The results of this study show that differences are isolated to frequencies below 100 Hz with half-space depths from 200 m exhibiting only minor variations. The 100 m half-space depth shows considerable variation from the other depths that were considered.

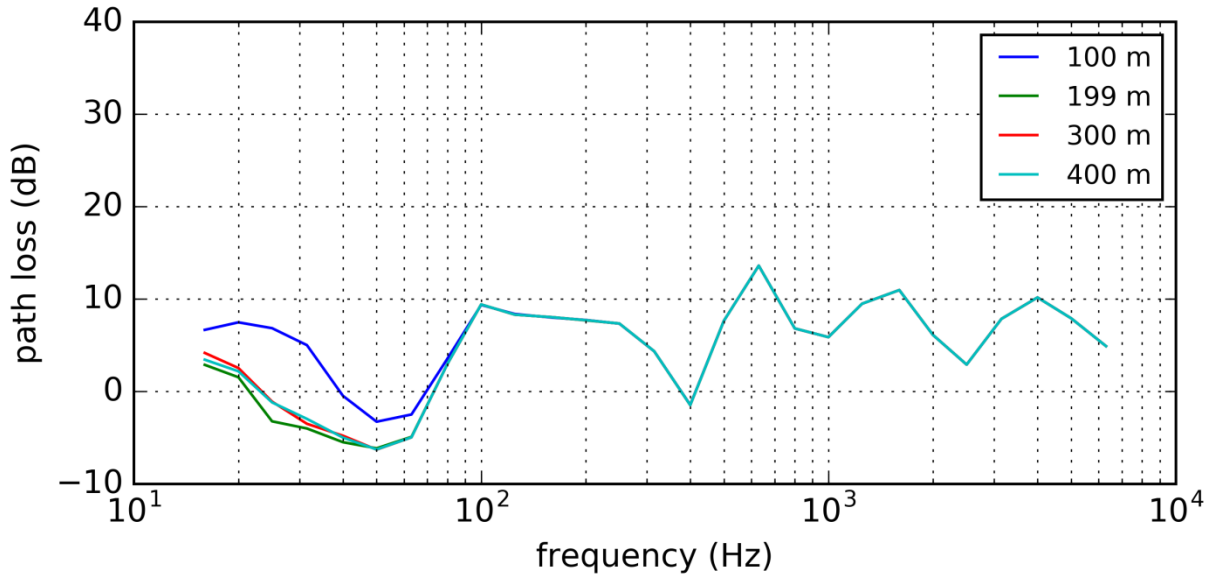

Figure C.2 Effects of varying the maximum depth of the half-space layer for the Virginia Beach seabed with a linear sound speed gradient.

C.4) Sensitivity Study Thickness of First Layer in Linear Sound Speed Gradient Seabed, z_1

The sensitivity study for the thickness of the first layer, z_1, varies the thickness of the first layer from 1 m to 9 m in 2 m intervals. The thickness of the first layer determines the travel time through the layer. As an equal layer travel time approach is used to model the linear sound speed gradient, this affects all layers within the equal layer travel-time approach. The results of this study show that differences in z_1 affect third octave bands above 1000 Hz however in general these effects are less than 1 dB and do not impact the primary frequency band considered in Chapter 6; low frequencies between 40 Hz and 100 Hz.

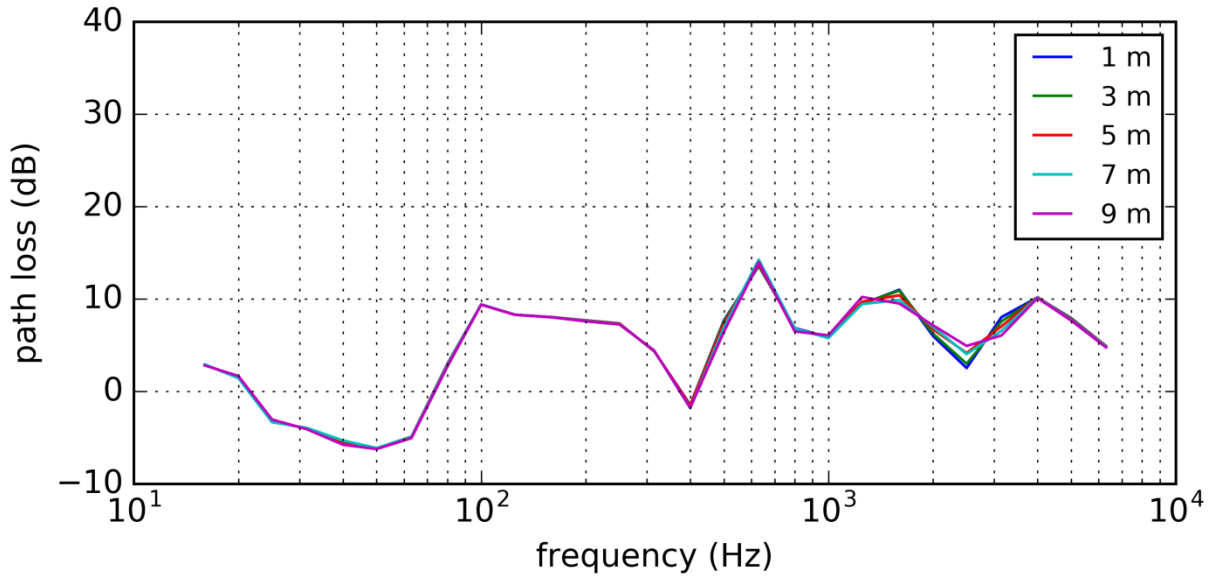

Figure C.3 Effects of varying the thickness of the first layer, h_1, for the Virginia Beach seabed with a linear sound speed gradient.

C.5) Sensitivity Study Seabed Density, ρ

The sensitivity study for the seabed density, ρ, varies the seabed density from 1600 kg/m^3 to 2200 kg/m^3 iterating by 200 kg/m^3. The results of this study shows a small impact below 100 Hz where increasing the density leads to a lower (more negative) path loss with this minimum shifting towards higher frequencies. Above 100 Hz the effects of varying the density are negligible.

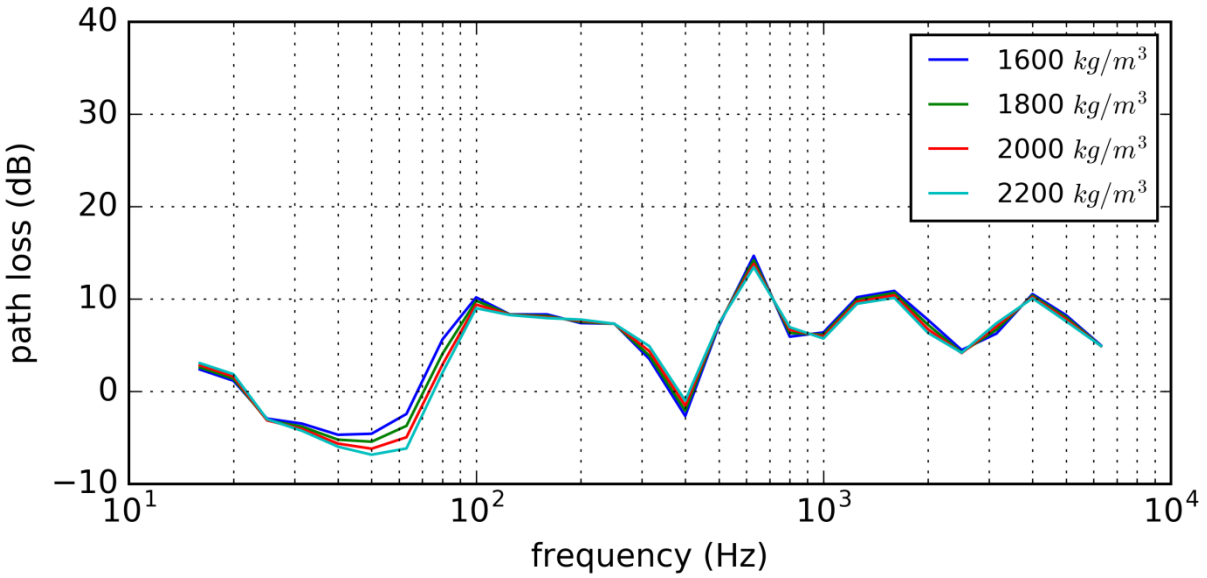

Figure C.4 Effects of varying the density of the seabed, ρ, for the Virginia Beach seabed with a linear sound speed gradient.

APPENDIX D: PU`ULOA SCHOLTE WAVE INVESTIGATION

D.1) Introduction

In this section low frequency signals present in the Pu`uloa data for the 1500 m Loggerheads are investigated in the hopes of determining an appropriate shear wave speed for the geoacoustic models in Chapter 5. It is shown that although there is a low frequency signal present that shows characteristics of a Scholte interface wave similar to those presented in Chapter 4, it is unlikely caused by a Scholte wave traveling at the sediment-basement interface of the three layer Pu`uloa seabed model.

D.2) Measurements

Time-frequency analysis is a useful tool for examining how the spectral content of the data changes with time. In this section this is accomplished using a 2^{14} Tukey window with a 10% ratio of the length of taper section to the total length of the window. For each time bin and 90% overlap for successive time bins was used.

Measurements for the three 4.5 kg NEW charges measured on day 3 of the Pu`uloa experiment on the high sensitivity hydrophone at 1500 m range show low frequency signal arriving 1.5 s to 3.5 s after the main water arrival (Figure D.1, Figure D.2 and Figure D.3). This signal shows similar characteristics to the Scholte waves measured at the Virginia Beach measurement site (Figure 4.1 and Figure 4.2) with low frequency arrivals coming in first followed by higher frequency arrivals. The frequency range of these signals is between 3 Hz and 7 Hz Note that due to the low frequency roll-off of the Loggerhead system, a correction from the manufacturer was applied (Figure D.4) with the correction at these frequencies between -35 dB and -25 dB respectively. In the next section numerical broadband modelling is used to explore this signal.

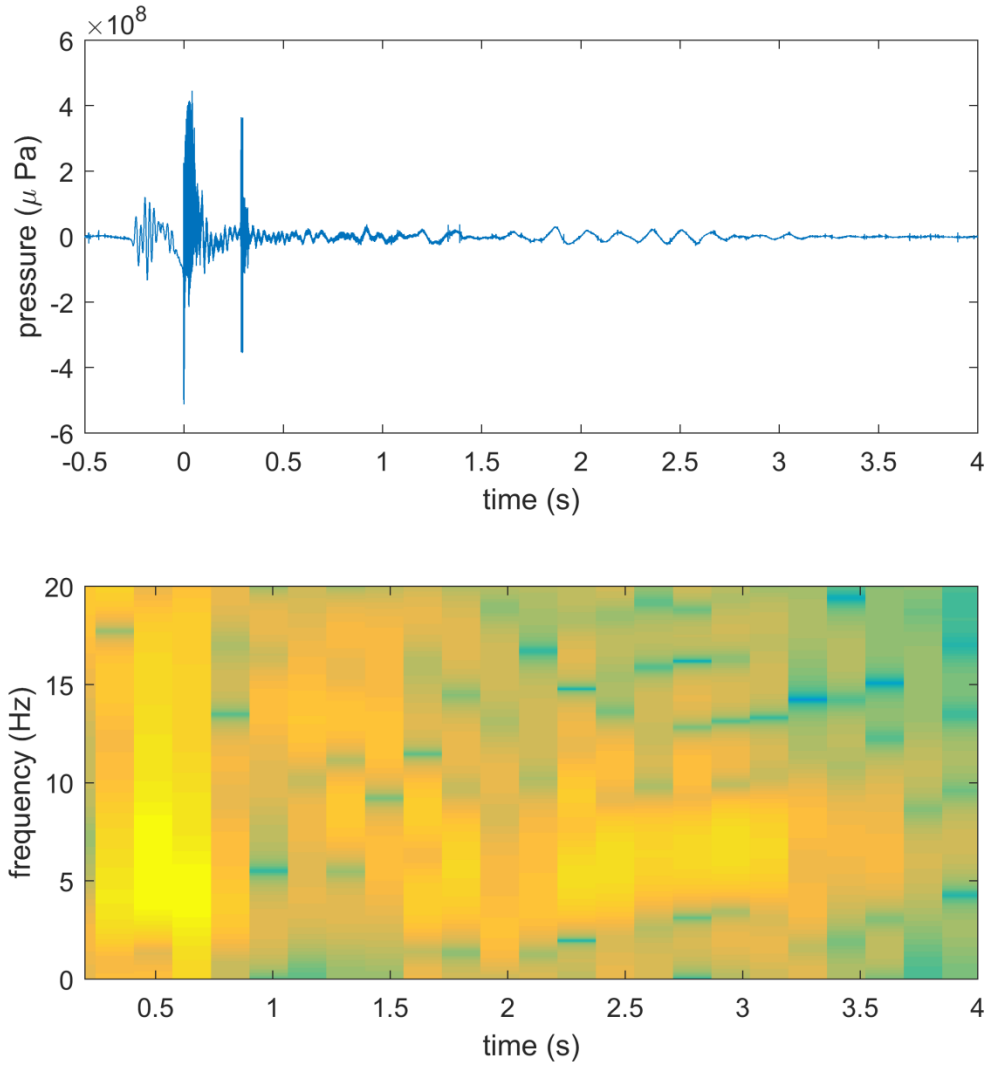

Figure D.1 Time series (top) and spectrogram (bottom) of the data collected on day 3 of test 1 of the 4.5 kg NEW charges measured on the high sensitivity Loggerhead system at 1500 m. Note that time 0 s corresponds to the main water arrival.

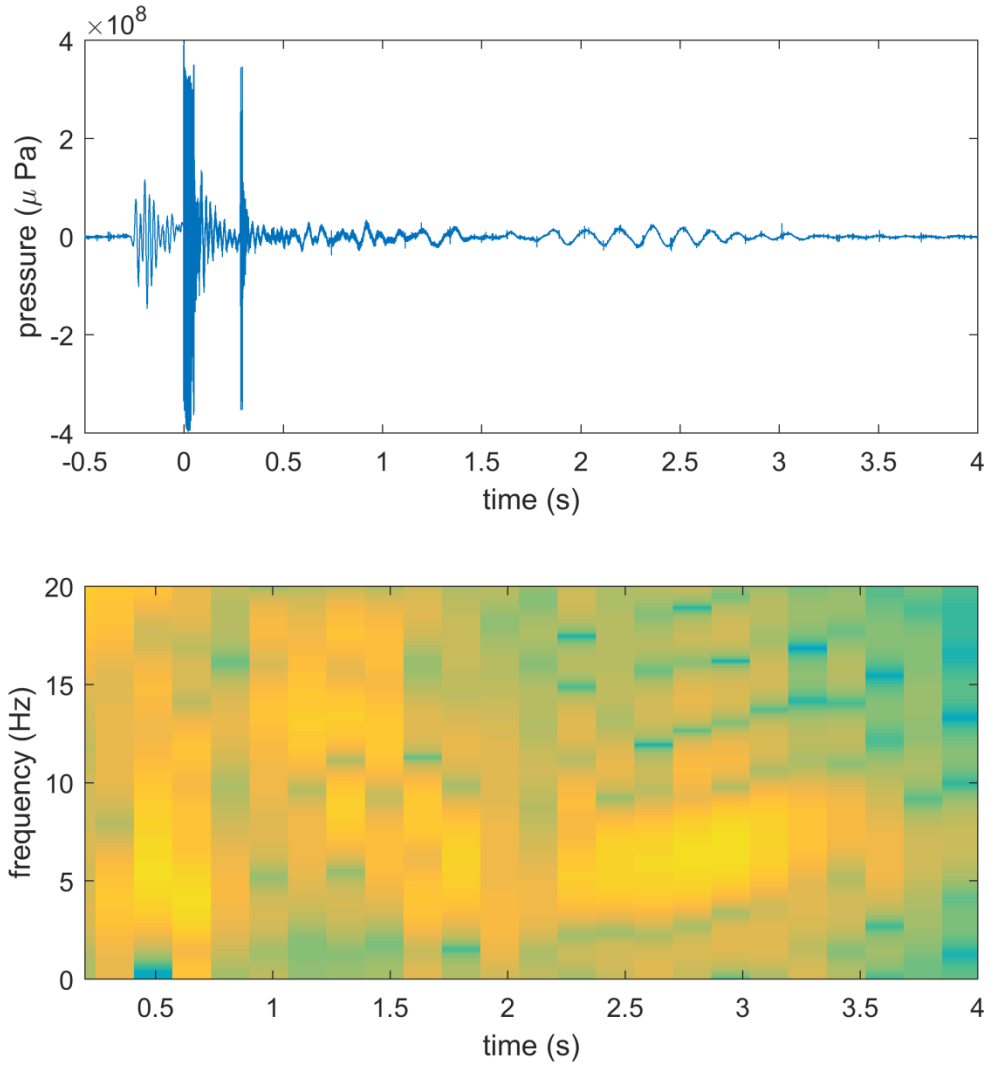

Figure D.2 Time series (top) and spectrogram (bottom) of the data collected on day 3 of test 2 of the 4.5 kg NEW charges measured on the high sensitivity Loggerhead system at 1500 m. Note that time 0 s corresponds to the main water arrival.

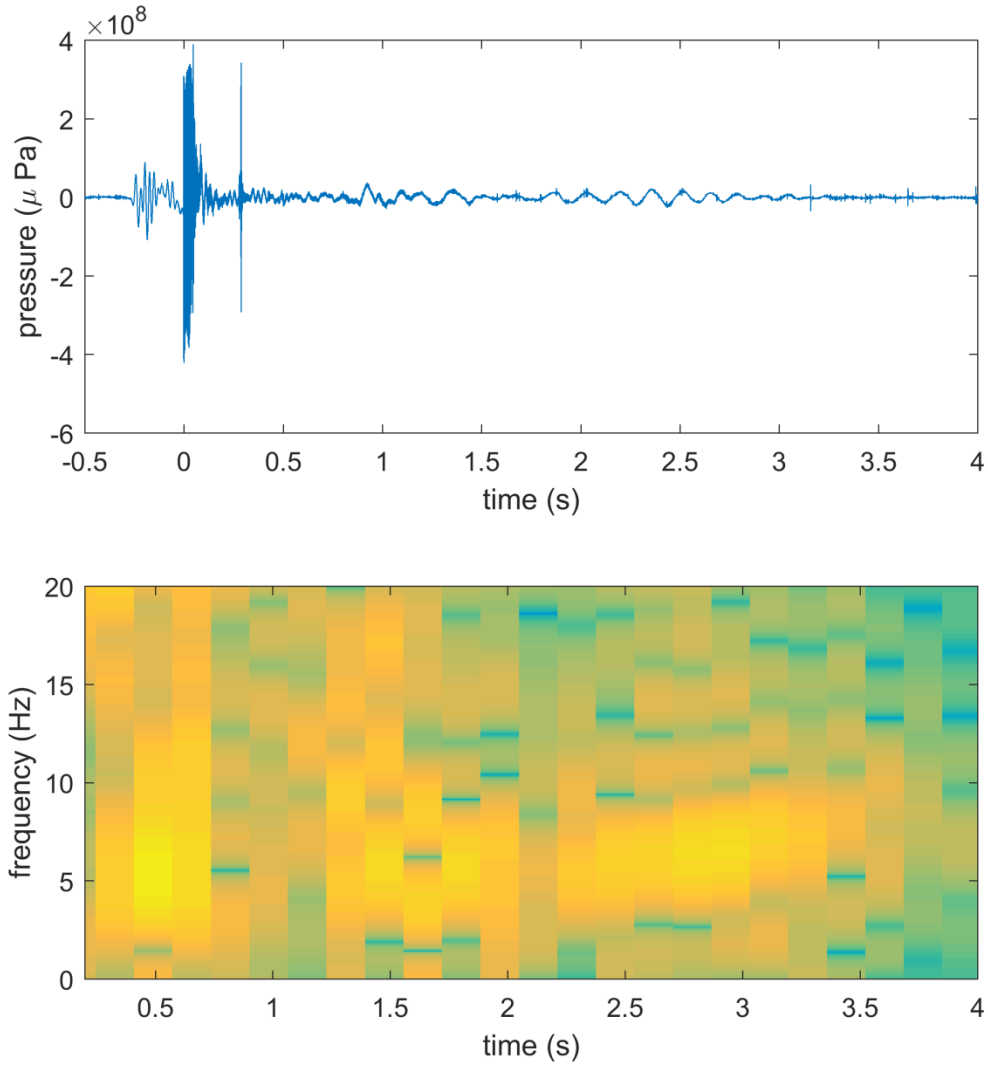

Figure D.3 Time series (top) and spectrogram (bottom) of the data collected on day 3 of test 3 of the 4.5 kg NEW charges measured on the high sensitivity Loggerhead system at 1500 m. Note that time 0 s corresponds to the main water arrival.

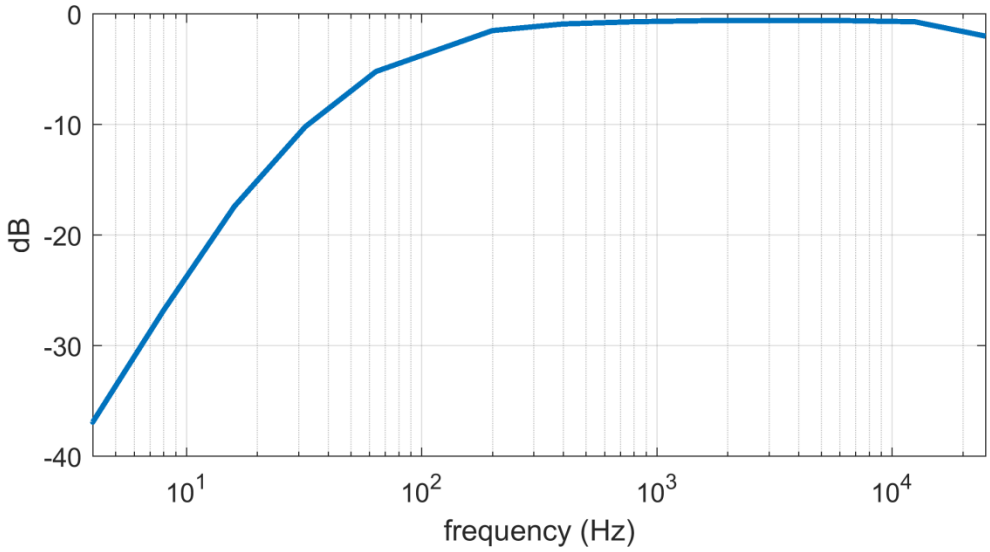

Figure D.4 Receiving voltage sensitivity for the Loggerhead system. This correction has been applied to the data discussed in this section.

D.3) Modelling

In this section OASES is used to compute broadband models using the Chapman-Chapman source model discussed in Chapter 4 and the three-layer geoacoustic model discussed in Chapter 5 to explore whether the signals present in Figure D.1, Figure D.2 and Figure D.3 are Scholte wave arrivals. Using the arrival time delay of roughly 2.25 s between the main water arrival and the low frequency signal gives a rough wave speed of 465 m/s. If we assume that the Scholte wave is 93% of the shear wave speed gives a shear wave speed of roughly 500 m/s. This either corresponds to the shear speed in the thin sediment layer or the shear speed in the limestone half-space basement. It is well established that this is a very high shear speed for sand (from Chapter 4 and literature) so it is more likely that it would be the shear wave speed in the limestones.

Modelling was accomplished using the geoacoustic model discussed in Chapter 5 supplemented with either a shear speed of 500 m/s or 1075 m/s (from Chapter 5) used for the limestone basement. The source has been modelled using the Chapman model discussed in Chapter 4 and has been located near the seabed.

Figure D.5 shows the model results for a shear speed in sand of 150 m/s and a shear speed in the limestone basement of 490 m/s. Looking at the results we see that a low frequency signal is observed at roughly 2.25 s and 2.5 s after the main water arrival, however the dispersive characteristics in the data cannot be observed. Note that two signals can be observed as one is a result of the shock arrival and the other is a result of the bubble pulse. This has been confirmed through modelling work using a source with and without a bubble pulse. As a supplement of this analysis the analytical reflection loss model (Chapter 5) has also been used to compute the reflection loss for this model and compare it to the reflection loss for a two-layer fluid seabed (Figure D.6). From this model we see that the fluid seabed and elastic seabeds are almost identical with the high losses below 1500 Hz not accounted for.

By running a similar model (Figure D.7) where the shear wave in the limestone basement is 1075 m/s (as discussed in Chapter 5) we see that the low frequency signal come in between 0.75 s and 1.0 s after the main water arrival and we once again cannot observe strong dispersion characteristics seen in the measured data. Unlike the previous scenario, the analytical reflection loss model for this environment is distinctly different than the fluid seabed model with the high losses below 1500 Hz accounted for (Figure D.8).

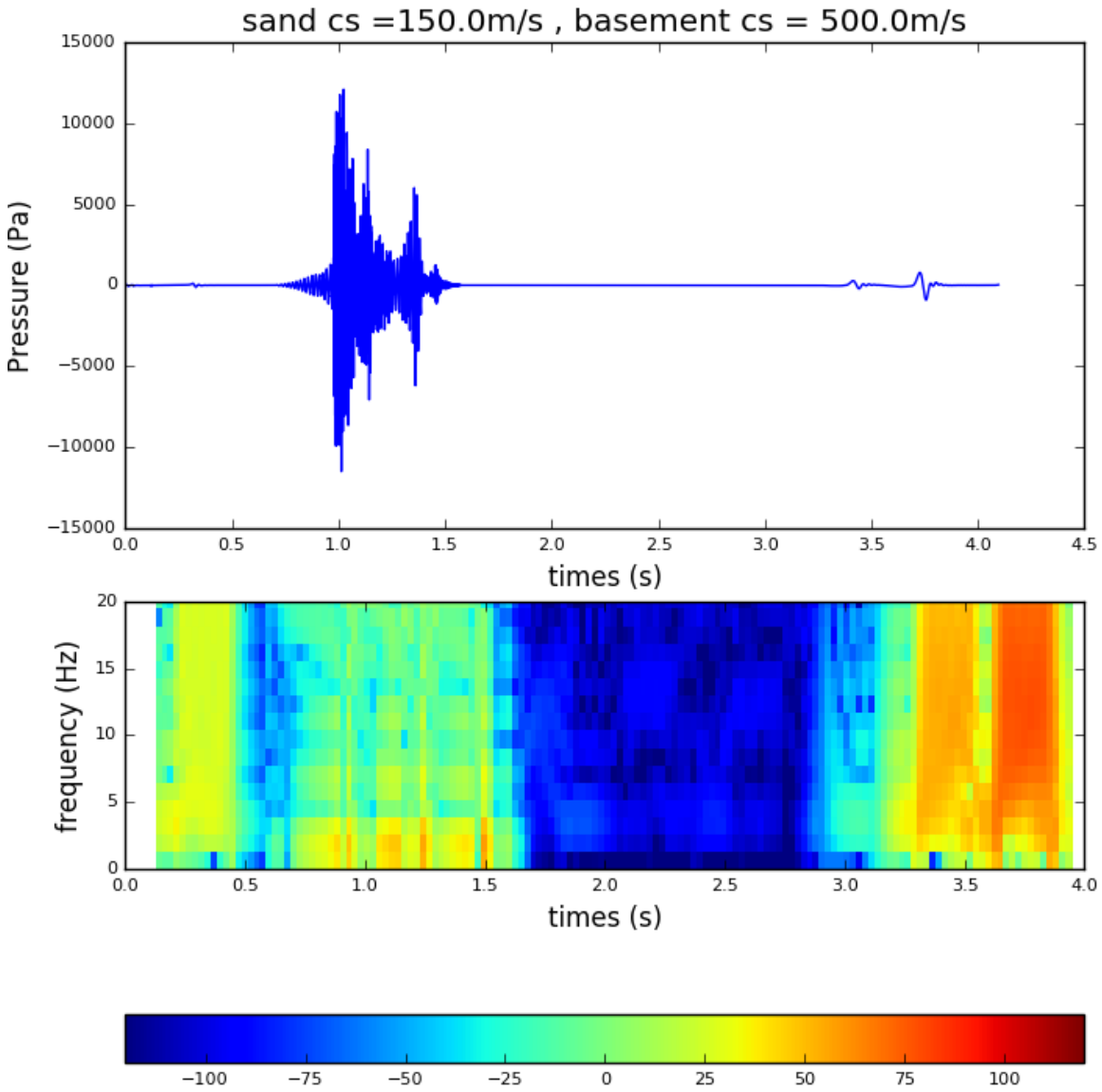

Figure D.5 Time series (top) and spectrogram (bottom) of the broadband model for the environment described using 150 m/s for the shear speed in the sand and a shear speed of 490 m/s in the limestone basement.

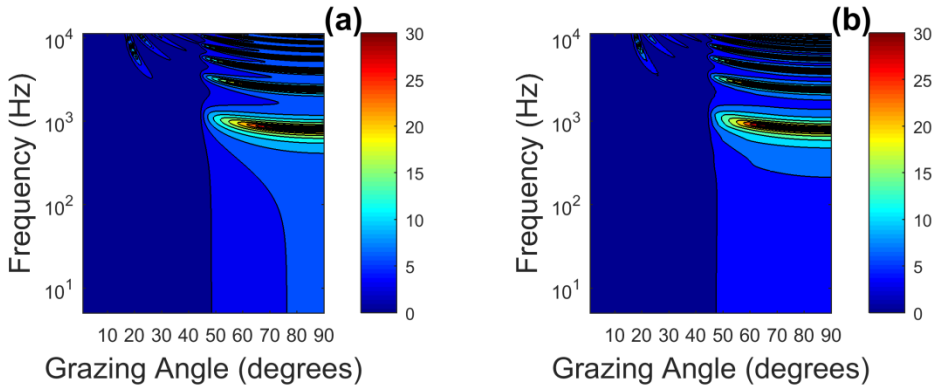

Figure D.6 Analytical reflection loss model calculated using Eq. (2.22) for a two layer fluid seabed (a) and two layer elastic seabed environment (b) where the shear speed in the sand is 150 m/s and the shear speed in the limestone basement is 490 m/s.

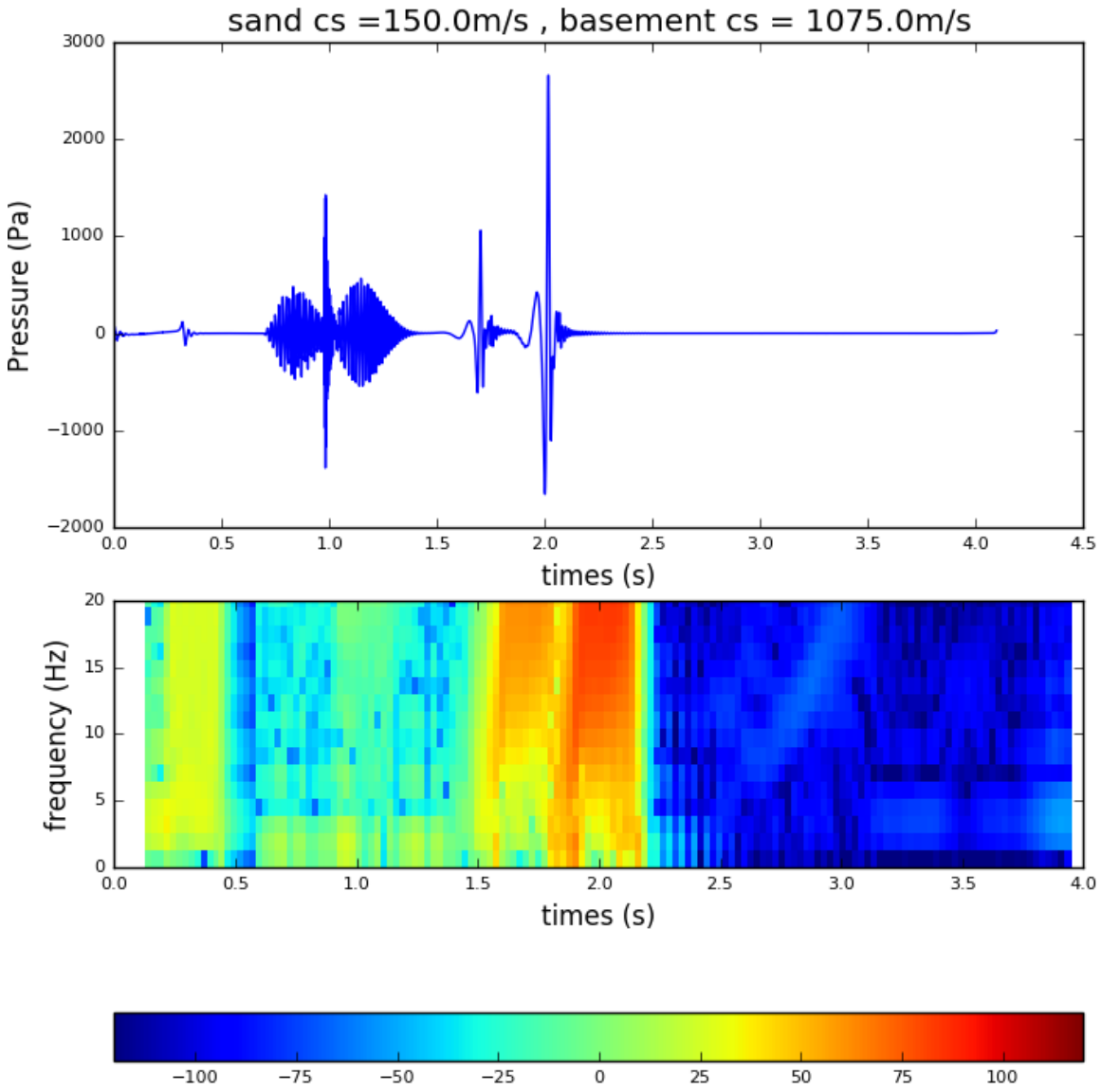

Figure D.7 Time series (top) and spectrogram (bottom) of the broadband model for the described using 150 m/s for the shear speed in the sand and a shear speed of 1075 m/s m/s in the limestone basement.

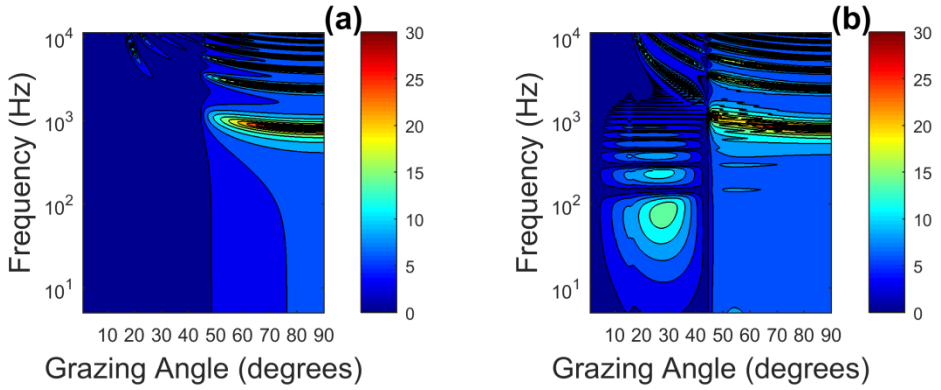

Figure D.8 Analytical reflection loss model calculated using Eq. (2.22) for a two layer fluid seabed (a) and two layer elastic seabed (b) where the shear speed in the sand is 150 m/s and the shear speed in the limestone basement is 1075 m/s.

D.4) Discussions and Conclusions

In this section low frequency signals observed in the data have been considered to determine whether they could be associated with Scholte wave arrivals which could help to determine an appropriate shear wave speed for the Pu`uloa environment. Using OASES to compute broadband time series models showed that it is unlikely that this signal can be used to determine the shear wave speed for the limestone basement at the Pu`uloa site.

To observe these signal, a low frequency correction had to be applied to the data (Figure D.4). The correction for the frequency range being considered is between 25dB and 35 dB. While the signal is consistently seen in all three 4.5 kg NEW tests, it is still unclear whether it is caused by this correction or is in fact associated with a real event. This is an ongoing study and will be addressed in future work.

APPENDIX E: META-DATA COLLECTION

In this appendix, a summary of meta-data collection techniques used during the three experiments discussed is presented;

1) Water depth (echo-sounder on boat after each shot)
2) Water sound speed (CTD system (conductivity, temperature and depth))
3) Bathymetry from navigation charts
4) Hydrophone depths (HOBO depth logger)
5) Source location using GPS measurements from divers
6) Receiver location at each shot using GPS; for boat mounted equipment using hand-held GPS measurements collected at the point on the boat where equipment has been deployed; for bottom deployed equipment a single measurement using a hand held GPS unit.
7) Source receiver range (source/receiver GPS measurements and range calculator from NOAA (https://www.nhc.noaa.gov/gccalc.shtml) or The Great Circle Calculator from Ed Williams (http://edwilliams.org/gccalc.htm))
8) Charge weight reported from Navy diver – it is important to confirm whether weights are reported as the measured weight of the C-4 or as the TNT equivalent weight or net explosive weight (NEW).
9) Time and date of detonation in UTM
10) Source detonation depth – from Navy divers. The detonation depth can be checked using the bubble pulse period described by Eq. (2.23). This method, however, relies on accurate charge weight.
11) Before and after photographs of all equipment and all hydrophones to determine any damage that occurred.

The collection of this information serves as a useful tool for understanding the data and the resulting noise levels. This improves both the predictive modelling stage of an EIA as well as assist with validation experiments.

VITA

Alexander G. Soloway received the B.Eng. degree from McGill University, Montreal, QC, Canada, in 2011, and the M.S. degree from the University of Washington, Seattle, WA, USA, in 2014, both in mechanical engineering. His research areas include the study of the environmental noise from shallow underwater explosions and Scholte wave propagation in the ocean bottom.